Real-time Intravascular Photoacoustics

Real-time intravasculaire fotoakoestiek

Thesis

to obtain the degree of Doctor from the
Erasmus University Rotterdam
by command of the
rector magnificus

Prof.dr. H.A.P. Pols,

and in accordance with the decision of the Doctorate Board

The public defense shall be held on

Friday 16th of June 2017 at 11.30 hours

by

Min Wu

born in Fujian, China

Erasmus University Rotterdam

Doctoral Committee

Promotor: Prof.dr.ir. A.F.W. van der Steen

Other members: Prof.dr. Felix Zijlstra

Dr. Evelyn Regar

Prof.dr. Stuart Foster

Copromotor: Dr. G. van Soest

This study was performed at Biomedical Engineering, Thorax Center, Erasmus MC Rotterdam, the Netherlands. The financial support by the Dutch Technology Foundation STW for this thesis is greatly acknowledged.

Financial support by Dutch Heart Foundation for publication of this thesis is greatly acknowledged. Financial support for printing of this thesis is kindly provided by: Erasmus Medical Center, Elforlight Ltd, Laser 2000 Benelux, and Diamond Kimberlit BV.

Printing: Ipskamp drukkers, Enschede, the Netherlands

The cover background design is created by Creative_hat - Freepik.com

ISBN: 978-94-028-0649-6.

Contents

Chapter 1. General Introduction

Based on Min Wu, Antonius F.W. van der Steen, Evelyn Regar, Gijs van Soest, Intravascular Photoacoustic Imaging of Vulnerable Atherosclerotic Plaque: An Emerging Technology Update, *Interventional cardiology review journal*, 2016;11(2):120–3

Cardiovascular diseases (CVDs) are the number one killer worldwide. In 2012, 17.5 million people died from CVDs, being responsible for 31% of all the global deaths. Particularly, 42% of these CVD deaths are due to coronary artery disease (CAD) [1]. Acute coronary syndrome (ACS), as the first common clinical manifestation of CAD, is most often triggered by the rupture of the vulnerable atherosclerotic plaque and thrombosis [2-4]. A Vulnerable atherosclerotic plaque comprises a lipid-rich necrotic core, covered by thin fibrous cap, that is weakened by the macrophages infiltration [5] (fig.1.1). Plaques that have this morphology and composition have a larger probability to be associated with acute coronary syndromes in clinical studies [6, 7]. To treat the coronary heart disease, percutaneous coronary intervention (PCI) may be suggested. It is a non-surgical procedure to open the narrow or blocked arteries and restores blood flow to the heart muscle. The procedure is done by inserting a thin catheter from the femoral or radial artery to the lesion site in the coronary arteries. At the lesion site, the artery is opened up by inflation of a balloon. Stents or scaffolds would be placed to hold the artery open. To guide PCI, an imaging technique capable of directly visualizing the vulnerable plaque lesion is very desirable.

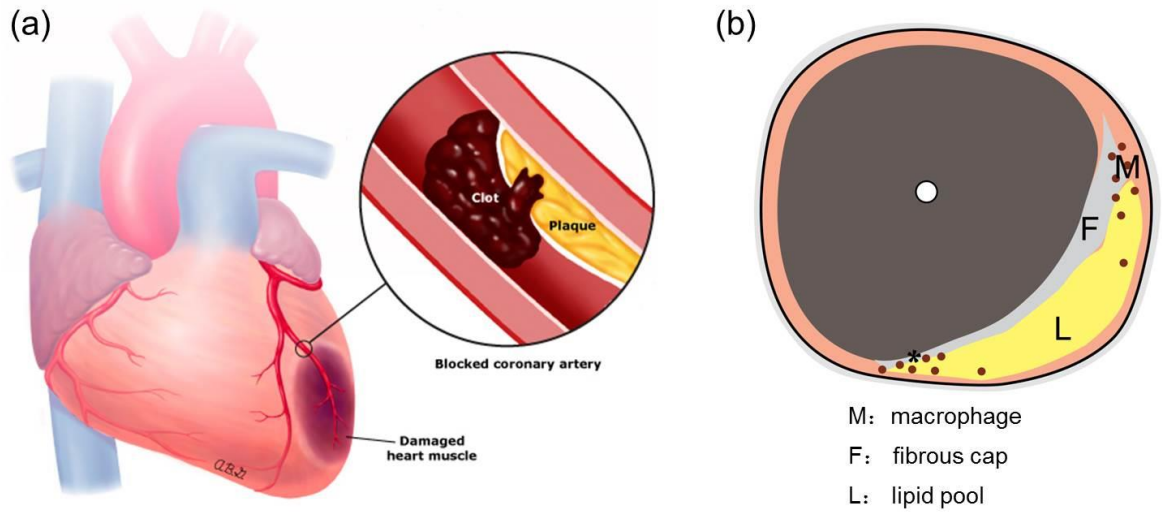

Figure 1.1 (a) Illustration of rupture of the vulnerable plaque. (b) The main composition of a vulnerable plaque

1.1 Intravascular imaging techniques

In the past three decades, several imaging modalities have been employed to identify vulnerable plaques. Coronary angiography is the oldest of these modalities and can only visualize the artery lumen not the artery wall and atherosclerotic lesions. Moreover, angiography images a 3D moving object in a 2D presentation.

Intravascular, catheter-based imaging methods can be safely used in a routine catheterization laboratory population [8] and offer direct visualization of the artery wall. Intravascular ultrasound (IVUS) imaging has been used in routine clinical practice for more than 20 years. Due to the limited acoustic contrast between soft tissues, the conventional greyscale IVUS image is not sensitive enough to differentiate plaque composition (except for calcium) [9, 10].

While an advanced analysis algorithm applied to IVUS images –VH-IVUS – has been developed to improve the plaque composition characterization[11], no data yet support its accuracy[12-14] to detect a lipid-rich necrotic plaque core. IVUS palpography is a technology to assess the local mechanical plaque properties based on the tissue deformation caused by the intraluminal pressure[15]. However, it can only sense the stiffness of the tissue rather than image the tissue, and assesses only the first 450 μm of the arterial wall [15].

Light-based intravascular optical coherence tomography (IVOCT) makes high resolution images (approx. 15 μm) with backscattered light from the tissue [16] and can image plaque components such as calcium, lipid, and thrombus. However, IVOCT currently relies on qualitative image interpretation to distinguish these features [17, 18]. The penetration depth of IVOCT is limited to 1–2 mm into atherosclerotic tissue, which means it often cannot see the extent of the plaque up to the adventitia.

Near-infrared spectroscopy (NIRS) is another light-based imaging modality for detection of lipid-rich necrotic core in plaque[19]. It provides a probability for the presence of coronary lipid based on spectral analysis of backscattered light[20]. However, NIRS cannot identify the amount and location of lipids, which may be important in risk assessment [21].

Several other innovative optical modalities have been proposed recently [22-25] and are currently being evaluated in clinical trials. The ability of these technologies to provide reliable, spatially precise, quantitative imaging of plaque lipid content is yet to be realized. We review one newer modality: intravascular photoacoustic (IVPA) imaging, an optical-acoustic hybrid imaging modality.

IVPA is currently under development to meet the needs of showing both morphology and chemical composition of the artery wall with good imaging depth and resolution. This technology takes advantages of the unique optical absorption contrast between different tissues and reasonably large penetration depth owing to the low acoustic attenuation in soft tissues [26, 27]. Published experimental data suggest it may be a strong contender for detailed plaque characterization and identification of plaque at increased risk of causing clinical sequelae.

1.2 Principles of IVPA imaging of atherosclerotic plaque

IVPA imaging requires short laser pulses (with a duration of a few nanoseconds) be applied for the irradiation of the artery wall. Absorption of the light transfers the optical energy to heat in the tissue and causes a thermoelastic expansion leading to a transient pressure rise (the laser pulse duration is shorter than both the stress relaxation and the thermal diffusion times). The initial pressure rise works as an acoustic source generating a broadband ultrasound wave that can be received by an ultrasound transducer. The amplitude of the emitted ultrasound signal is proportional to the magnitude of the specific optical absorption of the tissue and the light fluence. The time-of-flight of the received IVPA signal is related to the distance between the transducer and photoacoustic (PA) source. By illuminating tissue at different wavelengths, IVPA imaging is capable to image different tissue compositions based on their spectral contrast. Moreover, a co-registered pulse-echo IVUS image is naturally generated with the IVPA image, using the same transducer. A simple illustration of the IVPA principle is shown

in Figure 1.2. Combined IVPA/IVUS imaging provides the structure and chemical composition of the plaque, which are considered factors for plaque vulnerability.

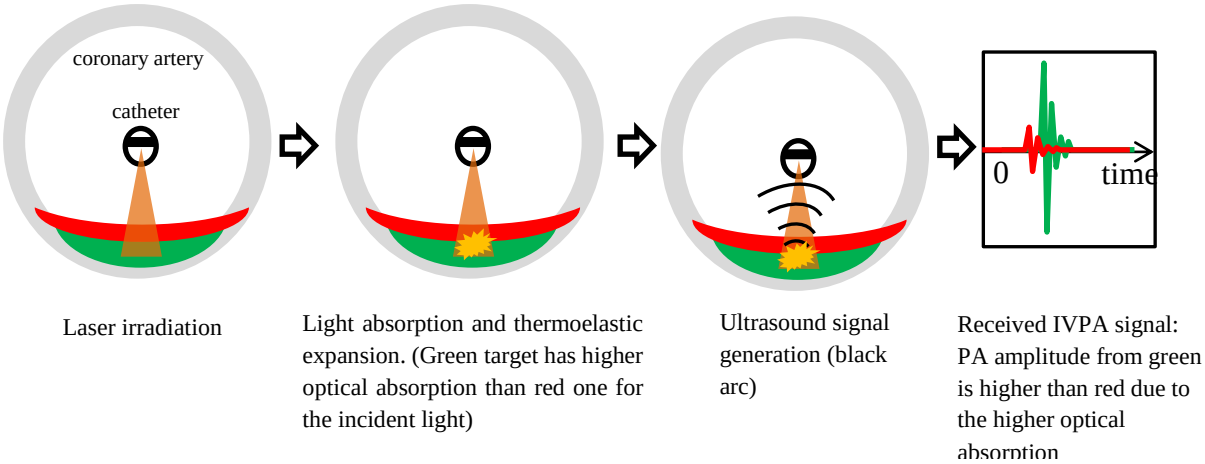

Figure 1.2. Illustration of the IVPA imaging principle.

The specific optical absorption spectra of lipids and other pure substances can be related to identification of plaque [28]. Various biomarkers present in plaques have been explored for their usefulness in IVPA imaging, with lipid being the most used. The capability of IVPA imaging of atherosclerotic plaque lipids has been demonstrated extensively with ex vivo tissues and in vivo animal models [29-35]. NIRS also makes use of lipid to identify potentially vulnerable plaque but with no depth resolution.

Macrophages are an important cell type related to the progression of atherosclerosis [29] and specific imaging of plaque macrophage content is a potentially interesting feature for identifying vulnerable plaque [30]. However, macrophages do not exhibit strong intrinsic contrast in the way lipids do. Thus, exogenous imaging contrast agents with high optical absorption are applied for visualization of macrophages by IVPA imaging [31, 32]. Furthermore, given that the activity of the enzyme matrix metalloproteinase (MMP) is an indicator of plaque instability, localization of MMP activity with an MMP-sensitive activatable probe in vulnerable plaques in human carotid specimens has been achieved using photoacoustic imaging [33]. More recently, an ApoE$^{-/-}$ mouse *in vivo* model injected with a photoacoustic ICG@PEG-Ag2S nanoprobe was successful in imaging plaque [34].

1.3 Challenges to bring IVPA Imaging into Clinical use

Encouraged by the capability of IVPA imaging of vulnerable atherosclerotic plaque, an intensive research effort is ongoing towards translation of IVPA imaging to clinical applications. Here, we review some of the key challenges.

1.3.1 Challenges towards a Miniature IVPA Catheter

A miniature, highly sensitive and flexible catheter for IVPA imaging is an essential element of bringing IVPA imaging technology into common use. As IVPA is an intrinsically multimodal imaging technique, the technical requirements on the catheter are more difficult to meet than for single-modality probes like OCT or IVUS catheters. A typical IVPA imaging catheter

consists of: (a) an optical part for light delivery; and (b) a broadband ultrasound transducer. The variety in the arrangement of these two parts in a catheter makes different catheter design. Two typical IVPA catheter designs so far are shown in Figure 1.3. The unit shown in Figure 1.3(a) is a collinear design, providing the largest overlap between optical and acoustic beams. Thus the design offers the highest reported sensitivity, but miniaturization is challenging [35, 36].

Another design possibility incorporates an offset between optical fiber and ultrasound transducer, either longitudinally [37] (see Figure 1.3 (b)) or laterally [38]. This catheter design is favored for miniaturization, and thus is most commonly used in many studies. However, the impact of the dual beam offset on PA imaging capability is unclear yet. A comprehensive characterization of the PA imaging property based on the catheter design is very important for better interpretations of the received PA images as well as making improvements for a better catheter design.

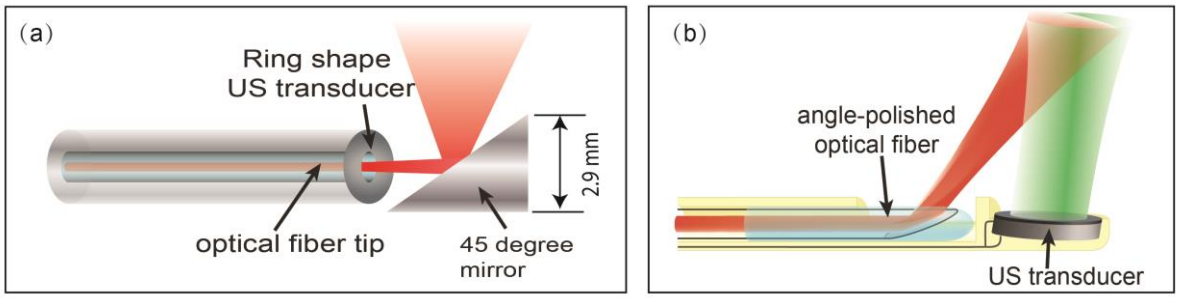

Figure 1.3. Schematic of different IVPA catheter design. (a) Schematic of a collinear IVPA catheter design. (b) Schematic of IVPA catheter with a longitudinal offset between optical and acoustic beams (Red optical beam and green ultrasound beam).

1.3.2 Challenge towards Specific Plaque lipids Identification by IVPA Imaging

IVPA imaging of an atherosclerotic artery, strong PA signal can be generated from the lipids in the plaque inside the artery wall as well as in peri-adventitial fat tissue around the artery [39]. Fig. 1.4 shows a typical example of IVPA image of an atherosclerotic coronary artery. In the IVPA image (fig.1.4 (a)), bright PA signal was clearly visible both in the plaque inside the artery wall (3 o'clock to 6 o' clock and 10 o'clock to 12 o'clock directions) and in the peri-adventitial fat tissue around the artery wall. While peri-adventitial fat is distributed around arteries throughout the body [40], making the detected bright PA signal from it a "false alarm" for identifying lipid-rich plaque lesions. Notably, lipids in the plaque lesions are rich in cholesterol and cholesteryl esters [41, 42], and the lipids in peri-adventitial fat are stored as a mixture of fatty acids [43]. This difference makes it possible to differentiate between them. This differentiation allows us to visualize only the plaque lipids while excluding the normal peri-adventitial fat. As a consequence, the presence and location of the lipid-rich plaque can be reliably and rapidly displayed in vessel cross-sections and longitudinal sections, without tedious examination of every individual cross sectional image in a catheter pullback scanning or error-prone automated IVUS image processing. This unique specific plaque lipids identification would be a valuable tool for guiding the assessment and treatment of coronary disease.

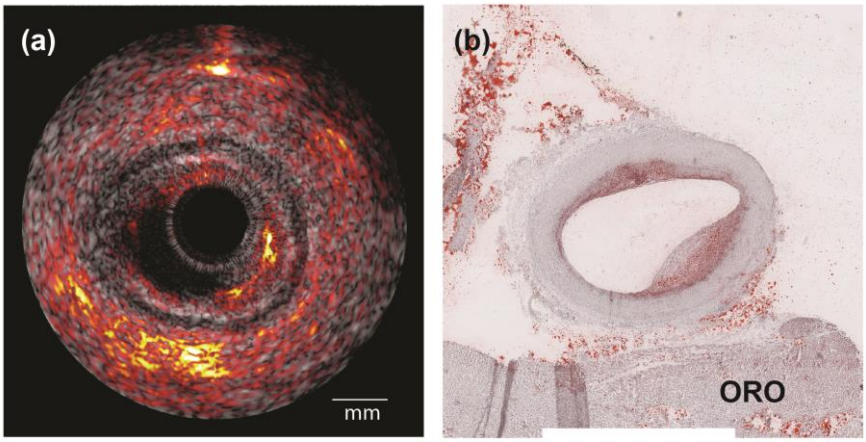

Figure 1.4 IVPA/US image of an atherosclerotic coronary artery. (a) Merged IVPA (at 1205 nm) and IVUS image of an atherosclerotic coronary artery. (b)) Oil Red O (ORO) histology staining result of the artery sample. In ORO staining, the lipids are in red.

Owing to the spectra contrast between the plaque lipids and peri-adventitial fat, multiple wavelength spectroscopic IVPA (sIVPA) imaging is capable of differentiation between them. However, performing multiple wavelengths sIVPA imaging impacts the complexity, cost, and speed of the imaging system. Minimization of the number of wavelengths for differentiation of different lipids, or improving the efficiency for specific lipid differentiation is necessary for practical application.

1.3.3 Challenges towards fast and safe IVPA imaging of vulnerable plaque

Despite successful plaque identification by IVPA imaging, the low imaging speed severely limits its application, mainly due to the slow laser systems being used, which have a pulse frequency of about 10-50 Hz. Generally, with a single-element catheter for IVPA imaging, every image line requires a laser pulse. To speed up IVPA imaging, a laser system with fast pulse rate is necessary. With the introduction of higher pulse-rate laser systems (2 kHz), IVPA imaging of lipid depositions has been increased to a speed of 1 frame per second (fps) [35, 36, 44]. This represents a significant step forward, but is still not fast enough for practical application.

Nevertheless, it is not possible to increase the pulse rate of lase unlimitedly due to the safety concern safety concerns about thermal damage of the artery for the patient and potential exposure hazard of skin and eyes for the operator. Especially, it is required to maintain enough pulse energy for high PA SNR while increasing pulse rate of the laser system for fast imaging speed.

1.4 Thesis objective and outline

To overcome some challenges addressed above and accelerate the translation of IVPA imaging system to clinical application, we are developing a new real-time IVPA imaging system with a well characterized, miniature, and flexible catheter, which allows us of the in vivo IVPA plaque detection in animal model.

Chapter 2 quantifies the imaging properties of a miniature IVPA catheter based on the longitudinal dual beam offset catheter design in terms of the spatial resolution. The impact of the dual beam offset on the received PA and US images is well characterized.

Chapter 3 presents an economic algorithm to detect and differentiate between the plaque lipids and peri-adventitial fat with only two wavelengths at 1700 nm spectral range. The performance of the algorithm was tested in several human coronary artery samples ex vivo.

Chapter 4 reports the frequency contents of the PA signal generated from the plaque lesion. Such information is very helpful to highly increase PA sensitivity for IVPA imaging of plaque lesions, enabling the possibility of IVPA imaging of lipids with a low the laser power.

Chapter 5 demonstrates a new real-time IVPA/US imaging system with a miniature, flexible catheter, capable of IVPA/US imaging of lipid plaque at a speed of 20 frames per second. The capability of the real-time IVPA/US imaging system was validated on a human atherosclerotic coronary ex vivo. With the imaging system, we conducted the first in vivo IVPA/US imaging of atherosclerotic plaque on swine coronary artery.

Chapter 6 concludes the achieved work in this thesis and discuss about some remaining issues for the future work.

References

1. Yang, J.-M., et al., *Photoacoustic endoscopy.* Opt. Lett., 2009. **34**(10): p. 1591-1593.
2. Falk, E., P.K. Shah, and V. Fuster, *Coronary Plaque Disruption.* Circulation, 1995. **92**(3): p. 657-671.
3. Bourantas, C.V., et al., *Hybrid intravascular imaging: current applications and prospective potential in the study of coronary atherosclerosis.* Journal of the American College Of Cardiology, 2013. **61**(13): p. 1369-1378.
4. Batty, J.A., et al., *Intracoronary Imaging in the Detection of Vulnerable Plaques.* Current cardiology reports, 2016. **18**(3): p. 1-12.
5. Schaar, J.A., et al., *Terminology for high-risk and vulnerable coronary artery plaques.* European Heart Journal, 2004. **25**(12): p. 1077-1082.
6. Kini, A.S., et al., *Multimodality Intravascular Imaging to Predict Periprocedural Myocardial Infarction During Percutaneous Coronary Intervention.* JACC: Cardiovascular Interventions, 2015. **8**(7): p. 937-945.
7. Goldstein, J.A., et al., *Detection of Lipid-Core Plaques by Intracoronary Near-Infrared Spectroscopy Identifies High Risk of Periprocedural Myocardial Infarction.* Circulation: Cardiovascular Interventions, 2011. **4**(5): p. 429-437.
8. van der Sijde, J.N., et al., *Safety of optical coherence tomography in daily practice: a comparison with intravascular ultrasound.* European Heart Journal - Cardiovascular Imaging, 2016.
9. Allen, T.J., et al., *Spectroscopic photoacoustic imaging of lipid-rich plaques in the human aorta in the 740 to 1400 nm wavelength range.* Journal of Biomedical Optics, 2012. **17**(6): p. 061209-10.

10. Choudhury, R.P., V. Fuster, and Z.A. Fayad, *Molecular, cellular and functional imaging of atherothrombosis.* Nature Reviews Drug Discovery, 2004. **3**(11): p. 913-925.
11. Nair, A., et al., *Coronary plaque classification with intravascular ultrasound radiofrequency data analysis.* Circulation, 2002. **106**(17): p. 2200-2206.
12. Thim, T., et al., *Unreliable Assessment of Necrotic Core by Virtual Histology Intravascular Ultrasound in Porcine Coronary Artery Disease.* Circulation-Cardiovascular Imaging, 2010. **3**(4): p. 384-391.
13. Shin, E.S., et al., *In vivo findings of tissue characteristics using iMap IVUS and Virtual Histology IVUS.* EuroIntervention, 2011. **6**(8): p. 1017-9.
14. Puri, R., M.I. Worthley, and S.J. Nicholls, *Intravascular imaging of vulnerable coronary plaque: current and future concepts.* Nature Reviews Cardiology, 2011. **8**(3): p. 131-139.
15. Schaar, J.A., et al., *Intravascular palpography for vulnerable plaque assessment.* J Am Coll Cardiol, 2006. **47**(8 Suppl): p. C86-91.
16. Tearney, G.J., et al., *Consensus Standards for Acquisition, Measurement, and Reporting of Intravascular Optical Coherence Tomography Studies: A Report From the International Working Group for Intravascular Optical Coherence Tomography Standardization and Validation.* Journal of the American College of Cardiology, 2012. **59**(12): p. 1058-1072.
17. van Soest, G., et al., *Atherosclerotic tissue characterization in vivo by optical coherence tomography attenuation imaging.* Journal of Biomedical Optics, 2010. **15**(1): p. 011105-9.
18. Jansen, K., G. van Soest, and A.F.W. van der Steen, *Intravascular Photoacoustic Imaging: A New Tool for Vulnerable Plaque Identification.* Ultrasound in medicine & biology, 2014. **40**(6): p. 1037-1048.
19. Gardner, C.M., et al., *Detection of lipid core coronary plaques in autopsy specimens with a novel catheter-based near-infrared spectroscopy system.* JACC Cardiovasc Imaging, 2008. **1**(5): p. 638-48.
20. Waxman, S., et al., *In Vivo Validation of a Catheter-Based Near-Infrared Spectroscopy System for Detection of Lipid Core Coronary Plaques: Initial Results of the SPECTACL Study.* J Am Coll Cardiol Img, 2009. **2**(7): p. 858-868.
21. Niccoli, G., et al., *Advances in mechanisms, imaging and management of the unstable plaque.* Atherosclerosis, 2014. **233**(2): p. 467-477.
22. Vinegoni, C., et al., *Indocyanine Green Enables Near-Infrared Fluorescence Imaging of Lipid-Rich, Inflamed Atherosclerotic Plaques.* Science Translational Medicine, 2011. **3**(84): p. 84ra45.
23. Ughi, G.J., et al., *Clinical Characterization of Coronary Atherosclerosis With Dual-Modality OCT and Near-Infrared Autofluorescence Imaging.* JACC: Cardiovascular Imaging.
24. Nadkarni, S.K., et al., *Characterization of atherosclerotic plaques by laser speckle imaging.* Circulation, 2005. **112**(6): p. 885-892.
25. van Soest, G., A.F.W. van der Steen, and E. Regar, *Autofluorescence: A New NIR on the Block∗.* JACC: Cardiovascular Imaging.
26. Jansen, K., G. van Soest, and T. van der Steen, *Photoacoustic Imaging of Coronary Arteries: current status and potential clinical application*, in *Coronary atherosclerosis: current management and treatment*, C. Arampatzis, et al., Editors. 2012, Informa Healthcare: London, UK. p. 166-174.

27. Schoenhagen, P. and D.G. Vince, *Intravascular Photoacoustic Tomography of Coronary AtherosclerosisRiding the Waves of Light and Sound∗.* Journal of the American College of Cardiology, 2014. **64**(4): p. 391-393.
28. Fleming, C.P., et al., *Depth resolved detection of lipid using spectroscopic optical coherence tomography.* Biomedical Optics Express, 2013. **4**(8): p. 1269-1284.
29. Hansson, G.K., *Inflammation, atherosclerosis, and coronary artery disease.* New England Journal of Medicine, 2005. **352**(16): p. 1685-1695.
30. Tearney, G.J., et al., *Quantification of macrophage content in atherosclerotic plaques by optical coherence tomography.* Circulation, 2003. **107**: p. 113-119.
31. Wang, B., et al. *Intravascular photoacoustic imaging of macrophages using molecularly targeted gold nanoparticles*. in *BiOS*. 2010. International Society for Optics and Photonics.
32. Wang, B., et al., *Plasmonic intravascular photoacoustic imaging for detection of macrophages in atherosclerotic plaques.* Nano Letters, 2009. **9**(6): p. 2212-2217.
33. Razansky, D., et al., *Multispectral Optoacoustic Tomography of Matrix Metalloproteinase Activity in Vulnerable Human Carotid Plaques.* Mol Imaging Biol, 2011.
34. Wu, C., et al., *A novel photoacoustic nanoprobe of ICG@ PEG-Ag 2 S for atherosclerosis targeting and imaging in vivo.* Nanoscale, 2016.
35. Hui, J., et al., *High-speed intravascular photoacoustic imaging at 1.7 μm with a KTP-based OPO.* Biomedical Optics Express, 2015. **6**(11): p. 4557-4566.
36. Wang, P., et al., *High-speed Intravascular Photoacoustic Imaging of Lipid-laden Atherosclerotic Plaque Enabled by a 2-kHz Barium Nitrite Raman Laser.* Scientific reports, 2014. **4**.
37. Jansen, K., et al. *An intravascular photoacoustic imaging catheter*. in *International Ultrasonics Symposium (IUS), 2010 IEEE*. 2010.
38. Li, X., et al., *Intravascular photoacoustic imaging at 35 and 80 MHz.* Journal of Biomedical Optics, 2012. **17**(10): p. 106005-1.
39. Jansen, K., et al., *Intravascular photoacoustic imaging of human coronary atherosclerosis.* Opt Lett, 2011. **36**(5): p. 597-9.
40. Takaoka, M., et al., *Periadventitial adipose tissue plays a critical role in vascular remodeling.* Circulation research, 2009. **105**(9): p. 906-911.
41. Lundberg, B., *Chemical-Composition and Physical State of Lipid Deposits in Atherosclerosis.* Atherosclerosis, 1985. **56**(1): p. 93-110.
42. Stegemann, C., et al., *Comparative Lipidomics Profiling of Human Atherosclerotic Plaques / Clinical Perspective.* Circulation: Cardiovascular Genetics, 2011. **4**(3): p. 232-242.
43. Tsai, C.L., J.C. Chen, and W.J. Wang, *Near-infrared absorption property of biological soft tissue constituents.* J Med Biol Eng, 2001. **21**(1): p. 7-14.
44. Piao, Z., et al., *High speed intravascular photoacoustic imaging with fast optical parametric oscillator laser at 1.7 μm.* Applied physics letters, 2015. **107**(8): p. 083701.

Chapter 2. Impact of device geometry on the imaging characteristics of an intravascular photoacoustic catheter.

Min Wu, Krista Jansen, Geert Springeling, Antonius F.W. van der Steen, Gijs van Soest, . Impact of device geometry on the imaging characteristics of an intravascular photoacoustic catheter. *Applied Optics 2014;* 53(34): 8131-8139.

Abstract

A basic requirement for intravascular photoacoustic (IVPA) imaging catheters is the delivery of light lies within the ultrasonic field of view. Size and manufacturing constraints favor probe designs with offset optical and acoustic beams. This non-collinear dual beam arrangement leads to a curved PA point spread function (PSF). In this work, we characterize the three-dimensional shape of the PSF for IVPA imaging in clear and optically scattering media. We show that the product of the two beam profiles can accurately model the measured peak response in clear and scattering media. We discuss the impact of the PSF shape and its relation to probe construction. We test imaging capability of the catheter on a phantom and a human artery ex vivo.

2. 1 Introduction

Acute events following atherosclerotic plaque rupture such as myocardial infarction and stroke are the leading causes of death and disability in the developed world [1]. Plaques prone to rupture are known as vulnerable plaques, which are generally characterized by a lipid-rich necrotic core with an overlying thin fibrous cap infiltrated by macrophages [2, 3]. The vulnerability of an atherosclerotic plaque is associated with the morphology and composition of the plaque [4]. Thus, development of coronary imaging modalities to detect structural and compositional plaque characteristics has been the subject of intensive preclinical and clinical research [5].

Intravascular photoacoustic (IVPA) imaging, a catheter-based optical-acoustic hybrid modality, has the potential to image atherosclerotic plaques in unprecedented chemical detail. Absorption of a short light pulse in tissue generates an ultrasound wave that can be detected by a transducer. This makes it possible to image the vessel wall anatomy, employing the chemical specificity of the optical absorption spectra to identify different tissue types. By selecting the excitation wavelength, various tissue types inside the vessel wall can be characterized. Several recent studies [6-11] have shown promising applications of IVPA imaging. Especially, the capability of spectroscopic IVPA (sIVPA) to detect lipid content in human coronary atherosclerotic arteries ex vivo has been demonstrated [12, 13]. Successful in vivo IVPA imaging of lipids in an abdominal aorta of a Watanabe heritable hyperlipidemic (WHHL) -rabbit aorta has also been presented recently [14].

Several design decisions affect the performance of catheters for IVPA imaging, and other forms of photoacoustic endoscopy as well [15]. In this work, we assume that an IVPA catheter must also be capable of intravascular ultrasound (IVUS) imaging, to provide a conventional pulse-echo image of tissue structure, to complement a photoacoustic image of tissue composition. An integrated IVUS/IVPA catheter normally consists of a broadband ultrasonic transducer, which can transmit and receive acoustic waves, and an optical port to deliver the laser light to illuminate the vessel wall. Various designs of integrated US/PA endoscopes, either all optical [16] or piezoelectric material based [17-21], have been proposed. The smallest catheter reported to date is 1.1 mm in diameter, and uses focused illumination for optical-resolution PA imaging [22].

In PA imaging, the received PA signal $V(r)$ from a source at position r can be written as $V(r) \propto p_0(r) * h(r)$, where $*$ denotes convolution, $h(r)$ is the transducer spatial impulse response and $p_0(r)$ is the source pressure [23]. The spatial impulse response $h(r)$ of the transducer can be obtained by a hydrophone measurement of the transmitted beam profile, and the source pressure can be expressed as $p_0(r) = \Gamma \mu_a F(r)$, where Γ is Grueneisen parameter (dimensionless), μ_a (cm-1) is the absorption coefficient of tissue and $F(r)$ is the laser fluence [24]. The relative arrangement of optical fiber and ultrasound element has an impact on the imaging characteristics of the probe. If both beams are collinear, the PA and US point spread functions (PSFs) will overlap, though not necessarily coincide. Other designs, either longitudinally [11, 19] or laterally offset [17], are more suitable for miniaturization, but present a more complex structure of the PSF in space. Because of the offset between the optical and acoustic beams,

the PA imaging plane is curved and the longitudinal and lateral resolutions are affected by the beam overlap. The presence of optical scattering by tissue or blood broadens the optical beam, and thus should reduce the curvature.

In this paper, we study the effect of the catheter tip geometry on imaging by quantifying the PSF in terms of three dimensional resolution, and by measuring the offset between the US and PA imaging planes, in water and in a scattering medium. We conclude with a discussion of the implications of our findings for catheter design.

2. 2 Methods

2.2.1 Catheter design parameters

For IVPA imaging, the illuminated area should lie within the field of view of the ultrasound transducer, as illustrated in Fig. 1(a). In a longitudinally offset dual beam design, the optical port of the catheter is positioned proximal from the ultrasound transducer. The beam emanates from the catheter under an angle to illuminate the tissue in front of the transducer. In optimizing the design of the catheter, we studied the effect of the probe geometry on the three-dimensional structure of the PSF. We work with multimode silica optical fiber of NA=0.22, with an angle-polished tip that is covered by a glued-on quartz cap to preserve an air-glass interface (Pioneer Optics, 400 µm core diameter, low OH). If we require that the marginal ray emanating from the fiber still satisfies the total reflection criterion, the maximum angle under which the fiber can be polished is 34°, deflecting the beam by total reflection at a 68° angle. A smaller angle will lead to a more forward-directed beam, which is undesirable. We therefore choose to keep the polishing angle of the fiber tip fixed at this value.

To avoid the acoustic specular reflection of the catheter sheath (not shown in the illustrations) which will be needed for in vivo imaging, the ultrasound transducer can be tilted relative to the catheter central axis. This angle affects the overlap between the optical and ultrasound beams and hence the PSF shape. We fixed the longitudinal offset between the fiber tip and the center of the transducer at the minimum achievable value of 1.1 mm.

We simulated the beam overlap at different tilt angles θ of the transducer (positive clockwise with respect to the probe axis; cf. Fig. 2.1(a)) by computing the PA signal response as the product of the US beam profile and the optical fluence distribution. The US beam profile of the transducer (0.4 x 0.4 mm, lead magnesium niobate-lead titanate [PMN-PT]; center frequency 45 MHz; –6 dB fractional bandwidth of 45%; custom built by the Dept. of Biomedical Engineering, University of Southern California [25]) was measured by a needle hydrophone (75 µm tip, calibrated from 2 to 60 MHz, Precision Acoustics, Dorchester, UK) in clear water at room temperature, and the optical beam profile was simulated assuming a Gaussian beam profile, NA=0.22 for the fiber, and ignoring lensing effects of the quartz cap on the fiber in the plane of the catheter. Both beams profiles are normalized to their respective maxima. The overlap range is defined as the imaging depth where the overlap intensity is more than -25dB (0 dB indicates the complete overlap of the dual beam maxima).

The overlap range and the maximal overlap intensity versus different transducer position angles are plotted in Fig. 2.1(b). The overlap intensity is higher, but with shorter range, at negative

transducer angle, showing a trade-off between sensitivity and viewing depth. The geometry of the intersecting beams for θ = 6°, combined with the contour graph of the PA response, is shown in Fig. 2.1(c). It clearly shows the beam overlap of the catheter,, extending from around 1.3 mm to 6.3 mm from the transducer, with the distance from about 2 to 4mm as the optimal imaging range. It also shows, importantly, that the PA response as indicated by the contour plot does not coincide with the US response, but is shifted proximally for small depths. This means that there is a variable offset between the US and PA images.

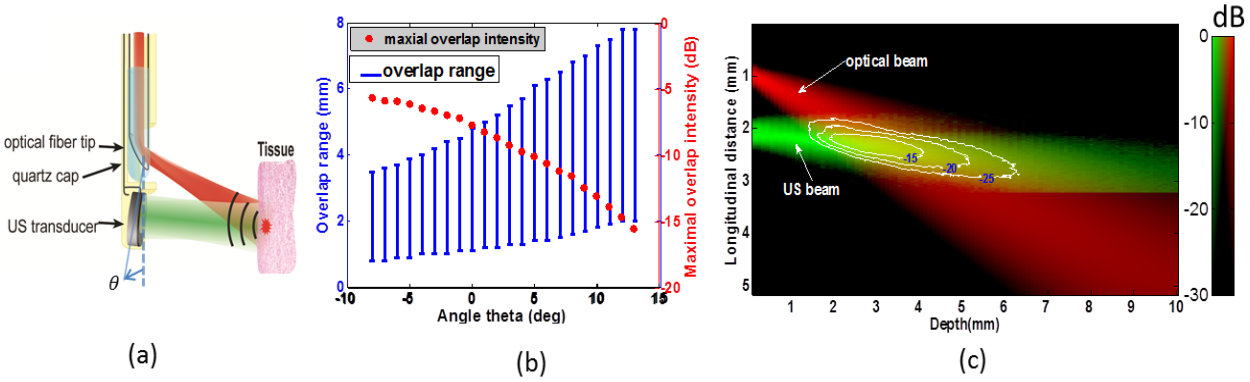

Figure 2.1(a) Schematic of the integrated IVUS/IVPA catheter depicts the light path (red), the US beam path (green) and generated ultrasound signal (black arcs). We vary the transducer tilt angle θ. (b) The dual beam overlap range and maximum overlap intensity versus transducer position angles. The angle is defined with respect to the probe axis and positive clock-wisely (c) US and optical beam profile of the catheter overlaid with contour graph of the overlap intensity in dB. 0 dB corresponds to the maximum response when the beams are fully overlapping.

We built an integrated US/PA probe with an outer diameter of 1 mm. We choose a transducer tilt angle of θ = 6°, which is a reasonable compromise between overlap range and intensity. A gold layer was sputter-deposited on the front of the transducer to serve as an electrode and optical isolation. An outer matching layer of parylene with 14 μm thickness was applied by vapor deposition (Philips Innovation Services, Eindhoven, the Netherlands) on top of the gold layer. The fiber tip and the transducer were mounted in a custom machined stainless steel assembly. The photographs of the catheters in Fig. 2.2 show the transducer configuration (prior to application of the metal film and coating).

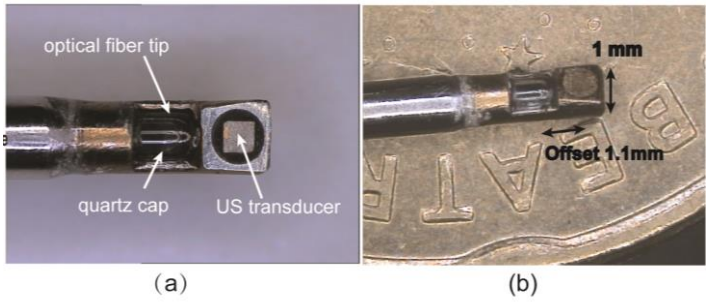

Figure 2. 2 Photographs of the catheter (before application of the gold optical isolation layer) (a) Front view, with light exiting the optical fiber tip. (b) The catheter tip on the edge of a 10 eurocent coin. The outer diameter of the tip is 1.0 mm

2.2.2 Combined IVPA/IVUS imaging system

A diagram of the combined IVPA/IVUS imaging system is illustrated in Fig. 2.3 [11]. The excitation source for photoacoustic imaging was provided by a tunable laser (Vibrant B/355-II, OPOTEK, Santa Clara, CA, USA). It provides high-energy laser pulses at a repetition rate of 10 Hz and a pulse width of 5 ns within 420 to 2200 nm spectral range. The output energy varies with wavelength. A tapered multimode optical fiber (Oxford Electronics, Four Marks, UK; input diameter 1mm; output diameter 360 µm) coupled the laser light to the catheter; typical coupling losses from laser to catheter tip amount to ~80%. For pulse-echo imaging, Gaussian-modulated cosine pulses with a peak-to-peak amplitude of 16 V were generated by an arbitrary waveform generator (WW2571A, Tabor Electronics, Tel Hanan, Israel) and transmitted to the catheter through a custom-built expander and limiter. The received US and PA signals were amplified by a 43 dB amplifier (AU1263, MITEQ, Long Island, New York, USA), band pass filtered (13–60 MHz 5th order Butterworth, custom built) and digitized at a sampling frequency of 350 MHz by a 12-bit data acquisition card (Acqiris DP310, Agilent Technologies, Santa Clara, CA, USA). A pulse/delay generator (BNC model 575, Berkeley Nucleonics Corporation, San Rafael, CA, USA) provided timing and triggering signals upon receiving a master trigger from the Q-switch of the laser. The catheter was translated and rotated by a motorized translation and rotary stage (MP 63-25-DC and DT 105, Steinmeyer GmbH & Co. KG, Albstadt, Germany), respectively.

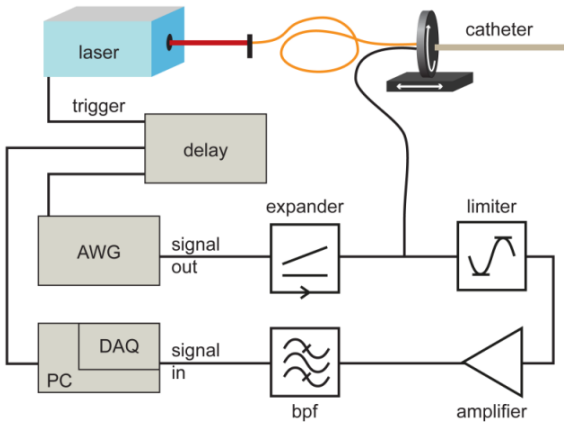

Figure 2.3. Diagram of the combined IVPA/IVUS imaging system; AWG: arbitrary waveform generator, DAQ: data acquisition, delay: pulse/delay generator; bpf: band pass filter.

2.2.3 Experiments

To gain insights into the imaging characteristics of the catheter, measurements on an isolated target at the wavelength of 760 nm (the energy of the laser is about 1 mJ per pulse out of the catheter) were performed. Although contrast for lipid in atherosclerotic plaque tissue is found at wavelengths beyond 1 µm, we chose to work at a wavelength with minimal water and lipid absorption to prevent a background PA signal from affecting the measurements. We characterized the spatial resolution, signal to noise ratio (SNR), and the PA imaging plane curvature. A single 30 µm diameter tungsten wire was used as an isolated target. In the measurement, the image plane was defined as the plane perpendicular to the catheter, containing the image lines. The tungsten wire was first positioned perpendicular to the catheter for measuring the resolution in the axial (along the image line) and longitudinal (parallel to the catheter axis, perpendicular to the imaging plane) directions, and then parallel to the catheter

for the lateral (perpendicular to the catheter in the imaging plane) resolution measurement. In both configurations, a 2D scan in the plane perpendicular to the tungsten wire was performed with the geometry illustrated in Fig. 2.4(a). In US mode, the lateral and longitudinal resolution can be assumed similar based on the symmetric US beam profile.

The measurements were conducted in clear water and in 0.5 vol% intralipid (Intralipid ® 20%, Fresenius Kabi Nederland BV, 's Hertogenbosch, The Netherlands; diluted 1:40 v/v) solution at room temperature. Intralipid is used as the scattering medium, broadening the optical beam to simulate the effect of tissue. At 0.5 vol%, the absorption coefficient of intralipid is μ_a = 0.0024 mm^{-1}, and the reduced scattering coefficient is approximately μ_s' = 0.5 mm^{-1} [26]. It is similar to the optical scattering coefficient in human coronary artery tissue, which is around 0.6 mm^{-1} [27]. The PA imaging curve was determined as the distance from the transducer to the signal maximum at all probe positions in the configuration of the wire perpendicular to the catheter. The spatial resolution was determined from the -6 dB width of the wire signal envelope. The SNR was computed as the difference between the wire signal maximum and background noise level in dB.

Next, we imaged a cylindrical vessel phantom and a human coronary artery to evaluate the imaging capability of the catheter. The vessel phantom is made of 10% poly-vinyl-alcohol (PVA) with 1% enamel paint as acoustic scatters (three freeze/thaw cycles of at least 2h) and has a 3 mm diameter lumen. Six metallic wires of 100 µm diameter located at 1.5 to 4 mm distance from the lumen were incorporated as targets. Each cross sectional image consists of 360 imaging lines at 1° spacing. A human coronary artery (left anterior descending artery, male, 80 years old) was collected at autopsy from the Department of Pathology of the Erasmus Medical Center (MC), after obtaining consent from the relatives and approval of the research protocol by the Medical Ethics Committee of the Erasmus MC (MEC-2007-081). The coronary artery was frozen within 2h at -80°, then thawed and measured 13 months later. After imaging, Oil Red O (ORO) staining was performed at the imaging cross section to identify lipids in the artery (lipids are stained red in ORO staining).

All the stored raw data were digitally band pass filtered between 10 and 70 MHz, using a 100^{th} order zero-phase forward and reverse finite impulse response (FIR) filter. All PA and US data were subsequently Tukey windowed and envelope filtered. The vessel phantom and human artery data were first scan-converted to Cartesian coordinates, and then logarithmically compressed for display.

2.3 Result

2.3.1 Spatial resolution and SNR

Figure 2.4 shows the spatial resolutions and SNRs of the catheter on the PA/US measurement of a 30 µm diameter tungsten wire at different depths (black dots are in clear water and red dots are in 0.5 vol% intralipid solution). As expected, the US images are not affected by the introduction of intralipid. The highest US SNR is 60 dB at the depth of 1.5 mm. The US axial resolution is independent of depth at approximately 43 µm while the lateral resolution keeps

increasing with depth in the far field of the transducer. In PA images, the intralipid only affects the SNR. The highest PA SNR is 63dB at the depth of 2.2 mm in clear water. After introduction of 0.5 vol% intralipid, the PA SNR decreases at all depths, typically 10~20 dB at depths greater than 1.4 mm. The maximum PA SNR is 43 dB at the depth of 1.5 mm. The PA axial resolution is independent of depth at around 52 μm. The lateral resolution (in the image plane) increases from 125 to 400 μm at depths from 1 to 4 mm. The PA longitudinal resolution increases from 400 μm close to the probe to 2000 μm at depths up to 8 mm.

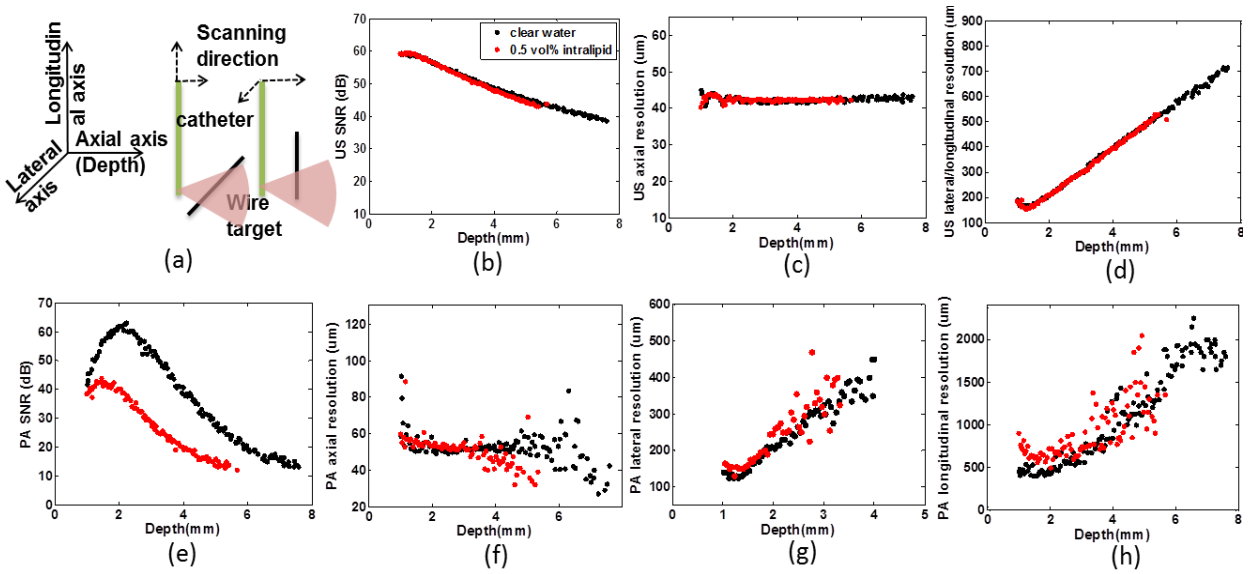

Figure 2.4. The spatial resolutions and SNRs of the probe on the measurement of a 30 μm tungsten wire in clear water (black dots) and 0.5 vol% intralipid solution (red dots). (a) The geometry of the measurements. (b-d) The SNR and spatial resolutions of the US images. (e-h) The SNR and spatial resolutions of the PA images.

To quantify the spatial resolution and SNR of the catheter, the spatial resolution and SNR at the natural focus of the transducer (2.1 mm for this transducer) in clear water were used. The results are listed in Table 2.1.

Table 2.1. Resolutions and SNRs of PA and US measurements on the single tungsten wire in clear water at the natural focus of the transducer

Imaging Modality	Resolution (μm)			SNR (dB)
	Axial	Lateral	Longitudinal	
PA	52	215	500	62
US	43	205		60

2.3.2 IVPA imaging plane curvature

The mismatch between the US and PA PSF leads to a longitudinal shift of the signal received from the single wire target by both modalities, which is shown in Fig. 2.5(b, c). In the figure, there is an offset of approximately 0.5 mm between US and PA signals in clear water (cf. Fig. 2.5(b)). Introduction of optical scattering leads to a broader optical beam and a more uniform light fluence distribution. The offset is resolved, albeit at a cost of SNR owing to the fluence reduction (cf. Fig. 2.5(c)). The PA imaging plane curve of the catheter in clear water (white dots) overlaid on the combined PA beam profile (from Fig. 2.3) is shown in Fig. 2.5(d). Similarly, the PA beam profile in 0.5 vol% intralipid can be computed by the product of the measured US profile and the simulated optical beam profile using Monte Carlo method. Fig. 2.5(e) shows the PA beam profile in 0.5 vol% intralipid overlaid with the PA imaging plane curve of the catheter (white dots). The measured PA imaging curve agrees well with the computed overlap of the optical and ultrasound beams in both clear and optical scattering medium. Figure 2.5(f) shows the offsets between PA and US imaging planes in clear water (black dots) and in 0.5 vol% intralipid (red dots). In clear water, the PA and US imaging planes intersect at the depth of 2.7 mm, as expected from the probe geometry (the face angle of the polished fiber and the distance between the fiber tip and the transducer). Up to a depth of about 7 mm, the offset between PA and US imaging planes is within [-1 0.5] mm. After introduction of 0.5 vol% intralipid to the water, the offset is reduced to [-0.1 0.3] mm, practically vanishing beyond the intersection point.

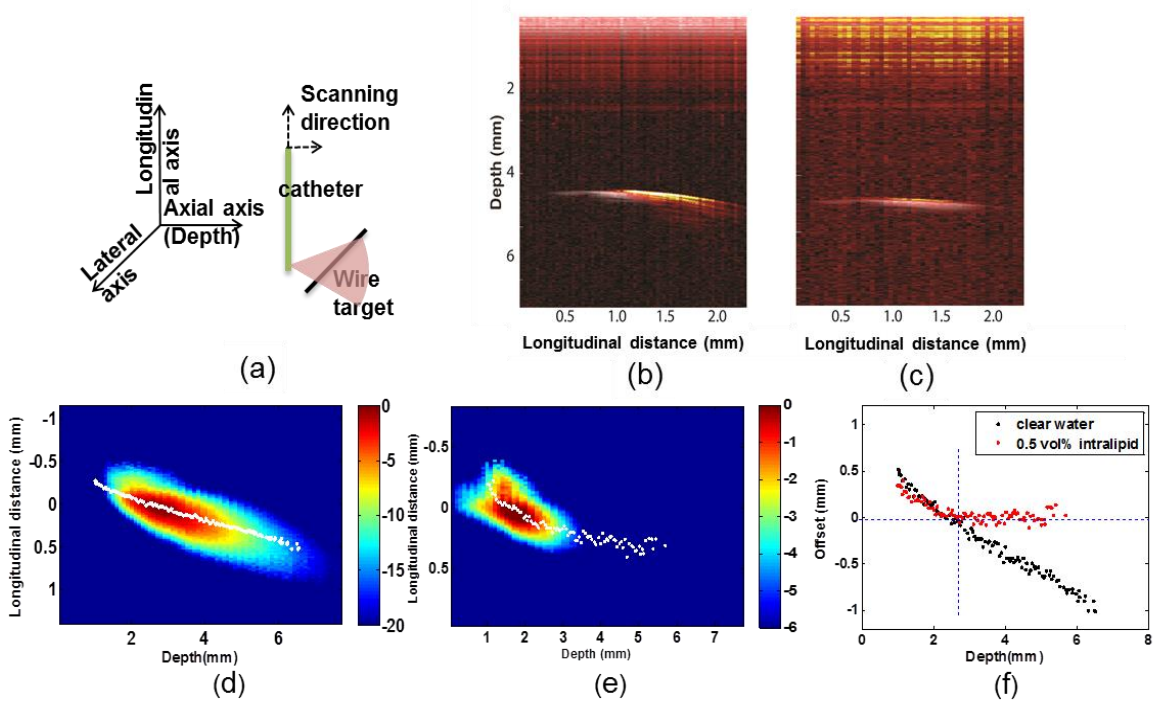

Figure 2.5. The PA imaging point spread function in the catheter plane. (a) The configuration of the measurements. (b) fused PA/US image of the single wire in water. (c) fused PA/US image of the single wire in 0.5 vol% intralipid solution (d) and (e) are PA imaging curve overlaid on the graph of the dual beam overlap in clear water (d) and in 0.5 vol% intralipid (e). In both figures, the longitudinal distance 0 is the position with maximal intensity. (f) the offset between PA and US imaging plane in longitudinal direction in clear water (black dots) and 0.5 vol% intralipid solution (red dots).

2.3.3 Imaging capability

2.3.3.1 Vessel-mimicking phantom

The images of the vessel phantom are presented in Fig. 2.6. All 6 wires are clearly visible. In the PA image, reverberation or 'comet-tail' artefacts [28] can be seen behind the wires close to the transducer. In the US image, the center ring is caused by the 'ringing' of the transducer during the transmission of ultrasound pulses.

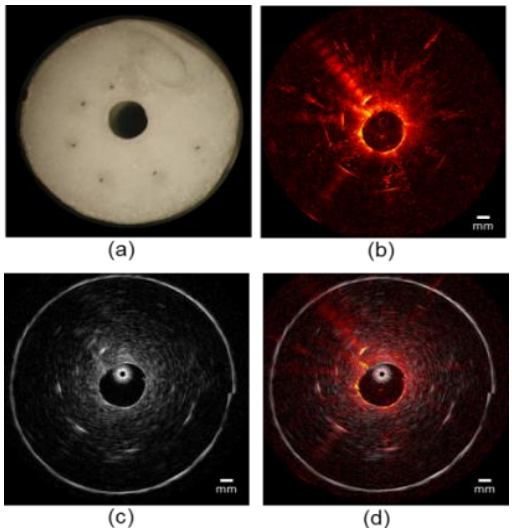

Figure 2.6. Images of the cylindrical vessel phantom. (a) Photograph of the phantom, taken from the top. (b) PA image; (c) US image; (d) Overlaid PA/US image of the vessel phantom. The dynamic range is 45 dB in the PA image and 50 dB in the US image.

2.3.3.2 Human coronary artery

Figure 2.7 shows the co-registered IVPA/IVUS ex vivo images of the artery at the wavelength of 1205 nm (high lipid absorption). In the IVUS image (cf. Fig. 2.7(a)), the border of the artery is clearly visible from 5:00 to 2:00 o'clock position. In the IVPA image (cf. Fig. 2.7(b)), there are bright signals from 12:00 to 9:00 o'clock position inside the artery wall, indicating the presence of a lipid-rich plaque. There are also bright signals mapping the lipids in peri-adventitial tissue observed from 6:00 to 12:00 o'clock position outside the artery wall. All the locations of the lipid regions were confirmed by the ORO histological data (lipids are red).

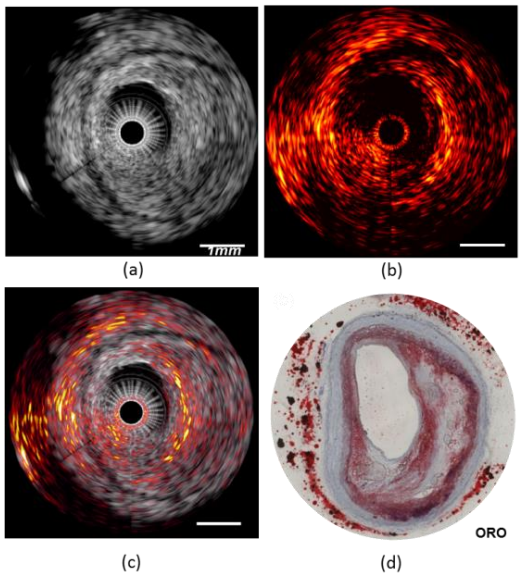

Figure 2.7. Cross-sectional IVPA and IVUS images of the human artery. (a) US image of the human artery, dynamic range is 45 dB; (b) PA image of the human artery, dynamic range is 25 dB; (c) The fused PA and US image of the human artery; (d) Histology: Oil Red O stain of the IVPA and IVUS imaging cross section (lipids are shown in red).

2.4 Discussion and summary

We presented a design study of an integrated photoacoustic and ultrasound catheter for combined IVPA/IVUS imaging. We characterized and quantified its imaging characteristics by a measurement on isolated targets. PA and US axial resolutions are 52 and 43 μm respectively, while the lateral resolutions are 215 and 205 μm at the natural focus distance, respectively. The SNR at this location was more than 60 dB for US in clear water and in 0.5% intralipid, as well as for PA in clear water; in 0.5% intralipid the maximum PA SNR dropped to 43 dB. This decrease is the effect of lower fluence in the scattering medium compared to clear water. The imaging performance of the probe was demonstrated by measurements on a cylindrical vessel phantom containing metal wires and an atherosclerotic human coronary artery. A usable imaging range of 8 mm was demonstrated, which is almost double that of the previous high-resolution devices [17].

The IVPA imaging plane is curved due to the non-collinear beams. The spatial PA response can be accurately modeled by a simple product of the overlapping beams in clear and optical scattering medium, which makes it a useful design tool for PA probes. The simulated fluence distribution in a scattering medium depends on the input optical properties, which not be exactly known. The PA and US imaging planes are shifted by $[-1\ 0.5]$ mm up to 7 mm from the transducer. The design variables that can be used to reduce this offset are minimization of the distance between the fiber tip and transducer, and use of a large-NA fiber (which leads to increased bending losses in a flexible rotating probe). Optical scattering broadens the optical beam and flattens the fluence distribution, largely restoring the alignment between the PA and US imaging planes. For targets close to the transducer, the offset may not vanish entirely, as the light needs a certain propagation distance to diffuse sufficiently.

We attempted to simulate tissue optics by adding a scattering agent to the water bath in the experiments. It is as yet unclear if flushing of the blood, as is done in OCT [29] is preferable for in vivo IVPA [7, 14]. The details of the PSF shape in actual use will depend on the presence and optical density of blood [30] as well as the tissue optical properties of the vessel wall. In a vessel filled with clear flush media, 2-4 mm is an ideal imaging range for a catheter that is centered in the vessel. If the catheter is eccentric, which happens often, the far wall is still visible through the clear flush media. The near wall provides optical scattering, which brings the beam overlap point closer to the catheter, in the adjacent tissue.

It is interesting to consider the effect of the non-collinear beams on other probe geometries. The parallel arrangement of fiber and transducer presented in [17] should still give rise to a curved point spread function in the imaging plane, although the close separation between the optical and ultrasonic beams in that device will minimize PSF curvature. Instead, transducer sidelobes were observed in the PA signal for close-range targets. In that study, optical scattering was not investigated, nor was there a comparison with a simulated beam profile.

We measured a large difference in the PA resolutions in the longitudinal and lateral directions. The lateral resolution remained comparable to the ultrasound resolution over the entire imaging range, apparently limited by ultrasound beam width within the much broader illumination beam. The longitudinal resolution, however, is limited by the non-collinear catheter design, increasing to nearly 2 mm at a depth of 7 mm. In the longitudinally offset catheter design discussed in this study, it would mean that the resolution along the pullback direction would be compromised, but resolution in the cross-sectional images is preserved. The difference can likely be attributed to an asymmetry in the optical beam characteristics, possibly caused by the detailed structure of the optical tip and lensing by one of the curved surfaces. However, we could not characterize the fiber tip with sufficient accuracy to simulate the effect on the beam.

The USC ultrasound transducer used in this study has excellent sensitivity, resulting in superior SNR, compared to many earlier designs, and the good axial and lateral resolutions benefit the cross-sectional images. Besides, its small size allows further reduction of the catheter diameter. Whether the frequency of 45 MHz is optimal for imaging of coronary atherosclerosis is the subject of ongoing experiments. The offset between optical and ultrasonic beams can be minimized by placing the transducer as close to the optical fiber tip as possible and using thinner fibers, which will also enable a further decrease in size to 0.7 mm tip diameter.

We observe a PA transmit artifact, which can be seen as the near-field signal in Fig. 2.5 (a) and (b). A photoacoustic signal can be generated directly in the transducer or in the transducer housing which is in mechanical contact with the transducer, if the light is absorbed by the probe itself. This signal appears immediately after the emission of the laser pulse, as there is no time of flight. In the presence of optical scattering, the light fluence close to the probe is higher and the signal is proportionally larger. An effect of the probe geometry is the reduced transducer light exposure with larger positive tilt angles (transducer is tilted away from optical fiber).

Anecdotally, we compared the strength of this artefact generated by the probe discussed in this paper with a previous prototype using a tip made out of polyether ether ketone (PEEK) [19].

Figure 2.8 shows that the stainless steel tip probe exhibits an artefact that is about 10 dB stronger and extends for > 2 μs after the laser pulse. This difference may be explained by assuming that the white PEEK tip of the 30 MHz catheter is non-absorbing, and any vibrations quickly decay by dissipation in the mounting epoxy. Covering the transducer front surface with a metal film is essential to minimize this unwanted signal. The steel tip, however, holds the optical fiber tip itself and cannot be effectively shielded from the light. Vibrations excited in this metal structure also persist for longer, leading to a more prominent artifact.

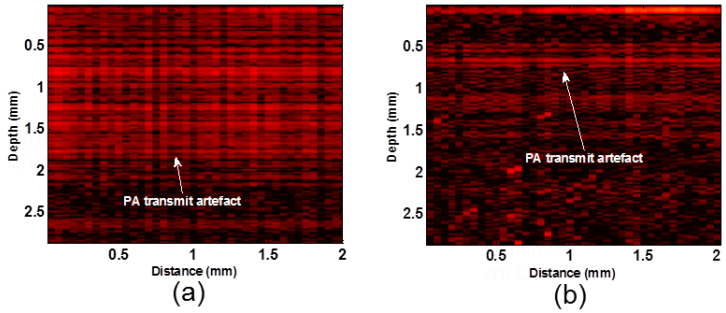

Figure 2. 8. PA images showing the transmit artefact. (a) PA image with the steel tip 45 MHz catheter and (b) PA image with the white PEEK tip 30 MHz catheter. The dynamic range is 60 dB in both images.

In summary, we evaluated the design of an intravascular ultrasound/photoacoustic imaging probe. We demonstrated the various geometrical considerations affecting the PA PSF. Experiments showed how optical scattering can at least partially mitigate the complexity of the spatial response introduced by the choices made in the design of the catheter tip. There is a trade-off between viewing depth and sensitivity resulting from the overlap between the optical and ultrasound beams. Finally, we discussed how the tip design can minimize light absorption in the catheter tip, which creates a prominent artifact that is difficult to avoid with a small probe used in reflection geometry.

Acknowledgments

This work was funded by the Dutch Technology Foundation (STW) through the 2007 Simon Stevin Meester grant (STW 10040) to A.F.W. van der Steen. We thank X. Li (Department of Biomedical Engineering, University of Southern California) for providing ultrasound transducers.

References

1. Waksman, R., P.W. Serruys, and J. Schaar, *Handbook of the vulnerable plaque*. 2004: Martin Dunitz.
2. Virmani, R., et al., *Pathology of the vulnerable plaque.* J Am Coll Cardiol, 2006. **47**(8 Suppl): p. C13-8.
3. Kolodgie, F.D., et al., *The thin-cap fibroatheroma: a type of vulnerable plaque - The major precursor lesion to acute coronary syndromes.* Current Opinion In Cardiology, 2001. **16**(5): p. 285-292.

4. Schaar, J.A., et al., *Intravascular palpography for vulnerable plaque assessment.* J Am Coll Cardiol, 2006. **47**(8 Suppl): p. C86-91.
5. Van Mieghem, C.A., et al., *Noninvasive detection of subclinical coronary atherosclerosis coupled with assessment of changes in plaque characteristics using novel invasive imaging modalities: the Integrated Biomarker and Imaging Study (IBIS).* J Am Coll Cardiol, 2006. **47**(6): p. 1134-42.
6. Sethuraman, S., et al., *Spectroscopic intravascular photoacoustic imaging to differentiate atherosclerotic plaques.* Optics Express, 2008. **16**(5): p. 3362-3367.
7. Wang, B., et al., *Intravascular photoacoustic imaging of lipid in atherosclerotic plaques in the presence of luminal blood.* Opt Lett, 2012. **37**(7): p. 1244-6.
8. Wang, B., et al., *Detection of macrophages and lipid using ultrasound guided spectroscopic intravascular photoacoustic imaging.* The Journal of the Acoustical Society of America, 2011. **129**(4): p. 2642-2642.
9. Allen, T.J., et al., *Spectroscopic photoacoustic imaging of lipid-rich plaques in the human aorta in the 740 to 1400 nm wavelength range.* Journal of Biomedical Optics, 2012. **17**(6): p. 061209-10.
10. Yeager, D., et al., *Intravascular Photoacoustics for Image-Guidance and Temperature Monitoring During Plasmonic Photothermal Therapy of Atherosclerotic Plaques: A Feasibility Study.* Theranostics, 2014. **4**(1): p. 36.
11. Jansen, K., et al., *Intravascular photoacoustic imaging of human coronary atherosclerosis.* Opt. Lett., 2011. **36**(5): p. 597-599.
12. Jansen, K., et al., *Lipid detection in atherosclerotic human coronaries by spectroscopic intravascular photoacoustic imaging.* Optics Express, 2013. **21**(18): p. 21472-21484.
13. Jansen, K., et al., *Spectroscopic intravascular photoacoustic imaging of lipids in atherosclerosis.* Journal of Biomedical Optics, 2014. **19**(2): p. 026006-026006.
14. Wang, B., et al., *In vivo Intravascular Ultrasound-guided Photoacoustic Imaging of Lipid in Plaques Using an Animal Model of Atherosclerosis.* Ultrasound in Medicine and Biology, 2012(0).
15. Yang, J.-M., et al., *Simultaneous functional photoacoustic and ultrasonic endoscopy of internal organs in vivo.* Nature Medicine, 2012. **18**(8): p. 1297-1302.
16. Hsieh, B.Y., et al., *All-optical scanhead for ultrasound and photoacoustic dual-modality imaging.* Opt Express, 2012. **20**(2): p. 1588-96.
17. Li, X., et al., *Intravascular photoacoustic imaging at 35 and 80 MHz.* Journal of Biomedical Optics, 2012. **17**(10).
18. Karpiouk, A.B., B. Wang, and S.Y. Emelianov, *Development of a catheter for combined intravascular ultrasound and photoacoustic imaging.* Review of Scientific Instruments, 2010. **81**(1): p. 014901-1-7.
19. Jansen, K., et al. *An intravascular photoacoustic imaging catheter*. in *International Ultrasonics Symposium (IUS), 2010 IEEE*. 2010.
20. Wang, B., A. Karpiouk, and et al., *Design of Catheter for Combined Intravascular Photoacoustic and Ultrasound Imaging.* 2008 Ieee Ultrasonics Symposium, 2008(Vols 1-4 and Appendix:): p. 1150-1153.
21. Hsieh, B.-Y., et al. *Design and fabrication of an integrated intravascular ultrasound/photoacoustic scan head*. in *BiOS*. 2010. International Society for Optics and Photonics.
22. Bai, X., et al., *Intravascular Optical-Resolution Photoacoustic Tomography with a 1.1 mm Diameter Catheter.* PloS one, 2014. **9**(3): p. e92463.
23. Jensen, J.A., *Linear description of ultrasound imaging systems.* Notes for the International Summer School on Advanced Ultrasound Imaging, Technical University of Denmark July, 1999. **5**.

24. Wang, L.V., *Photoacoustic imaging and spectroscopy*. 2009: CRC press.
25. Zhou, Q., et al., *PMN-PT single crystal, high-frequency ultrasonic needle transducers for pulsed-wave Doppler application.* IEEE Trans Ultrason Ferroelectr Freq Control, 2007. **54**(3): p. 668-75.
26. Michels, R., F. Foschum, and A. Kienle, *Optical properties of fat emulsions.* Optics Express, 2008. **16**(8): p. 5907-5925.
27. van Gemert, M.J., et al., *Optical properties of human blood vessel wall and plaque.* Lasers in surgery and medicine, 1985. **5**(3): p. 235-237.
28. Ziskin, M.C., et al., *The comet tail artifact.* Journal of Ultrasound in Medicine, 1982. **1**(1): p. 1-7.
29. Tearney, G.J., et al., *Consensus Standards for Acquisition, Measurement, and Reporting of Intravascular Optical Coherence Tomography Studies: A Report From the International Working Group for Intravascular Optical Coherence Tomography Standardization and Validation.* Journal of the American College of Cardiology, 2012. **59**(12): p. 1058-1072.
30. Roggan, A., et al., *Optical properties of circulating human blood in the wavelength range 400-2500 NM.* Journal Of Biomedical Optics, 1999. **4**(1): p. 36-46.

Chapter 3. Specific imaging of atherosclerotic plaque lipids with two-wavelength intravascular photoacoustics

Wu M, Jansen K, van der Steen A F W, et al. Specific imaging of atherosclerotic plaque lipids with two-wavelength intravascular photoacoustics. *Biomedical optics express, 2015, 6(9): 3276-3286.*

Abstract

The lipid content in plaques is an important marker for identifying atherosclerotic lesions and disease states. Intravascular photoacoustic (IVPA) imaging can be used to visualize lipids in the artery. In this study, we further investigated lipid detection in the 1.7-μm spectral range. By exploiting the relative difference between the IVPA signal strengths at 1718 and 1734 nm, we could successfully detect and differentiate between the plaque lipids and peri-adventitial fat in human coronary arteries ex vivo. Our study demonstrates that IVPA imaging can positively identify atherosclerotic plaques using only two wavelengths, which could enable rapid data acquisition in vivo.

3.1 Introduction

The rupture of vulnerable atherosclerotic plaques is a major cause of acute cardiovascular events and sudden cardiac death [1]. One of the most common types of vulnerable atherosclerotic plaques is the thin-cap fibroatheroma (TCFA). It is characterized by the thin fibrous cap with macrophage infiltration, covering a lipid rich necrotic core [2, 3]. Lipid in particular is a crucial component and is used as a biomarker for detecting atherosclerotic plaques [4-7]. A technology that directly, specifically and reliably images plaque lipid content can be used for guiding diagnosis and interventions without observer-dependent and time-consuming interpretation. Such a technology is presently not available for use in patients.

Intravascular photoacoustic (IVPA) imaging is a new catheter-based hybrid optical-acoustic modality for imaging atherosclerotic plaques which could meet that clinical need [8-10]. It can detect lipids on the basis of optical absorption contrast. However, choosing the wavelengths most suitable for lipid detection by IVPA imaging is critical. We know that lipids are highly effective absorbers at wavelengths near 1.7 μm and 1.2 μm due to the first and second overtone of the vibration of C-H bonds within lipid molecules [4, 11, 12]. The capability of IVPA imaging to detect lipids at both spectral ranges in the coronary arteries has been demonstrated ex vivo [13, 14] and in vivo [15]. In a typical atherosclerotic artery, lipids can be found in the plaque inside the artery wall, while peri-adventitial fat is present around the artery wall also in normal coronary arteries in the aging heart. While lipids in the plaque mainly consist of cholesterol and certain cholesteryl esters [16, 17], the lipids in the peri-adventitial fat are stored as a mixture of fatty acids [18, 19]. This difference makes it possible to differentiate between these two lipids. Peri-adventitial fat is distributed around arteries throughout the body [20]. A modality that visualizes only lipids in plaques, excluding peri-adventitial fat, can highlight the presence and location of lipid-rich plaques (LRP) in vessel cross-sections and longitudinal sections through a pullback data set, without having to rely on IVUS image analysis. Unique LRP detection can be a valuable tool for guidance of percutaneous coronary interventions (PCI).

A number of recent studies advocated the use of a single wavelength for lipid imaging [11, 15].We observed that other plaque components may also generate a signal at that chosen wavelength, as is illustrated in Fig. 3.1. In the figure, only the PA signal from 1 o'clock to 3 o'clock (in the light blue box) was generated from plaque lipids. The signals from 3 o'clock to 7 o'clock inside the vessel (in the green box) were generated from calcium (black in the ORO stained section), while the strong signal surrounding the vessel from 9 o'clock to 3 o'clock was generated from the peri-adventitial adipose tissue. The observation shows that reliable lipid detection requires multiple wavelengths. We have previously investigated the possibility of specific plaque lipid imaging using IVPA [13, 21], and demonstrated that lipids in plaques can be differentiated from those in peri-adventitial fat using the correlation between the observed PA spectra data and the reference PA spectra data. This analysis requires at least 3 wavelengths in the 1.2 μm range. However, using multiple wavelengths impacts the complexity, cost, and speed of the imaging system, and hence the viability of IVPA as a clinical imaging technique.

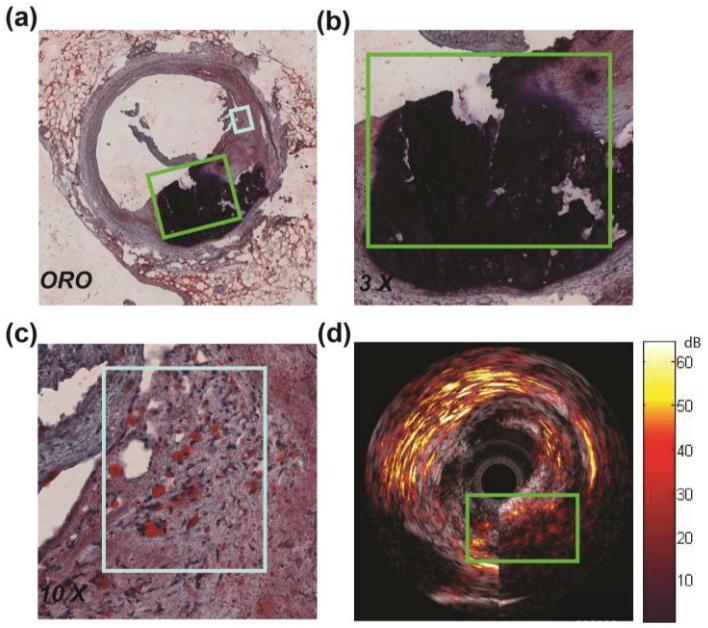

Figure 3.1. Ex vivo IVPA/IVUS image of a human coronary artery. (a) Histology: Oil Red O staining of the imaging cross session. (b) 3 x magnification of a part of vessel wall (area outlined in green in (a)). (c) 10 x magnification of a part of vessel wall (area outlined in light blue in (a)). (d) 1710 nm combined IVPA/IVUS images of the same cross session shown in (a). The image also shows a strong signal from the adipose tissue surrounding the vessel from 9 o'clock to 3 o'clock. The dynamic range is 55 dB in the US image and 22 dB in the PA image.

The larger absorption coefficient of lipids in the 1.7 µm wavelength band allows us to work at lower laser pulse energies (compared to 1.2 µm) to achieve a reliable PA signal, which is attractive for safety, cost and usability of the technology in a real-world clinical setting.

In this work, based on the statistical analysis of the spectra of different lipid samples, we present a method to automatically detect and differentiate plaque lipids using only two wavelengths in the 1.7 µm range, enabling a fast image acquisition for in vivo application. The performance of this presented method was tested on a vessel phantom and on ex vivo human coronary arteries.

3.2 Method and material

3.2.1 Imaging system

We used a combined IVPA/IVUS imaging system to obtain co-registered IVPA/IVUS images as described before [13, 22]. Briefly, the laser pulses for IVPA imaging were provided by a tuneable laser (Vibrant B/355-II, OPOTEK, Santa Clara, CA, USA; Pulse energy 650 µJ/pulse at 1700 nm, pulse duration 5 ns, repetition rate 10 Hz). The laser light was coupled into the custom built catheter by a tapered multimode optical fiber (Oxford Electronics, Four Marks, UK; input diameter 1 mm; output diameter 360 µm). Our catheter mainly comprised a 400 µm diameter core optical fiber with an angle-polished tip (Pioneer Optics, Hartford, Connecticut; tip angle = 34°, NA = 0.22) and a 0.4 x 0.4 mm lead magnesium niobate-lead titanate (PMN-PT) ultrasound transducer (Dept. of Biomedical Engineering, University of Southern California; 45 MHz central frequency, 45% relative bandwidth) [22, 23]. The catheter was positioned by a motorized stage (MP 63-25-DC and DT 105, Steinmeyer GmbH & Co. KG, Albstadt, Germany). A pulse/delay generator (BNC model 575, Berkeley Nucleonics

Corporation, San Rafael, CA, USA), triggered by the Q-switch of the laser, provided synchronisation signals to the data acquisition card and arbitrary waveform generator (WW2571A, Tabor Electronics, Tel Hanan, Israel) for pulse echo imaging.

3.2.2 Lipid spectroscopy

To investigate the possibility of lipid detection and differentiation in the 1.7 μm range, the spectra of the lipids in plaque and peri-adventitial fat were measured. The spectra of lipids in plaques were measured with pure cholesterol, cholesterol oleate and cholesterol linoleate samples (Sigma Aldrich Co., C8667, C9253 and C0289, respectively), which are dominant lipids in human atherosclerotic plaques [16, 24]. The spectra of the lipids in peri-adventitial fat were measured directly using the human peri-vascular adipose tissue. We filled one lipid sample at a time in a custom-built TPX holder (TPX® Polymethylpentene) and positioned the holder in front of the ultrasound transducer to optimize the signal-to-noise ratio (SNR) of the PA signal.

Spectroscopic photoacoustic imaging (sPA) was performed in the spectral range from 1620 to 1780 nm with a step of 2 nm in clear water at room temperature. The laser energy for sPA imaging was about 0.35 mJ/pulse at the catheter tip. To improve the PA SNR, 32 A-lines were averaged at every wavelength. We acquired at least 500 PA spectral data sets per lipid sample. These spectra were used as a reference. We performed statistical analysis to investigate the spectral contrast between different lipid samples. Since the sPA data were acquired within a narrow spectral range (1620 to 1780 nm), the variations of the average laser pulse energy and the tissue scattering properties were negligible. Any differences in the PA signal were assumed to only arise due to the optical absorption contrast in this spectral range. All the lipid spectra were filtered using a Savitzky-Golay FIR smoothing filter and normalized to their respective maxima for display.

Typical spectra of the different lipid samples are shown in fig. 3.2(a). In the figure, the spectra of different lipid samples are relatively similar. The dominant differences of the spectra between lipids in plaque and in peri-adventitial tissue are shifts in the locations of the peaks, and these differences make it possible to differentiate between the lipids in plaques and in peri-adventitial tissue.

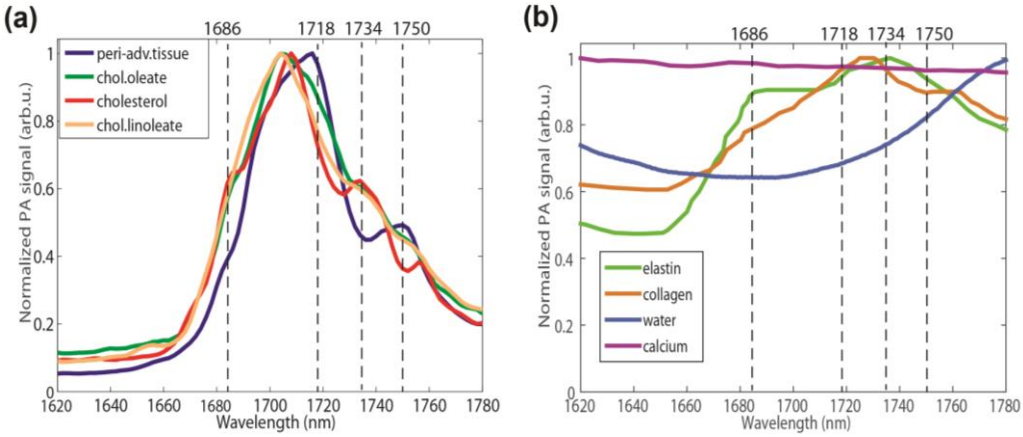

Figure 3.2. The spectra of different tissue types in 1.7μm spectral range. (a) The normalized PA spectra of different lipid samples. (b) The spectra of elastin, collagen, water, and calcium obtained from refs. [25-27, 29]. All spectra are normalized to their respective maxima.

3.2.3 Criteria for lipid detection and differentiation

Choosing optimal PA excitation wavelengths for specific plaque lipid detection is critical. In order to minimize time and power overhead, we aim to select two wavelengths only. The ideal pair of wavelengths is closely spaced (to avoid any fluence changes due to water absorption or tissue optics) and provides sufficient PA contrast for lipid detection and differentiation. In the 1.7 μm spectral range, lipids produce a usable PA signal between 1680 and 1750 nm, where lipid absorption exceeds that of water [25, 26].

To differentiate the plaque lipids and peri-adventitial fat, we plotted the difference between the cholesterol (representative of plaque lipid) and peri-adventitial fat normalized spectra in Fig. 3.3. The figure shows that there are four wavelengths exhibiting a large contrast, which are marked with red dots. Plaque lipid has a larger PA signal at 1686 nm and 1734 nm, while the peri-adventitial fat response dominates at 1718 nm and 1750 nm. A pair of wavelengths is selected based on the contrast of the two-wavelength relative difference in PA signal of the tissue types that may be expected to occur in the coronary artery wall: lipids, water, calcium and the connective tissues (elastin and collagen). Normalized PA spectra for these non-lipid tissues are shown in Fig. 3.2(b) [26-29]. The relative PA difference ΔPA is defined as follows:

$$\Delta\mathrm{PA} = \frac{PA_{\lambda_1} - PA_{\lambda_2}}{PA_{\lambda_1}}$$

where PA_{λ_1} and PA_{λ_2} are the PA amplitudes at the two wavelengths. Note that for noise immunity, lipids should generate PA signals with good SNR at the selected wavelengths. Of these four wavelengths, 1718 nm is close to the peak response of all lipids, and hence always generates a strong signal. We choose this wavelength as λ_1 to avoid the denominator in ΔPA becoming small and to decrease the sensitivity to noise. Adequate contrast and acceptable noise sensitivity can be achieved with λ_1 = 1718 nm and λ_2 = 1734 nm, which is the nearest usable wavelength.

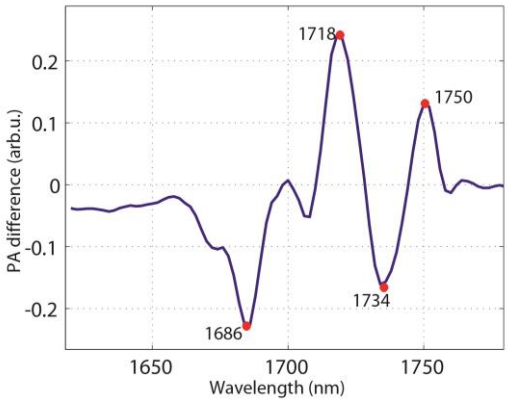

Figure 3.3. Difference in PA normalized spectra between cholesterol and peri-adventitial fat. Four wavelengths produce a large enough difference to be useful for distinguishing the two.

We computed ΔPA at 1718 and 1734 nm, for all spectra acquired on the different lipid samples and performed statistical analysis on the results, shown in Fig. 3.4. This representation shows how ΔPA can be used for tissue characterization. Water, calcium and connective tissues have $\Delta PA \leq 0$, while for lipids this quantity is always positive. Fatty acids have a larger relative difference than plaque lipids. We can discriminate between plaque lipids, peri-adventitial fat, and other tissue components by setting two thresholds: ΔPA > 0.1 for all lipids (red dashed line in Fig. 3.4) and $0.1 < \Delta PA < 0.35$ for plaque lipids. The former threshold accounts for an unknown experimental variability in the PA spectra of collagen, elastin, and calcium, which were based on literature data, as well as a potential underestimation of the variance in the ΔPA of plaque lipid related to composition differences. There is a small overlap of the relative differences between the plaque lipids and peri-adventitial fat. The upper threshold was defined as the minimum of the measured relative differences of peri-adventitial fat in our data set. In this way, most of the atherosclerotic plaques are detected while the other normal components of the artery wall (such as peri-adventitial fat) are excluded, minimizing the false-positive rate.

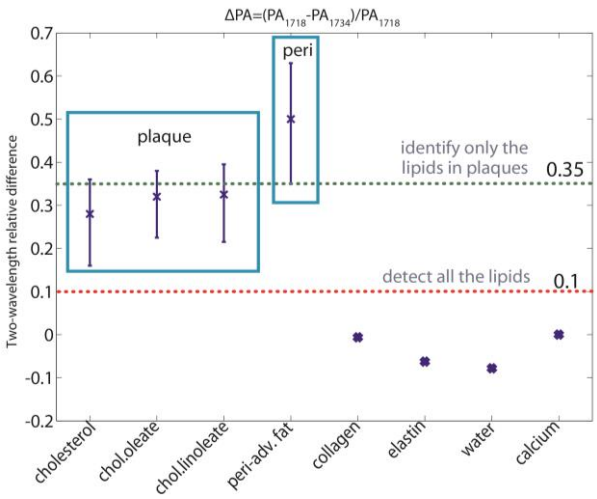

Figure 3.4. The relative difference between different tissue types at the wavelength of 1718 and 1734 nm plotted as average

3.2.4 Ex vivo experiments

3.2.4.1 Vessel mimicking phantom experiment

To test the presented method, we performed IVPA/IVUS imaging on a poly-vinyl-alcohol (PVA) vessel mimicking phantom (10% wt. PVA crystals in demineralized water, 3 freeze/thaw cycles of at least 2h). The phantom has a 3 mm diameter lumen with four cylindrical cavities 0.5 mm apart from the lumen. All the cylindrical cavities are 1.5 mm round by 5 mm deep. One cavity was filled with human peri-adventitial fat from a coronary artery specimen. The other three cavities were filled with pure cholesterol, cholesterol oleate and cholesterol linoleate samples (Sigma Aldrich Co., C8667, C9253 and C0289), respectively. A photo of the filled PVA vessel phantom is shown in Fig. 3.5(a).

The phantom was placed in clear water at room temperature. The catheter was positioned inside the lumen of the phantom to image all the lipids filled in the cavities. By rotating the catheter 360° in 1° steps, the full cross-sectional IVPA/US images of the phantom were acquired. At every rotation angle, the laser was tuned between 1718 and 1734 nm to ensure the co-registration of the IVPA data at both wavelengths. US images were 8 times averaged; no averaging was applied for PA images.

3.2.4.2 Human coronary artery measurement

We collected human coronary arteries at autopsy from the Department of Pathology of Erasmus Medical Center (MC), after obtaining consent from the relatives. The research protocol was sanctioned by the Medical Ethics Committee of Erasmus MC (MEC-2007-081). The coronary arteries were frozen within 2h at -80°, then thawed and measured within 2 months. In the measurement, we fixed the artery on top of a custom built TPX tissue holder with an array of 200 µm thick metal wires glued every 1.5 mm at the bottom. The metal wires were clearly visible in the IVPA/IVUS images and used as the marker to register the imaging position. The tissue holder was placed inside a water tank filled with saline solution at room temperature. Spatially co-registered two-wavelength (1718 and 1734 nm) IVPA and IVUS images were obtained by rotating the catheter inside the lumen of the artery in 1° steps and repeating PA and US acquisitions at every step. IVUS images were 10 times averaged; no averaging was applied for PA images.

After the IVPA/IVUS imaging, we cut the artery at the two wires adjacent to the imaging plane, embedded in optimal cutting temperature (OCT) compound (Tissue-Tek®, Sakura Finetek Europe B.V.), and then were frozen on dry ice, and stored at -80°C until further processing. For histopathology, we cut into the tissue block until the imaged location was reached. A series of 10 µm thick sections were thaw mounted on slides and stained with Oil Red O (ORO) to identify lipids in the artery (lipids are stained red in ORO staining).

3. 2.4.3 Data processing

All the stored US and PA data were digitally band pass filtered (10 to 70 MHz, 100th order zero-phase forward and reverse finite impulse response (FIR) filter), Tukey windowed, envelope filtered, artefacts removed and converted for display as discussed in our previous work [13]. Specifically, absorption of laser pulses in the catheter tip generates an artefact in

the PA data that is proportional to the laser pulse energy. We used the magnitude of this signal to correct for variations in the laser energy between individual pulses and between the different wavelengths. The artefact was removed from the data by an adaptive filter that detects and suppresses highly correlated features across A-lines, spanning angles of more than 20 degrees. A binary denoising mask was defined to include all pixels where PA amplitude at 1718 nm is higher than the background noise threshold, and reject data elsewhere. The background noise threshold is calculated as the maximum envelope signal in a region of the image beyond the imaged object. This denoising mask was then applied to the pixel-to-pixel calculated relative difference between the PA signals at 1718 and 1734 nm as described in section 2.2. Subsequently, we obtained the lipid differentiation map by implementing the first cutoff threshold of 0.1 to detect all the lipids and the second cutoff threshold of 0.35 to identify only the lipid in plaques. The lipid differentiation map was then scan-converted to Cartesian coordinates, color coded (red for lipids in peri-adventitial tissue and yellow for lipids in plaques) and overlaid on the co-registered US images for display.

To evaluate the presented method, we calculated the classification accuracy for plaque lipid detection. True positives are plaque lipid pixels inside the external elastic lamina (EEL), which separates the media and adventitia layer of the artery wall; true negatives are adipose-type lipids pixels outside the EEL. Plaque lipid pixels outside the EEL are classified as false positives; as explained above, minimization of the number of false positives is important for clinical application. False negatives are not detected, as plaques often comprise a fraction of non-cholesterol lipids. We report performance as the number of plaque lipids inside and outside the EEL. The former is expected to be greater than zero but less than 100% because of the presence of fatty-acid-like lipid species; the latter should be as small as possible as no cholesterol-like molecules occur in adipose lipids.

3.3 Results

3.3.1 Lipid imaging in a vessel mimicking phantom

Fig. 3.5 (b) shows the lipid detection and differentiation results of the PVA vessel mimicking phantom. In the figure, all lipid samples inside the four holes were clearly visible and the lipid differentiation results agreed with the phantom arrangement very well. The attenuation by the lipid samples (and water, to a degree) in the 1.7 μm spectral range limits the PA imaging depth to about 2.5 mm. We calculated the differentiation results and got 97.3% true positive and no false positive lipid differentiation in the PVA phantom.

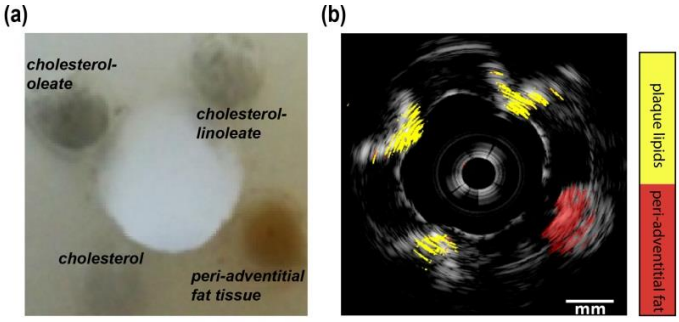

Figure 3.5. Lipid detection and differentiation result of the PVA vessel mimicking phantom. (a) The photo of the PVA vessel phantom with filled different lipid samples. (b) Lipid differentiation map fused with US image of the PVA vessel phantom. The lipids in plaques are in yellow and lipids in peri-adventitial tissue are in red. The dynamic range of the US image is 40 dB.

3.3.2 Lipid imaging in a human coronary artery specimen

Lipid content of a human atherosclerotic plaque was evaluated by IVPA in a left anterior descending artery (male donor, 80 years old). Histology shows the presence of a large eccentric plaque with abundant lipids both superficially and deeply located in the plaque (Fig. 3.6(a)). In Fig. 3.6(b), the EEL of the artery, separating the media and adventitia, is clearly visible in the IVUS image, and we marked the EEL by a light blue contour. The IVPA data confirm the lipid deposition that was identified in the histology, located from 12 o'clock to 9 o'clock inside the artery wall containing lots of extracellular lipid droplets. However, the lipids located from 9 o'clock to 12 o'clock inside the artery wall remain undetected. These are mostly intracellular lipids, to which IVPA appears to be less sensitive [13]. The IVPA signal strength also varies the distance from the catheter depending on the probe geometry [22]. Inside this lipid-rich plaque, 76% of the lipids are identified as cholesterol-derived plaque lipids (in yellow). The lipid signal observed from 7 o'clock to 12 o'clock outside the artery wall comes from adipose tissue, and 84% of this is indeed identified as peri-adventitial adipose tissue (in red).

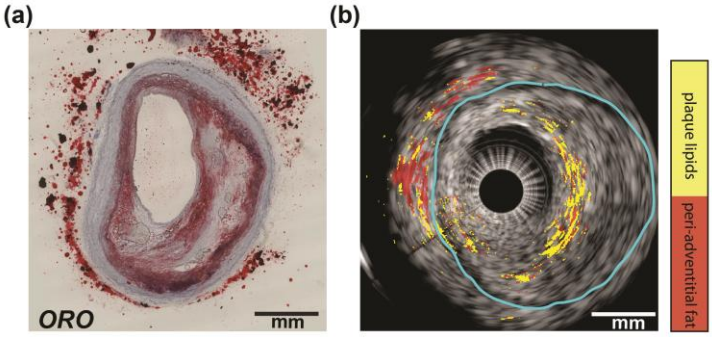

Figure 3.6. Ex vivo lipid differentiation result of an atherosclerotic human coronary artery (LAD, male, 80 years old). (a) Histology: Oil Red O staining of the IVPA/IVUS imaging cross section (lipids are in red). (b) Lipid differentiation map overlaid on the co-registered US image of the coronary artery. The lipids in plaques are in yellow and lipids in peri-adventitial tissue are in red. The dynamic range of the US image is 45 dB.

Ex vivo lipid differentiation in another human coronary artery is shown in Fig. 3.7. The histology of the artery (Fig. 3.7(a)) reveals absence of atherosclerosis in this cross section. All lipids in the ORO stain are located outside the artery wall. In the lipid differentiation map, all the detected lipids are shown outside the EEL (indicated by the light blue contour). We calculated that 95.5% of the detected lipids are identified as peri-adventitial adipose tissue.

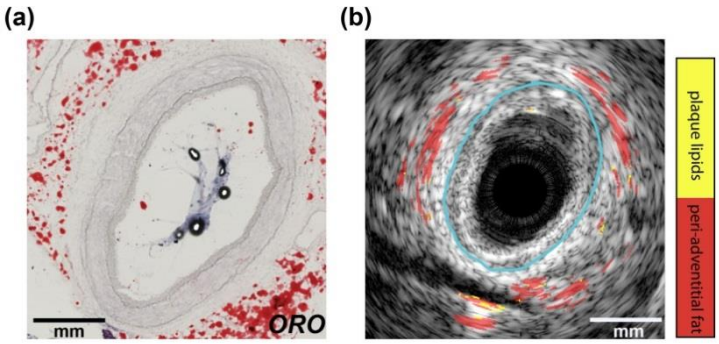

Figure 3.7. Ex vivo lipid identification result of a human coronary artery (LAD, male, 54 years old). (a) Histology: Oil Red O staining of the IVPA/IVUS imaging cross section (lipids are in red). (b) Lipid differentiation map overlaid on the co-registered US image of the coronary artery. The lipids in plaques are in yellow and lipids in peri-adventitial tissue are in red. The dynamic range of the US image is 45 dB.

All ex-vivo lipid identification results are presented in Table 3.1. The table lists the true (plaque lipids detected inside the artery wall) and false (plaque lipids detected outside the artery wall) plaque lipids detection results. Phantom case in shown in Fig.3.5 and human artery case 1 and 2 are described above in fig.3.6 and fig.3.7. In artery case 3, we achieved 68% true positive and 18% false positive plaque lipid detection. In artery case 4, a large LRP was detected, and no peri-adventitial adipose tissue was visible due to insufficient laser light penetrating at its depth. In this case, we attained 67% true positive plaque lipid detection. Artery case 5 presents another clean artery and we achieved 14% false positive plaque lipid detection.

Table 3.1. Ex-vivo plaque lipid detection results
(Phantom case in Fig.3.5; artery case 1 in Fig. 3.6; artery case 2 in Fig. 3.7)

	Plaque lipids inside EEL (%)	Plaque lipids outside EEL (%)
Phantom	97.3	0
Artery case 1	76	16
Artery case 2	--	4.5
Artery case 3	68	18
Artery case 4	67	--
Artery case 5	--	14

3.4 Discussion and conclusion

Our results have demonstrated that it is possible to detect and differentiate between the lipid in plaques and in peri-adventitial adipose tissue using relative difference of the PA signal at only two wavelengths, namely 1718 and 1734 nm. Small differences in the absorption spectrum of the different lipids in and around the artery make it possible to specifically identify plaque lipids by IVPA. To the best of our knowledge, the method presented here uses the lowest

number of wavelengths for detecting and differentiating between lipids in plaques and in peri-adventitial adipose tissue.

In a series of human coronary arteries ex vivo, we identify about 70% of lipids in plaques, and 15% in the peri-adventitia tissue as cholesterol-like lipids. The latter number represents actual false positives. The former score may be affected by the variability of plaque lipid composition: Plaques also contain non-sterol lipids (e.g. triglycerides and phosphatidylcholines). These molecules do not contain a multiply connected carbon backbone, but rather consist of largely saturated hydrocarbon chains, which are likely to have a fatty-acid-like absorption spectrum. In a clinical application targeting coronary artery disease, specificity is preferable over sensitivity: it is more important to be sure that a detected LRP is actually a significant plaque, than to detect every small lipid deposit which is likely clinically irrelevant. We chose the upper threshold, separating plaque lipids from fatty acid, to prevent false positives as much as possible.

The optimal wavelength selection needs to be confirmed by a more extensive ex vivo spectroscopy study, deriving more robust cut-offs from the spectral data of human coronary artery plaques instead of pure lipid samples. Such a study requires spectroscopic IVPA imaging of full cross-sections, and at present our laser system is too slow to allow us to perform this measurement; faster IVPA systems are on the horizon [30-32]. For technical reasons, the OPO system we used in this study has a tuning accuracy in this wavelength range of a few nm, which means that the reported wavelengths are indeterminate within that band. The general principle of the method reported here remains valid, but the wavelength calibration is somewhat laser-dependent.

One limitation of our method is that the identification results are sensitive to noise, as it relies on the precise determination of the ratio between two relatively weak signals. At 1734 nm, lipids generated just moderate PA signals, making PA images at this wavelength vulnerable to noise. Further noise reduction and increased transducer sensitivity will improve the accuracy and reliability of the lipid identification. Another limitation is that the PA imaging depth at 1.7 μm is lower than that at 1.2 μm [21]. Nevertheless, the imaging depth we achieved in our ex vivo measurements of human coronary arteries at 1.7 μm was about 3 mm, which is sufficient to image human coronary arteries [21, 33]. The large absorption coefficient of superficial lipid did suppress the contrast of the deeper layer in the plaque shown in Fig. 6. As mentioned before, better detection sensitivity may help, although the strong superficial absorption at 1718 nm may actually “color” the light, causing a violation of the assumption that light at both wavelengths is equally attenuated, reducing ΔPA to below the threshold set for lipids, leading to underestimation of the plaque volume. This is a fundamental limitation in PA imaging that also affects oxygen saturation measurements in other applications [34, 35]. Deriving a fluence correction and smoothing the lipid differentiation map may help to mediate this light coloring effect.

Our method will enable a rapid data acquisition, which is essential for clinical application of IVPA. In current clinical practice, LRP may be detected with high specificity by near-infrared reflection spectroscopy (NIRS) [6, 7, 36, 37]. A limitation of that technology in its commercial

form is its inability to determine the depth of lipid deposits in the vessel wall. IVPA amends that shortcoming by not just detecting, but imaging lipids. NIRS has positively demonstrated the clinical value of an overall assessment of the presence of LRP in the whole artery, which is done in a display that summarizes the entire pullback, obviating the necessity to inspect the data set frame by frame. Earlier implementations of lipid detection by IVPA [5, 11, 15, 38] were unable to discriminate between plaque and adipose tissue. Peri-adventitial fat is detected in almost all IVPA images, and specific plaque lipid imaging is needed to present a clinician with a rapid assessment of the presence of LRP and the cap thickness overlaying the lipid core, without tedious examination of every individual cross sectional image in the pullback or error-prone automated IVUS image processing.

In conclusion, we have presented here a technique to specifically image lipids in atherosclerotic plaques. It relies on subtle spectroscopic contrast between different lipid types in and around the artery, which we probe by two-wavelength IVPA. Two thresholds applied to this differential measurement make it possible to detect all lipid and separate plaque-specific lipids from the more common fatty-acid-like lipids. This technique enables rapid identification of thin-cap lipid-rich atherosclerotic plaque in coronary arteries. Its speed and moderate pulse energy open up an avenue of translating IVPA imaging to clinical application.

References

1. Falk, E., P.K. Shah, and V. Fuster, *Coronary Plaque Disruption.* Circulation, 1995. **92**(3): p. 657-671.
2. Virmani, R., et al., *Pathology of the vulnerable plaque.* J Am Coll Cardiol, 2006. **47**(8 Suppl): p. C13-8.
3. Schaar, J.A., et al., *Terminology for high-risk and vulnerable coronary artery plaques.* European Heart Journal, 2004. **25**(12): p. 1077-1082.
4. Allen, T.J., et al. *Photoacoustic imaging of lipid rich plaques in human aorta*. in *Photons Plus Ultrasound: Imaging and Sensing 2010*. 2010. San Francisco, California, USA: SPIE.
5. Wang, B., et al., *Detection of lipid in atherosclerotic vessels using ultrasound-guided spectroscopic intravascular photoacoustic imaging.* Optics Express, 2010. **18**(5): p. 4889-4897.
6. Waxman, S., et al., *In Vivo Validation of a Catheter-Based Near-Infrared Spectroscopy System for Detection of Lipid Core Coronary Plaques: Initial Results of the SPECTACL Study.* J Am Coll Cardiol Img, 2009. **2**(7): p. 858-868.
7. Gardner, C.M., et al., *Detection of lipid core coronary plaques in autopsy specimens with a novel catheter-based near-infrared spectroscopy system.* JACC Cardiovasc Imaging, 2008. **1**(5): p. 638-48.
8. Sethuraman, S., et al., *Intravascular photoacoustic imaging using an IVUS imaging catheter.* Ieee Transactions on Ultrasonics Ferroelectrics and Frequency Control, 2007. **54**(5): p. 978-986.
9. Sethuraman, S., et al., *Ex vivo Characterization of Atherosclerosis using Intravascular Photoacoustic Imaging.* Optics Express, 2007. **15**(25): p. 16657-16666.
10. Jansen, K., et al., *Intravascular photoacoustic imaging of human coronary atherosclerosis.* Opt. Lett., 2011. **36**(5): p. 597-599.

11. Wang, P., et al., *Bond-selective imaging of deep tissue through the optical window between 1600 and 1850 nm.* Journal of biophotonics, 2012. **5**(1): p. 25-32.
12. Wang, B., et al., *Intravascular photoacoustic imaging of lipid in atherosclerotic plaques in the presence of luminal blood.* Opt Lett, 2012. **37**(7): p. 1244-6.
13. Jansen, K., et al., *Lipid detection in atherosclerotic human coronaries by spectroscopic intravascular photoacoustic imaging.* Optics Express, 2013. **21**(18): p. 21472-21484.
14. Allen, T.J., et al., *Spectroscopic photoacoustic imaging of lipid-rich plaques in the human aorta in the 740 to 1400 nm wavelength range.* Journal of Biomedical Optics, 2012. **17**(6): p. 061209-10.
15. Wang, B., et al., *In vivo Intravascular Ultrasound-guided Photoacoustic Imaging of Lipid in Plaques Using an Animal Model of Atherosclerosis.* Ultrasound in medicine & biology, 2012.
16. Lundberg, B., *Chemical-Composition and Physical State of Lipid Deposits in Atherosclerosis.* Atherosclerosis, 1985. **56**(1): p. 93-110.
17. Stegemann, C., et al., *Comparative Lipidomics Profiling of Human Atherosclerotic Plaques / Clinical Perspective.* Circulation: Cardiovascular Genetics, 2011. **4**(3): p. 232-242.
18. Tsai, C.L., J.C. Chen, and W.J. Wang, *Near-infrared absorption property of biological soft tissue constituents.* J Med Biol Eng, 2001. **21**(1): p. 7-14.
19. Spector, W.S., *Handbook of Biological Data*. 1956: W.B. Saunders and Company.
20. Takaoka, M., et al., *Periadventitial adipose tissue plays a critical role in vascular remodeling.* Circulation research, 2009. **105**(9): p. 906-911.
21. Jansen, K., et al., *Photoacoustic imaging of human coronary atherosclerosis in two spectral bands.* Photoacoustics, 2014. **2**(1): p. 12-20.
22. Wu, M., et al., *Impact of device geometry on the imaging characteristics of an intravascular photoacoustic catheter.* Applied Optics, 2014. **53**(34): p. 8131-8139.
23. Zhou, Q., et al., *PMN-PT single crystal, high-frequency ultrasonic needle transducers for pulsed-wave Doppler application.* IEEE Trans Ultrason Ferroelectr Freq Control, 2007. **54**(3): p. 668-75.
24. Stegemann, C., et al., *Comparative lipidomics profiling of human atherosclerotic plaques.* Circ Cardiovasc Genet, 2011. **4**(3): p. 232-42.
25. Anderson, R.R., et al., *Selective photothermolysis of lipid-rich tissues: A free electron laser study.* Lasers in Surgery and Medicine, 2006. **38**(10): p. 913-919.
26. Caplan, J.D., et al., *Near-infrared spectroscopy for the detection of vulnerable coronary artery plaques.* J Am Coll Cardiol, 2006. **47**(8 Suppl): p. C92-6.
27. Nilsson, A.M.K., et al., *Near infrared diffuse reflection and laser-induced fluorescence spectroscopy for myocardial tissue characterisation.* Spectrochimica Acta Part A: Molecular and Biomolecular Spectroscopy, 1997. **53**(11): p. 1901-1912.
28. Wieliczka, D.M., S. Weng, and M.R. Querry, *Wedge shaped cell for highly absorbent liquids: infrared optical constants of water.* Applied Optics, 1989. **28**(9): p. 1714-1719.
29. Fleming, C.P., et al., *Depth resolved detection of lipid using spectroscopic optical coherence tomography.* Biomedical Optics Express, 2013. **4**(8): p. 1269-1284.
30. VanderLaan, D., et al. *System and integrated catheter for real-time intravascular ultrasound and photoacoustic imaging*. in *Ultrasonics Symposium (IUS), 2014 IEEE International*. 2014.
31. Li, Y., et al., *High-speed intravascular spectroscopic photoacoustic imaging at 1000 A-lines per second with a 0.9-mm diameter catheter.* Journal of Biomedical Optics, 2015. **20**(6): p. 065006-065006.

32. Wang, P., et al., *High-speed Intravascular Photoacoustic Imaging of Lipid-laden Atherosclerotic Plaque Enabled by a 2-kHz Barium Nitrite Raman Laser.* Sci. Rep., 2014. **4**.
33. Wang, P., et al., *High-speed Intravascular Photoacoustic Imaging of Lipid-laden Atherosclerotic Plaque Enabled by a 2-kHz Barium Nitrite Raman Laser.* Scientific reports, 2014. **4**.
34. Laufer, J., et al., *In vitro measurements of absolute blood oxygen saturation using pulsed near-infrared photoacoustic spectroscopy: accuracy and resolution.* Physics in Medicine and Biology, 2005. **50**(18): p. 4409.
35. Sivaramakrishnan, M., et al., *Limitations of quantitative photoacoustic measurements of blood oxygenation in small vessels.* Physics in Medicine and Biology, 2007. **52**(5): p. 1349.
36. Madder, R.D., et al., *Detection by Near-Infrared Spectroscopy of Large Lipid Core Plaques at Culprit Sites in Patients With Acute ST-Segment Elevation Myocardial Infarction.* JACC: Cardiovascular Interventions, 2013. **6**(8): p. 838-846.
37. Madder, R.D., et al., *Composition of Target Lesions by Near-Infrared Spectroscopy in Patients With Acute Coronary Syndrome Versus Stable Angina.* Circulation-Cardiovascular Interventions, 2012. **5**(1): p. 55-61.
38. Wang, H.W., et al., *Label-free bond-selective imaging by listening to vibrationally excited molecules.* Phys. Rev. Lett., 2011. **106**(23): p. 238106.

Chapter 4. Frequency analysis of the photoacoustic signal generated by coronary atherosclerotic plaque

Daeichin V, **Wu M**, de Jong N, et al. Frequency analysis of the photoacoustic signal generated by coronary atherosclerotic plaque. *Ultrasound Med Bio* 2016;42:2017–25.

Abstract

The identification of unstable atherosclerotic plaques in the coronary arteries is emerging as an important tool for guiding percutaneous coronary interventions, and may enable preventive treatment of such plaques in the future. Assessment of plaque stability requires imaging of both structure and composition. Spectroscopic photoacoustic (sPA) imaging can visualize atherosclerotic plaque composition on the basis of the optical absorption contrast. It is an established fact that the frequency content of the photoacoustic (PA) signal is correlated with the structural tissue properties. As PA signals can be weak, it is important to match the transducer bandwidth to the signal frequency content for in vivo imaging. In this ex vivo study on human coronary arteries, we combined sPA imaging and analysis of frequency content of the PA signals. Utilizing a broadband transducer (-3 dB one-way bandwidth of 10-35 MHz) and a 1 mm needle hydrophone (calibrated for 1-20 MHz), we covered a large frequency range from 1 MHz to 35 MHz for receiving the PA signals. sPA imaging was performed at wavelengths ranging from 1125 to 1275 nm with a step of 2 nm, allowing discrimination between plaque lipids and adventitial tissue. Guided by sPA imaging, the frequency content of the PA signals from the plaque lipids was quantified. Our data shows that more than 80% of the PA energy of the coronary plaque lipids lies in the frequency band below 8 MHz. This frequency information can guide the choice of the transducer element used for PA catheter fabrication.

4 .1 Introduction

A major cause of death worldwide is cardiovascular disease [1]. A substantial proportion of cardiac deaths are due to acute coronary syndromes. The majority of these fatal acute coronary syndromes are caused by ruptures of vulnerable atherosclerotic plaques and thrombosis [2-4]. The identification of unstable atherosclerotic plaques in the coronary artery is emerging as an important tool for guiding percutaneous coronary interventions. The structure and composition of the plaque are significant determinants of its stability [5]. Imaging modalities has provided a greater understanding of factors involved in the atherosclerosis disease process and has improved therapeutic interventions [6]. Particularly, intravascular imaging approaches can characterize the burden, composition and functionality of atherosclerotic plaque, neointimal hyperplasia and allograft vasculopathy that develop within coronary arteries [6].

Currently available intravascular imaging modalities have limitations in that respect: Intravascular ultrasound (IVUS) imaging is unable to distinguish plaque constituents other than calcium [7, 8]. Intravascular optical coherence tomography (OCT) has better soft tissue contrast, but its penetration depth is limited to 1-3 mm, and it requires flushing blood from the lumen of the vessel [9], a limitation that also applies to angioscopy. The intravascular chemical sensing techniques near infrared spectroscopy, Raman spectroscopy and intravascular fluorescence imaging cannot provide depth-resolved information [10, 11].

Intravascular photoacoustic (IVPA) imaging, and particularly spectroscopic IVPA (sIVPA) imaging, aims to fill this gap by imaging plaque components in a vessel wall with reasonably large imaging depth [12-15]. This imaging technique, which applies pulsed light excitation, benefits from the optical absorption properties of tissue composition as contrast. Typically, photoacoustic (PA) imaging utilizes the signal envelope of the PA signal to reconstruct macroscopic optical absorbers in an image [16]. Theoretical solutions of the wave equation for simple geometries predict that the PA pressure amplitude is proportional to the radius of the absorber squared whereas the main frequency of the PA signal is inversely related to the size of the absorber [17]: larger sources will emit PA pressure waves with higher amplitude and lower frequencies compared to smaller ones. As PA signals can be weak for *in vivo* imaging applications, it is important to match the transducer bandwidth to the major frequency contents of the PA signal. The frequency content of PA signals has recently been investigated to estimate the microscopic properties of absorbers in phantoms [18, 19] and in more complex biological tissues [20-26]. The frequency content of plaque lipid PA signal has not been investigated to date, and may be distinct from e.g. the adipose tissues surrounding the vessel. While this peri-adventitial fat has a homogeneous structure, there is variability in size, shape, and concentration of the lipid deposits, acting as PA sources, in plaque. This contrast in spatial structure affects the emitted acoustic frequencies. The small device size and stringent optical power limits of endoscopic applications mean that the signal-to-noise ratio (SNR) cannot be arbitrarily increased by larger sensor surface or excitation power, so optimization of the transducer sensitivity is a key step towards a reliable, safe, and usable IVPA technology.

Generally, to obtain co-registered IVUS and IVPA images, transducers with central frequency of 30-85 MHz have been used, which guarantees decent IVUS images. However, in absence of any data on the typical frequencies generated by PA imaging in lipid-rich atherosclerosis, it

is unknown whether the frequency range of >30 MHz is a suitable choice for plaque lipid detection. To investigate this question, we perform both a simulation and a statistical analysis of the frequency content in the range of 1-35 MHz of PA signal obtained from human coronary artery plaques *ex vivo*.

4 .2 Methods

4.2.1 Experiment Setup

The overall schematic of the imaging setup is illustrated in figure 1a. A tuneable laser (Vibrant B/355-II, OPOTEK, Santa Clara, CA, USA) served as an optical excitation source for PA imaging (pulse width: 5 ns, repetition rate: 10 Hz, and energy per pulse at 1200 nm wavelength: 2 mJ). A tapered multimode optical fibre (Oxford Electronics, Four Marks, UK; input diameter: 1 mm, output diameter: 360 µm) coupled the laser light to a custom built forward looking optical probe for light delivery (fiber core diameter: 400 um). A needle hydrophone (Hydrophone 1875, Precision acoustics Ltd, Dorset, UK) calibrated from 1 MHz to 20 MHz and a polyvinylidene difluoride (PVDF) focused transducer calibrated from 10 MHz to 35MHz received the PA signals. Combining these two broadband receivers, a large frequency range (1-35 MHz) was covered. We will refer to the hydrophone as the low frequency (LF) probe and the PVDF transducer as the high frequency (HF) probe in the rest of this manuscript. A holder with a window size of 5 x 5 mm held the artery samples. The received signal level was optimized by the relative positioning of the tissue sample and the ultrasound receivers: the tissue sample was positioned in the focus of the HF probe, and approximately 5 mm from the LF probe respectively. The sample holder was connected to a motorized translation stage (MP 63-25-DC, Steinmeyer GmbH & Co. KG, Albstadt, Germany) to scan the samples. The PA signals were amplified by a 43 dB amplifier (AU1263, Miteq, Hauppauge, NY, USA) and were digitized at sample frequency of 350 MHz by 12-bit data acquisition card (Acqiris DP310, Agilent, Santa Clara, CA, USA).

4.2.2 Phantom measurement

The sPA imaging on a phantom was performed to study the PA radio frequency spectra of intraplaque lipids at different frequency bands. A Polyvinyl alcohol (PVA) phantom (10% wt. PVA crystals in demineralized water, 3 freeze/thaw cycles of at least 2h) was prepared with a lumen size of 3 mm and a 1.5 mm round by 5 mm deep cylindrical cavity at 500 µm from the lumen. The cavity was filled with cholesterol, cholesterol oleate , cholesterol linoleate (Sigma Aldrich Co., C8667, C9253 and C0289, respectively) which are dominating the plaque lipid composition [27], and a piece of human coronary adipose tissue. The cavity was emptied and cleaned each time before placing a new sample. The sPA imaging was performed from 1125 to 1275 nm wavelengths with a 2 nm steps (in water at room temperature). The PA signals were 32 times averaged to improve the SNR. The reference sPA signals were acquired using a transducer with the central frequency of 40 MHz (referred as the very high frequency (VHF) probe in the following text) and bandwidth of 50% as in our previous study [28]. These data are referred to as reference data since the majority of publications in the field have used similarly high frequency IVUS transducers for IVPA applications.

4.2.3 Ex vivo measurement

Ten human coronary arteries were collected at autopsy from the Department of Pathology of Erasmus Medical Center (MC), after obtaining consent from the relatives, under a research protocol sanctioned by the Medical Ethics Committee of the Erasmus MC (MEC-2007-081). The coronary arteries were frozen within 24h post mortem at -80°, and thawed and measured several weeks later for imaging. Before the IVPA measurement, the arteries were imaged by OCT (C7XR system with Dragonfly catheters; St. Jude Medical, St. Paul MN, USA) to exclude any arteries without atherosclerotic plaques. In the end, seven human coronary arteries were selected for sPA imaging. The coronary arteries were cut open longitudinally, mounted on the holder and submerged in saline solution at room temperature with the lumen side facing the optical probe (Fig. 4.1(b)). In this configuration, the PA signals of the adipose tissue reach the acoustic probe first.

sPA imaging was performed at optical excitation wavelengths ranging from 1125 to 1275 nm with steps of 2 nm, allowing localization of the plaque region and discrimination between plaque lipids and peri-adventitial fat tissue [13, 27, 28]. At each optical wavelength, 32 PA signals were collected and averaged to improve the SNR. The sPA imaging was performed on at least 5 locations for each artery sample. Then histological analysis was performed on each sample where Oil Red O (ORO) staining was applied at the same cross section on the sample from which the PA signal was acquired to identify intraplaque lipids and peri-adventitial lipids (lipids are stained red in ORO staining) (Fig. 4.1(c)).

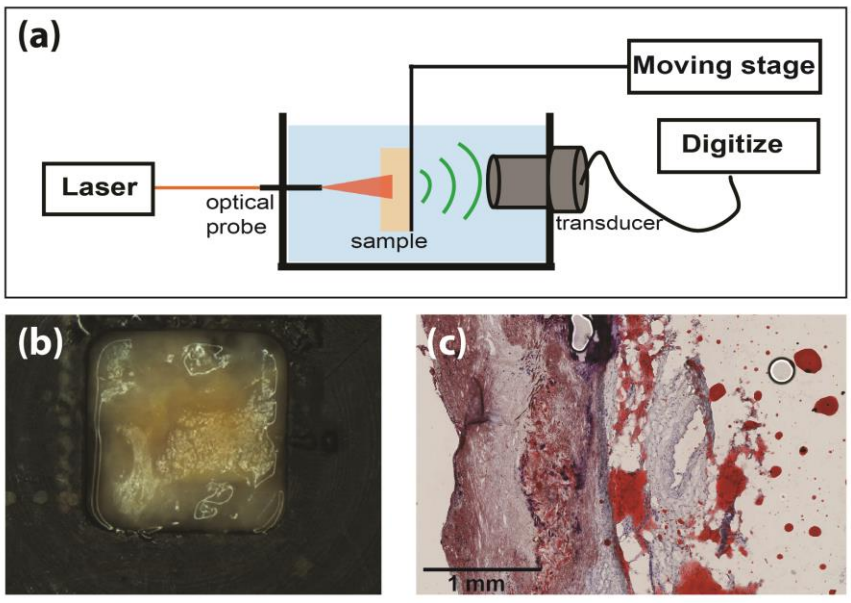

Figure 4.1. a) A schematic diagram of experimental setup for sPA imaging; b) Photo of an artery sample mounted on the holder; c) Image of a histology slice with Oil Red O (ORO) staining showing lipids in red. The artery samples were placed with the lumen side facing the optical probe.

4.2.4 Data processing

The data from the LF probe were filtered from 1 to 15 MHz (-3 dB bandwidth) and the data from the HF probe were filtered from 10 to 35 MHz (-3 dB one-way bandwidth), using a 100th order zero-phase forward and reverse finite impulse response (FIR) filter. The PA optical spectra were compared with the reference PA optical spectra of plaque lipids and human adipose tissue [28], to separate the PA signals by tissue type. The frequency analysis on the PA signals of lipid-rich tissues was performed at the optical wavelength where lipids most effectively absorb light (e.g. at 1205 nm).

The PA signals recorded by both LF and HF probes were stitched together by scaling the signal received by the HF probe. The scaling factor was calculated as the ratio of amplitudes of the PA signals received by the LF probe and the HF probe at the overlapping frequency of 13 MHz. Although the probes were calibrated using their transfer function, the stitching was done to rule out the effect of the different transducer surface areas. Then the PA signals of the intraplaque lipids were Fourier transformed to calculate the main frequency and the percentage of the accumulative PA power over the frequency range from 1 to 35 MHz.

Furthermore, the shapes of the PA optical spectra received by the LF and HF probes were quantified and compared to the reference PA optical spectra. Quantification is based on the location of the peak in the PA optical spectra and the full width of the optical spectra at 50% of the peak amplitude. The latter parameter is referred to as the full width at half maximum (FWHM) in the rest of this manuscript.

4.2.5 Simulation

In the simulation, we used the MATLAB k-Wave toolbox [29] to simulate the time-domain PA signals of the initial pressure source obtained from intraplaque lipids in histology. The purpose of this simulation study was to further investigate whether the intraplaque lipid structures in our experiments would produce PA signals with main frequencies similar to what was obtained in the ex vivo experiments. The initial pressure source was obtained from the ORO staining of a human coronary plaque with all lipids stained in red (Figure 1c). First, we segmented the lipids using a custom-made filtering method based on the RGB colors of the image (segmenting red structures of the image). Then the segmented lipid structures were used as an initial pressure input source for k-Wave toolbox to simulate the PA signals. Then, the FFT was applied to the simulated PA signal to calculate the frequency response. The percentage of the cumulative PA power was calculated and compared with the experimental data.

4 .3 Results

4.3.1 Phantom measurement

The PA optical spectra of lipids received by the LF probe are compared with the reference optical spectra in fig. 4.2. The spectra received by the LF are almost identical with the reference spectra for all the lipid samples. The PA optical spectra from plaque lipids have an absorption

peak at around 1190 nm and the spectra from adipose tissue have an absorption peak at 1205 nm regardless of the frequency band in which they are captured.

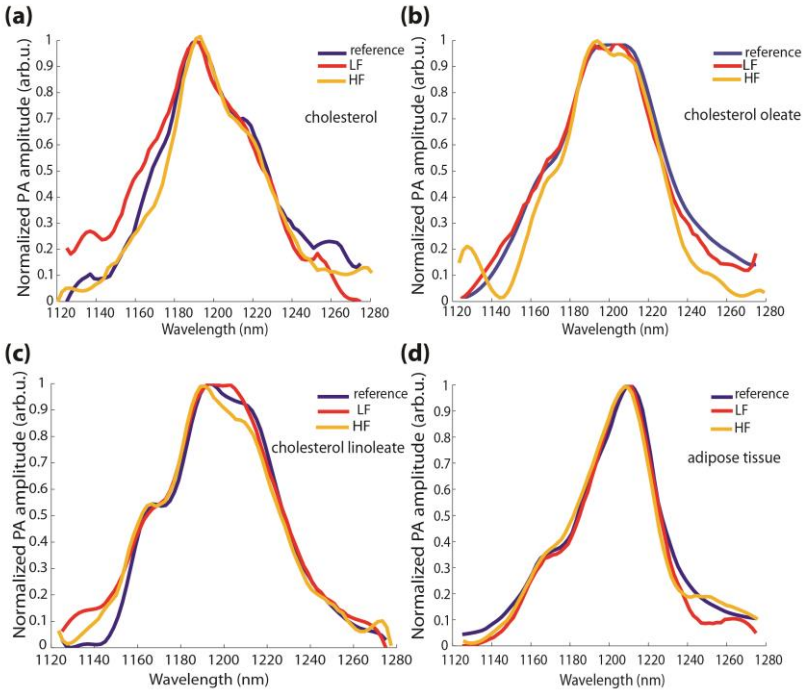

Figure 4.2. Comparison of photoacoustic (PA) spectra of the cholesterol (a), cholesterol oleate (b), cholesterol linoleate (c) and human coronary adipose tissue (d) received with the low frequency (LF) probe (red curves) and the reference spectra (blue curves).

4.3.2 Ex vivo measurement and simulation

An example of the ex vivo sPA image of a coronary atherosclerotic plaque is depicted in fig. 4.3. The sPA depth profiles acquired with LF and HF probes after laser power correction are shown in fig. 4.3 (a, c). The corresponding detailed PA optical spectra at the locations indicating by the dots in fig. 4.3 (a) and (c) are presented in fig. 4.3 (b) and (d)

Comparing the PA optical spectra with the reference spectra [28] (dashed lines in the fig. 4.3 (b) and (d)), we can separate the PA signal generated from the intraplaque lipids for further frequency analyses. The sPA signals correspond to the plaque optical spectra of the same tissue sample at depths from 8.8 mm to 9.3 mm with LF probe and 12.2 mm to 12.6 mm with HF probe in figure 3. The frequency content of the plaque PA signal and the cumulative PA power as a function of frequency are plotted and compared to the simulation results in figure 4. The overal powers of the PA signal in the examined frequency band are almost identical in both simulation and experiment (fig. 4.4 (b)). In both situations, we see that 80% of the total PA power lies below 5 MHz.

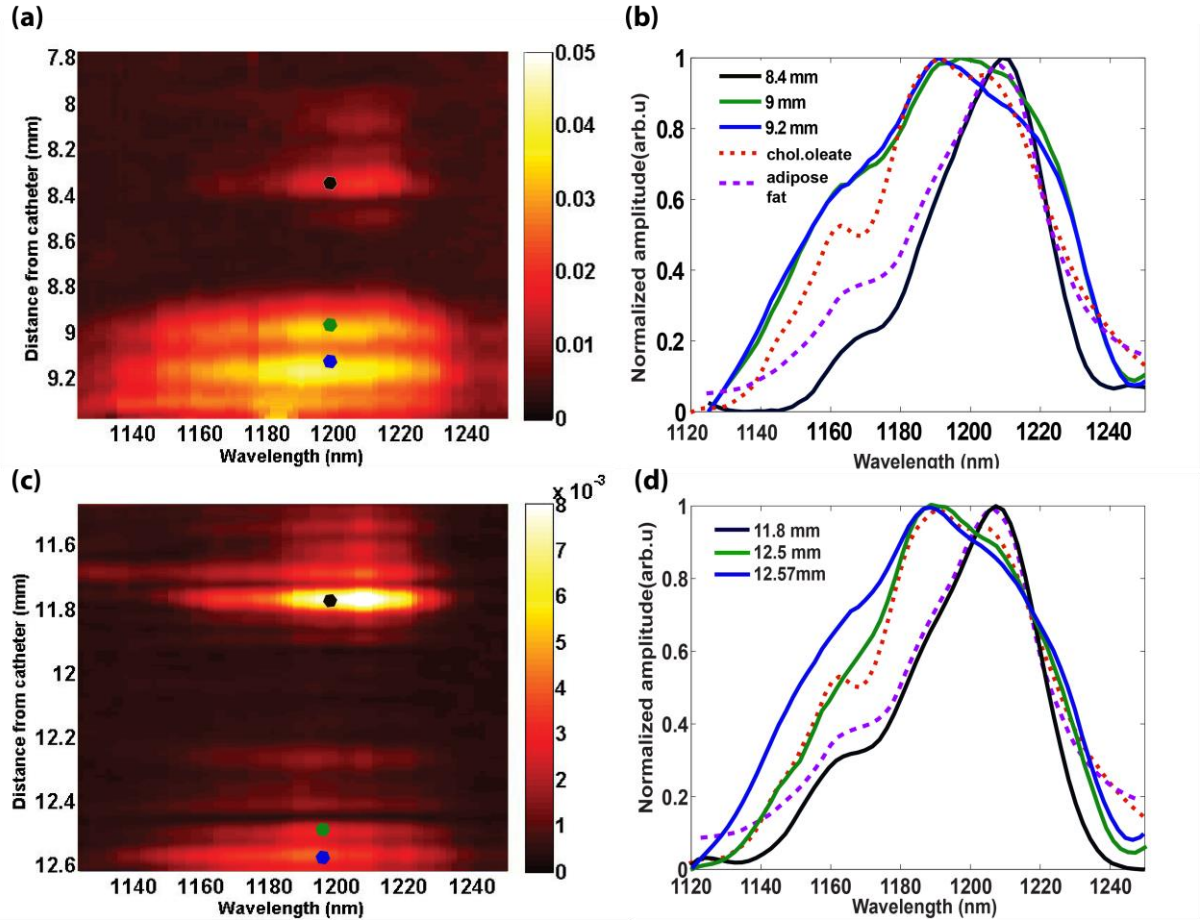

Figure 4.3. Spectroscopic photoacoustic (sPA) images of a human coronary plaque. The sPA depth profiles acquired with the low frequency (LF) probe (a) and the high frequency (HF) probe (c); corresponding PA spectra at the locations indicated with the dots in (a) and (c) acquired with the LF probe (b) and the HF probe (d). Dashed pink lines represent the reference plaque spectra and the dashed orange lines represent the adipose tissue spectra.

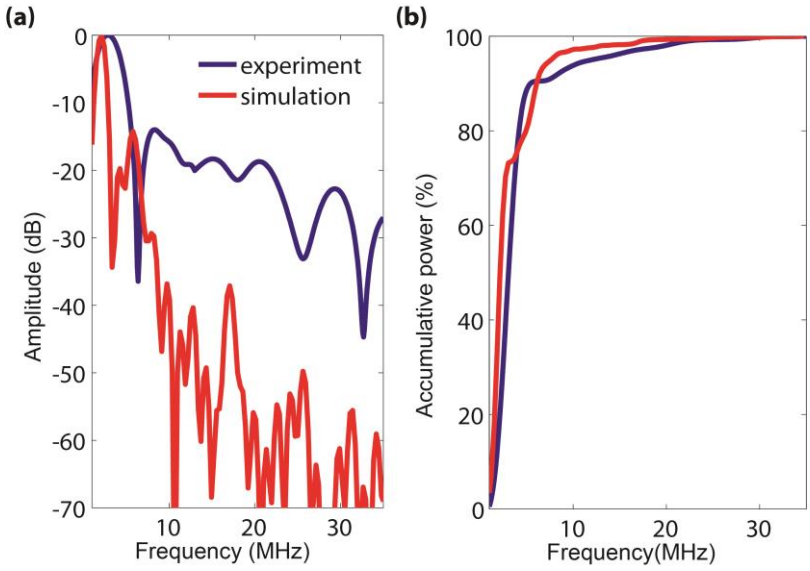

Figure 4.4. Experimental and computational frequency analysis of intraplaque lipids: a) Amplitude of the photoacoustic (PA) signal as a function of acoustic frequency; b) Percentage of the cumulative power over the frequency range of 1 MHz to 35 MHz.

Two thresholds were chosen to characterize the PA radio frequency power spectra of the plaque in the frequency range of 1 to 35 MHz, which is 60% and 80% of the total PA power. The same frequency analysis and thresholds were applied to all the PA signals of the artery samples (n=36). The statistical results are shown in a boxplot in fig. 4.5. With the threshold of 60% power, the PA signal falls in the frequency range below 7 MHz for all the samples and below 4 MHz for 75% of the samples. Increasing the threshold to 80% of the total cumulative power will slightly increase the main frequency to 8 MHz except for two outliers.

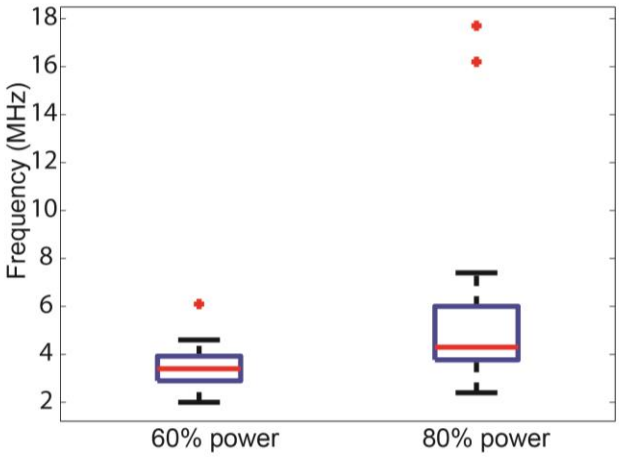

Figure 4.5. Photoacoustic accumulative signal power of the intraplaque lipids (n=36) as a function of frequency with two thresholds: 60% and 80% of the maximum accumulative power over the frequency range of 1 MHz to 35 MHz [median (red lines), 25/75 percentiles (box) and 5/95% confidence bands (whiskers), plus outliers (red dots)].

Fig. 4.6 shows the statistical results on quantified shape of the sPA signals. The location of the peak in the PA optical spectra for intraplaque lipids and adipose tissue are plotted in fig.4. 6(a) and the FWHM parameters are plotted in fig.4.6 (b). The shapes of the PA spectra of coronary plaque lipids acquired by the HF probe are in good agreement with the reference spectra. However, when acquired with the LF probe, the mean of FWHM is 1.6 times higher compared with the reference spectra.

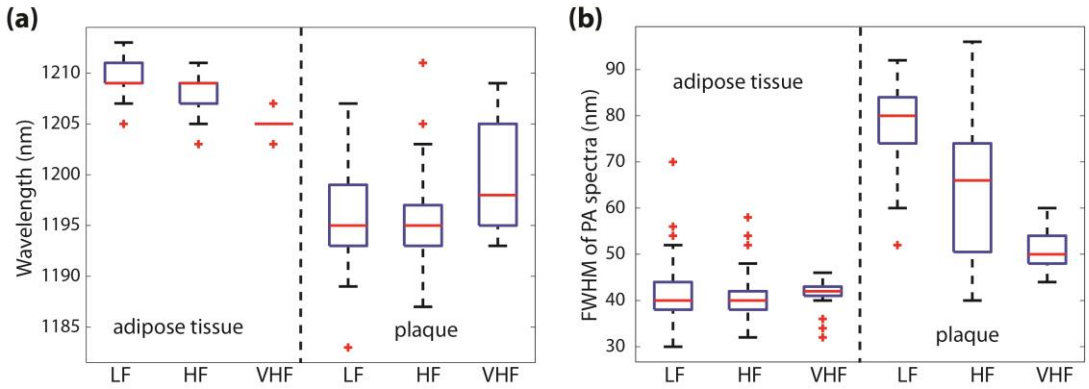

Figure 4.6. Comparison of photoacoustic (PA) spectral shape of intraplaque lipids and adipose tissue acquired with low frequency (LF), high frequency (HF) and very high frequency (VHF) acoustic probes: a) Peak location in the PA spectra; b) Full width half maxima (FWHM) of the PA spectra. The PA spectra acquired by the VHP is the reference spectra.

4 .4 Discussion

Frequency analysis on the PA signals (n=36) of human coronary intraplaque lipids *ex vivo* revealed that the majority (80%) of the PA signal power lies below 8 MHz for all samples except for two outliers. The frequency characteristics of the PA signal could be replicated by a simulation based on plaque lipid structures visualized by a histological lipid stain.
The relationship between the source size and the amplitude and frequency of the PA signal has been investigated before to characterise tissue microstructures [19-25, 30]. Although high frequency components of the PA signal may be specifically used to visualize microscopic spatial information of the absorbers in the medium [18, 19, 21, 31], their magnitude is much smaller than the stronger PA signal reflecting the macroscopic structures [16, 19]. Therefore, using a transducer that covers the frequency range in which the intraplaque lipids emit most of their PA signal significantly (lower than 8MHz in our results) increases the sensitivity of IVPA imaging of atherosclerosis plaque lipid. Currently, a transducer with a broad bandwidth to cover frequencies lower than 10 MHz and providing high resolution for IVUS imaging is not available. In the field of IVUS imaging, dual element transducers have been proposed to increase the bandwidth [32-34] . Although dual element transducers have been proposed also for IVPA imaging applications, the lower frequency range of the acoustic spectra is still not covered: Ji et al. have recently developed an intravascular confocal IVPA catheter with dual-element identical transducers with centre frequencies of 19 MHz [35, 36]; and Li et al. has developed a catheter for 35 and 80 MHz frequencies [35]. These publications prove the possibilities of applying similar technologies in fabricating an IVPA catheter with a large bandwidth.

The shapes of the PA optical spectra of coronary plaque lipids acquired by the HF probe are in good agreement with the optical spectra reported in the previous publications [28, 37]. However, when acquired with the LF probe, these optical spectral shapes are noticeably broader while keeping the same peak locations. This broadening of the optical spectra is consistent with the complex constitution of the plaque in the vessel wall and has been reported before by Allen et al. [38]. The complex structure of such plaques consist of not only lipids but also other constituents such as collagen (with an absorption peak at 1180 nm [39]), calcium (with a flat optical spectra [40]). Mixture of these plaque constituents' optical spectra is more pronounced when the PA signals are received with a LF probe because of the larger effective spatial kernel in which the detected signal originates. As expected there was no difference in the shape of the optical spectra of pure lipid samples for the LF, HF and VHF probes in a phantom, supporting the hypothesis that the broadening of the optical spectra acquired by the LF probe *ex vivo* is due to mixing of signals generated by different plaque constitutes other than lipids. It has been shown that intraplaque lipids can be detected with a single optical wavelength approach (around absorption peak of lipids) [41, 42]. This approach can readily be used with a LF probe since the location of the absorption peak of lipids remains the same. However, multiple optical wavelengths approach provides a more reliable intraplaque lipid detection [28, 43]. If multiple optical wavelength approach with a LF probe is desired, a new calibration is required since the shape of the optical spectra of intraplaque lipids can be broader if other plaque constitutions are within the effective spatial kernel of the transducer.

Catheter prototypes that rely on typical IVUS transducers require a high pulse energy to produce sufficiently strong PA signals [44-47]. Video rate imaging requires a pulse rate of at least 5-10 kHz per optical wavelength. It means that the optical power delivered to the vessel becomes very high, if such pulse energies can even be produced at optical wavelengths that generate lipid contrast. The lack of sufficiently fast lasers has hampered translation of IVPA imaging to real-time in vivo experiments, and further into clinical applications. We have previously shown that by exploiting the relative difference between the IVPA signal strengths at only two wavelengths (1718 and 1734 nm), we could successfully detect and differentiate between the plaque lipids and peri-adventitial fat in human coronary arteries ex vivo (Wu, et al. 2015). However, the sensitivity in capturing the PA signal with low pulse energy is a key factor to translate the technology to the clinic. The sensitivity of IVPA catheters can be increased by more than 20 dB by matching the frequency response of the receiving transducer to the low frequency range, below 8 MHz, that we observed in this study to maintain most of the signal power (80% of the PA power). Such a device would enable imaging with lower pulse energy, which may open up opportunities for new fast laser sources with moderate output power.

It is known that under the conditions of thermal and stress confinement, the pressure rise in tissue for short laser pulses is nearly isotropic. It is followed by a compression at nearly constant temperature during propagation of the laser-induced compressive wave into the medium, and a transition to a state with negative pressure when the negative reflection from the free surface arrives at the detector surface [48] We did not include the effect of the laser pulse length (5 ns) on the frequency content of the PA signals in our study since the frequency of the 5 ns short pulse falls in the range much higher than the investigated frequency range (up to 35 MHz) in this study.

4 .5 Limitations

Our statistical analysis were done on a rather small sample size (n=36). Moreover, the arteries were donated from non-symptomatic patients with perhaps smaller plaque size compared with symptomatic patients. This suggests that the main frequency of the PA signals to be at even lower frequencies for patients with bigger fatty structures in larger plaques. Further comprehensive investigations are needed to develop a reliable statistical model. Also we did not investigate the possible effect of freezing the tissue samples on the optical and acoustical properties of their PA signal. Finally, the differences in the exact shape of the acoustic spectra of the PA signal (figure 4a) is due to various parameters which are different in experiment and simulation such as, the discretization of the input initial pressure source; dimensions in which the simulation is performed (2D instead of 3D) and the shape of the lipid droplets after ORO staining.

4 .6 Conclusion

Based on our frequency analysis of intraplaque lipid photoacoustic signals, it is expected that the sensitivity of intravascular photoacoustic imaging for intraplaque lipids will be significantly improved if ultrasound transducers with large bandwidth which covers the lower frequencies (1-10 MHz) are used.

Acknowledgment

We greatly thank all colleagues who made the experiments possible for their help and support: Hans Bosch, Geert Springeling, and Robert Beurskens from the Department of Biomedical Engineering, Erasmus MC, the Netherlands.

This research is supported by the Dutch Technology Foundation STW, which is part of the Netherlands Organisation for Scientific Research (NWO), and which is partly funded by the Ministry of Economic Affairs (Grant number: 13169).

References

1. World-Health-Organization, *Cardiovascular diseases (CVDs)*. January 2015.
2. Schaar, J.A., et al., *Terminology for high-risk and vulnerable coronary artery plaques. Report of a meeting on the vulnerable plaque, June 17 and 18, 2003, Santorini, Greece.* Eur Heart J, 2004. **25**(12): p. 1077-82.
3. Virmani, R., et al., *Lessons from sudden coronary death - A comprehensive morphological classification scheme for atherosclerotic lesions.* Arteriosclerosis Thrombosis And Vascular Biology, 2000. **20**(5): p. 1262-1275.
4. Davies, M.J. and A.C. Thomas, *Plaque fissuring--the cause of acute myocardial infarction, sudden ischaemic death, and crescendo angina.* British heart journal, 1985. **53**(4): p. 363.
5. Schaar, J.A., et al., *Intravascular palpography for vulnerable plaque assessment.* J Am Coll Cardiol, 2006. **47**(8 Suppl): p. C86-91.
6. Puri, R., et al., *Exploring coronary atherosclerosis with intravascular imaging.* Int J Cardiol, 2013. **168**(2): p. 670-9.
7. Choudhury, R.P., V. Fuster, and Z.A. Fayad, *Molecular, cellular and functional imaging of atherothrombosis.* Nat Rev Drug Discov, 2004. **3**(11): p. 913-25.
8. Allen, T.J., et al., *Spectroscopic photoacoustic imaging of lipid-rich plaques in the human aorta in the 740 to 1400 nm wavelength range.* J Biomed Opt, 2012. **17**(6): p. 061209.
9. Niccoli, G., et al., *Advances in mechanisms, imaging and management of the unstable plaque.* Atherosclerosis, 2014. **233**(2): p. 467-477.
10. Jansen, K., G. van Soest, and A.F.W. van der Steen, *Intravascular Photoacoustic Imaging: A New Tool for Vulnerable Plaque Identification.* Ultrasound in medicine & biology, 2014. **40**(6): p. 1037-1048.
11. Puri, R., M.I. Worthley, and S.J. Nicholls, *Intravascular imaging of vulnerable coronary plaque: current and future concepts.* Nature Reviews Cardiology, 2011. **8**(3): p. 131-139.
12. Wang, H.W., et al., *Label-free bond-selective imaging by listening to vibrationally excited molecules.* Phys Rev Lett, 2011. **106**(23): p. 10.
13. Jansen, K., et al., *Intravascular photoacoustic imaging of human coronary atherosclerosis.* Opt Lett, 2011. **36**(5): p. 597-9.
14. Wang, B., et al., *Intravascular photoacoustic imaging of lipid in atherosclerotic plaques in the presence of luminal blood.* Opt Lett, 2012. **37**(7): p. 1244-6.

15. Wang, P., J.R. Rajian, and J.X. Cheng, *Spectroscopic Imaging of Deep Tissue through Photoacoustic Detection of Molecular Vibration.* J Phys Chem Lett, 2013. **4**(13): p. 2177-2185.
16. Wang, L.V. and S. Hu, *Photoacoustic tomography: in vivo imaging from organelles to organs.* Science, 2012. **335**(6075): p. 1458-62.
17. Diebold, G.J., M.I. Khan, and S.M. Park, *Photoacoustic "Signatures" of Particulate Matter: Optical Production of Acoustic Monopole Radiation.* Science, 1990. **250**(4977): p. 101-104.
18. Yang, Y., et al., *Photoacoustic tomography of tissue subwavelength microstructure with a narrowband and low frequency system.* Applied Physics Letters, 2012. **101**(3): p. 034105.
19. Xu, G., et al., *Photoacoustic Spectrum Analysis for Microstructure Characterization in Biological Tissue: Analytical Model.* Ultrasound in Medicine and Biology, 2015. **41**(5): p. 1473-1480.
20. Hysi, E., D. Dopsa, and M.C. Kolios. *Photoacoustic radio-frequency spectroscopy (PA-RFS): A technique for monitoring absorber size and concentration*. 2013.
21. Kumon, R.E., C.X. Deng, and X. Wang, *Frequency-domain analysis of photoacoustic imaging data from prostate adenocarcinoma tumors in a murine model.* Ultrasound Med Biol, 2011. **37**(5): p. 834-9.
22. Patterson, M.P., et al., *Optoacoustic characterization of prostate cancer in an in vivo transgenic murine model.* J Biomed Opt, 2014. **19**(5): p. 056008.
23. Patterson, M.P., et al. *Optoacoustic signal amplitude and frequency spectrum analysis laser heated bovine liver ex vivo*. in *Ultrasonics Symposium (IUS), 2011 IEEE International*. 2011.
24. Saha, R.K. and M.C. Kolios, *A simulation study on photoacoustic signals from red blood cells.* J Acoust Soc Am, 2011. **129**(5): p. 2935-43.
25. Strohm, E.M., E.S. Berndl, and M.C. Kolios, *Probing red blood cell morphology using high-frequency photoacoustics.* Biophys J, 2013. **105**(1): p. 59-67.
26. Xu, G., et al., *The functional pitch of an organ: quantification of tissue texture with photoacoustic spectrum analysis.* Radiology, 2014. **271**(1): p. 248-54.
27. Jansen, K., et al., *Spectroscopic intravascular photoacoustic imaging of lipids in atherosclerosis.* Journal of Biomedical Optics, 2014. **19**(2): p. 026006-026006.
28. Jansen, K., et al., *Lipid detection in atherosclerotic human coronaries by spectroscopic intravascular photoacoustic imaging.* Optics Express, 2013. **21**(18): p. 21472-21484.
29. Treeby, B.E. and B.T. Cox, *k-Wave: MATLAB toolbox for the simulation and reconstruction of photoacoustic wave fields.* J Biomed Opt, 2010. **15**(2): p. 021314.
30. Gertsch, A.G., et al. *Toward characterizing the size of microscopic optical absorbers using optoacoustic emission spectroscopy*. 2010.
31. Wang, S., et al., *Quantitative detection of stochastic microstructure in turbid media by photoacoustic spectral matching.* Applied Physics Letters, 2013. **102**(11): p. 114102.
32. Jianguo, M., et al. *Dual frequency transducers for intravascular ultrasound super-harmonic imaging and acoustic angiography*. in *Ultrasonics Symposium (IUS), 2014 IEEE International*. 2014.
33. Teng, M., et al., *Multi-frequency intravascular ultrasound (IVUS) imaging.* Ultrasonics, Ferroelectrics, and Frequency Control, IEEE Transactions on, 2015. **62**(1): p. 97-107.
34. Qiu, W., et al., *A novel dual-frequency imaging method for intravascular ultrasound applications.* Ultrasonics, 2015. **57**(0): p. 31-35.
35. Li, X., et al., *Intravascular photoacoustic imaging at 35 and 80 MHz.* J Biomed Opt, 2012. **17**(10): p. 106005.

36. Ji, X., et al., *Intravascular confocal photoacoustic endoscope with dual-element ultrasonic transducer.* Opt Express, 2015. **23**(7): p. 9130-6.
37. Caplan, J.D., et al., *Near-infrared spectroscopy for the detection of vulnerable coronary artery plaques.* J Am Coll Cardiol, 2006. **47**(8 Suppl): p. C92-6.
38. Allen, T.J., et al., *Spectroscopic photoacoustic imaging of lipid-rich plaques in the human aorta in the 740 to 1400 nm wavelength range.* Journal of Biomedical Optics, 2012. **17**(6): p. 061209-10.
39. Tsai, C.L., J.C. Chen, and W.J. Wang, *Near-infrared absorption property of biological soft tissue constituents.* J Med Biol Eng, 2001. **21**(1): p. 7-14.
40. Fleming, C.P., et al., *Depth resolved detection of lipid using spectroscopic optical coherence tomography.* Biomedical Optics Express, 2013. **4**(8): p. 1269-1284.
41. Wang, P., et al., *High-speed Intravascular Photoacoustic Imaging of Lipid-laden Atherosclerotic Plaque Enabled by a 2-kHz Barium Nitrite Raman Laser.* Scientific reports, 2014. **4**.
42. Wang, B., et al., *In vivo Intravascular Ultrasound-guided Photoacoustic Imaging of Lipid in Plaques Using an Animal Model of Atherosclerosis.* Ultrasound in medicine & biology, 2012.
43. Wu, M., et al., *Specific imaging of atherosclerotic plaque lipids with two-wavelength intravascular photoacoustics.* Biomedical Optics Express, 2015. **6**(9): p. 3276-3286.
44. Sethuraman, S., et al., *Spectroscopic intravascular photoacoustic imaging*, in *2007 Ieee Ultrasonics Symposium Proceedings, Vols 1-6*. 2007, Ieee: New York. p. 1188-1191.
45. Zhang, J., et al., *Characterization of lipid-rich aortic plaques by intravascular photoacoustic tomography: ex vivo and in vivo validation in a rabbit atherosclerosis model with histologic correlation.* J Am Coll Cardiol, 2014. **64**(4): p. 385-90.
46. Karpiouk, A.B., et al., *Feasibility of in vivo intravascular photoacoustic imaging using integrated ultrasound and photoacoustic imaging catheter.* J Biomed Opt, 2012. **17**(9): p. 96008-1.
47. Li, Y., et al., *High-speed intravascular spectroscopic photoacoustic imaging at 1000 A-lines per second with a 0.9-mm diameter catheter.* Journal of Biomedical Optics, 2015. **20**(6): p. 065006-065006.
48. Paltauf, G. and H. Schmidt-Kloiber, *Microcavity dynamics during laser-induced spallation of liquids and gels.* Applied Physics A, 1996. **62**(4): p. 303-311.

Chapter 5. Real-time volumetric lipid imaging in vivo by intravascular photoacoustics at 20 frames per second

Wu M, Geert Springeling, Matija Lovrak, et al. Real-time volumetric lipid imaging in vivo by intravascular photoacoustics at 20 frames per second. *Biomedical optics express, 2017, 8(2), 943-953*

Abstract

Lipid deposition can be assessed with combined intravascular photoacoustic/ultrasound (IVPA/US) imaging. To date, the clinical translation of IVPA/US imaging has been stalled by a low imaging speed and catheter complexity. In this paper, we demonstrate imaging of lipid targets in swine coronary arteries in vivo, at a clinically useful frame rate of 20 s^{-1}. We confirmed image contrast for atherosclerotic plaque in human samples ex vivo. The system is on a mobile platform and provides real-time data visualization during acquisition. We achieved an IVPA signal-to-noise ratio of 20 dB. These data show that clinical translation of IVPA is possible in principle.

5.1 Introduction

Cardiovascular diseases (CVDs) are the leading cause of death worldwide. In 2012, 17.5 million people died from CVDs, representing 31% of all the global deaths. Particularly, 42% of these CVD deaths are due to coronary artery disease (CAD), which is most often triggered by the rupture of vulnerable atherosclerotic plaque and ensuing thrombosis [1, 2]. A vulnerable plaque is commonly described as a lipid-rich necrotic core, covered by a thin fibrous cap with macrophage infiltration [3]. These plaques have been implicated in worse short-term and long-term outcomes of coronary interventions, as they may destabilize by intracoronary instrumentation during the intervention, or spontaneously at a later stage. The identification of the vulnerable plaque requiring information on the structure and composition of the plaque [4], can have an important role for guiding the diagnosis and treatment of CAD.

All commercially available intravascular imaging modalities can detect one or more of the defining features of a vulnerable plaque, but none provides conclusive identification [5]. Intravascular optical coherence tomography is well positioned for imaging fibrous cap thickness but has insufficient imaging depth to fully visualize the artery wall [6], and tissue characterization requires a high level of user expertise [7]. Intravascular ultrasound (IVUS) can usually see the entire vessel, but lacks resolution and soft tissue type specificity. This has led to the proposal of multimodal imaging strategies [8]. Optical spectroscopies are ideal for discriminating between tissue types, capitalizing on specific absorption features [9, 10]. IVUS has been combined recently with near-infrared spectroscopy (NIRS), which provides information about the presence of lipid-core plaque, but still is unable to measure its depth relative to the lumen border [11].

Combined intravascular photoacoustic (IVPA) and IVUS imaging is emerging as a promising technology for localization, characterization and quantification of coronary atherosclerotic plaque lipids. IVPA imaging, generating ultrasound signal by the absorption of a short laser pulse in the tissue, is capable of imaging the composition of the artery wall with an adequate imaging depth and resolution based on the optical absorption contrast between different tissues [12, 13]. Tissue contrast in IVPA can be chosen by tuning the excitation wavelength to a specific absorption band of the imaging target. We target atherosclerotic plaque lipid, the most prevalent marker for identifying vulnerable plaques, by choosing an excitation wavelength that excites a PA signal from lipids [12, 14-17], and ideally from atherosclerotic lipids alone [18-20]. Its co-registered IVUS image provides the complementary structure information of the artery wall. Although IVPA/US imaging potentially offers valuable information for assessment of plaque vulnerability, the slow imaging speed and the difficulty in design and fabrication of a miniature flexible catheter have presented as major challenges for translation of IVPA/US imaging into an in vivo or clinical application. An intensive research effort is ongoing towards the further development of IVPA/US imaging systems. Imaging speed is primarily limited by laser pulse rate: with the introduction of 500 Hz to 2 kHz repetition rate laser systems, operating at the wavelengths of lipid absorption peaks near 1.2 μm or 1.7 μm, the IVPA/US lipid imaging speed has recently increased to about 1 frame per second (fps) [21-23]. Use of a more conventional laser wavelength facilitates speed but offers limited biological image contrast [24].

The routine for intravascular imaging is to perform a pullback while acquiring a series of cross-sectional images, which together form a volume scan. If using the closest relative, IVUS imaging, as a reference, scanning a vessel with a pullback speed of 0.5-1 mm/s and a frame rate of 20-50 fps is required for IVPA imaging.

In this paper, we demonstrate an IVPA/US system with a 1.3 mm outer diameter flexible catheter, imaging coronary lipids at the speed of 20 fps, comparable to the speed of a conventional commercial IVUS system [25, 26]. This frame rate is the minimum usable acquisition speed for in vivo volumetric (pullback) imaging, if adequate sampling is required in the presence of cardiac motion. We demonstrate the imaging performance in vivo in a healthy swine model with an introduced lipid target, and on a human atherosclerotic coronary artery sample ex-vivo.

5.2 Methods and materials

5.2.1 IVPA/US image acquisition and real-time visualization

The schematic of the high-speed IVPA/US imaging system is shown in fig.5.1.The laser source in the system (FQ-OPO, Elforlight Ltd, Daventry, UK) is a periodically-poled $LiNbO_3$ OPO pumped by a pulsed Nd:YAG laser, which in turn is pumped by a CW diode. The laser pulse duration is approximately 10 ns, the maximum output pulse energy of the laser is 80 μJ/pulse and the pulse repetition rate is of 5 kHz. The tuning range of the laser is from 1700 to 1750 nm. The laser output is coupled into a multimode optical fiber with a core diameter of 100 μm and connected to the 1.3 mm IVPA/US catheter through an optical rotary joint (Princetel, Hamilton, NJ, USA) and an electrical slip ring (LPT025, JINPAT Electronics, Shenzhen, China) inside the scanning stage. The IVPA/US catheter is based on the design we previously described in [27], consisting of a 100 μm diameter angle polished fiber (angled at 34 degree, low OH, Pioneer Optics, USA), an ultrasound transducer element (40 MHz central frequency, 50% bandwidth, Blatek, USA), a tip assembly made from polyether ether ketone (PEEK), a metal torque coil and a 1.3 mm outer diameter polyethylene (PE) sheath. An ultrasound pulser (AVL-2-PS-P, Avtech Electrosystems Ltd, New York, NY, USA) is used to transmit 80 V amplitude pulses for pulse-echo imaging. A pulse/delay generator (BNC model 575, Berkeley Nucleonics Corporation, San Rafael, CA, USA) provided timing and triggering signals to the laser, digitizer and the ultrasound pulser. The time delay between the PA and US signal is 10 μs. The received data were 43dB amplified (AU1263, MITEQ, Long Island, NY, USA), band pass filtered (13–60 MHz 5th order Butterworth, custom built), digitized and transferred by a data acquisition card with 14 bits digitization and 400 MS/s sampling rate (PX14400, Signatec, New York, NY, USA) installed in a personal computer (PC). The data acquisition software was developed in C++ (Microsoft Visual Studio 10) to acquire and display the recorded data in real time. Simple data processing including decimation, truncation, absolute value, normalization, and scan-conversion to Cartesian coordinates was applied to the acquired data before real time data display. A video of data acquisition and visualization with the software interface is provided in Visualization. 1. Rotation (313518, Maxon motor, Sachseln, Switzerland) and translation motors (143967, Maxon motor, Sachseln, Switzerland) were combined for helical scanning, driving the catheter rotation at 1200 rpm and pullback at 0.1~1 mm/s. One cross-

sectional image was composed of 250 A-lines and the whole system is capable of IVPA/US imaging at 20 fps. All the devices were placed in a portable trolley for easy transportation.

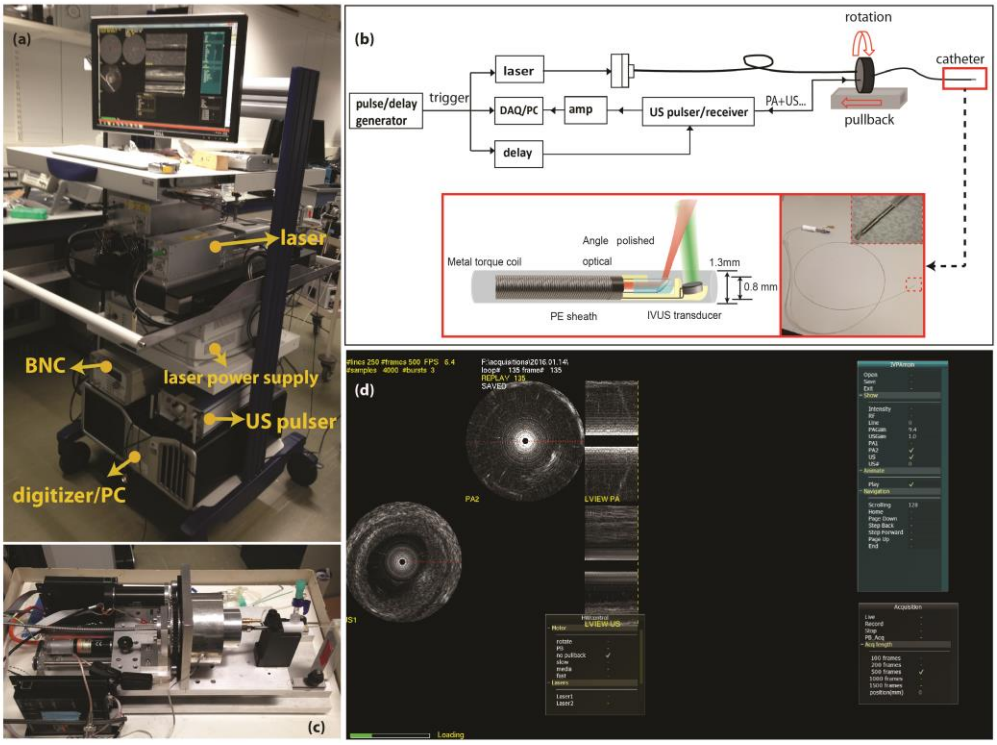

Figure 5.1. Real-time IVPA/US imaging system. (a) Photo of the mobile IVPA/US system. (b) Schematic of the IVPA/IVUS imaging system composition and illustration of the IVPA catheter components. (c) Photo of the pullback unit. (d) Data acquiring and display with the homemade software interface on a human coronary artery sample ex vivo (Visulization 1)

5.2.2 Data processing

Further signal processing on the data was performed in Matlab (R2016a; The Mathworks, Natick, MA, USA) offline. All received PA and US data were decimated, digitally band pass filtered from 10 to 60 MHz, envelope filtered, median filtered, denoised and converted for display as in our previous work [12]. In the in vivo data, we noticed image wobble in the pullback due to variations in tip rotation speed, possibly related to cardiac motion. We applied a global rotational block matching correction based on the correlation of subsequent IVUS frames [28]. After this motion correction, we enhanced the PA signal to noise ratio (SNR) by averaging each A-line in a 3×2 (lines×frames) averaging kernel. For instance, the PA signal at i^{th} A-line and j^{th} frame, $P_{i,j}$, was averaged with its two adjacent A-line signals at the same frame $P_{i\pm1,j}$ and the PA signal at the same three A-lines in the next frame, $P_{i\pm1,j+1}$.

Furthermore, in vivo imaging is performed through the PE sheath, which attenuates PA signal and introduces strong reflection artifacts. The reflection artifacts are highly correlated throughout the pullback recording. The reference reflection artifact PA signal was constructed from the PA images without lipid target and was used to cancel the artifacts in images with lipid target.

5.2.3 Human coronary artery sample preparation

One artery sample (LAD, 48 years old man) was collected at autopsy from the Department of Pathology of Erasmus Medical Center (MC), after obtaining consent from the relatives. The research protocol was sanctioned by the Medical Ethics Committee of Erasmus MC (MEC-2007-081). The coronary artery was frozen within 2h after autopsy and stored at -80° until analysis a few months later. Prior to analysis, the artery was thawed and measured within several hours. In the measurement, metal needles were used to fix the artery specimen inside a small container filled with D_2O-saline and register the pullback locations. Figure 2(a) shows a photo of the prepared artery sample for the measurement. The IVPA/US measurement was performed at room temperature at the wavelength of 1720 nm. To maximize the PA SNR, the PE sheath was removed during the measurement. 500 frames data were acquired for one pullback and the pullback speed was set to be 0.1mm/s. All the IVPA/IVUS images were non-averaged.

After the measurement, we cut the part of the artery sample imaged, embedded in optimal cutting temperature compound (Tissue-Tek®, Sakura Finetek Europe B.V., Alphen a/d Rijn, The Netherlands), and stored it at -80°C until further processing. For histology, we sliced the whole frozen artery block into a series of 10 μm thick sections. Oil Red O (ORO) staining was applied to all these sections to detect lipids.

5.2.4 In vivo IVPA/US imaging in swine coronary lipid model

To further test the imaging system, an in vivo IVPA/US experiment was performed on a healthy farmbred (Yorkshire-landrace) swine. The animal was sedated using Zoletil 100 (Virbac Nederland BV, Barneveld, The Netherlands), Sedazine (AST Farma BV, Oudewater, The Netherlands) and Atropine (Pharmachemie BV, Haarlem, The Netherlands), and anesthesia was maintained using pentobarbital (10-15 mg/kg/hr) while connected to a ventilator as described before [29]. The protocol was approved by the Erasmus MC Animal Ethics committee and was performed in accordance with the Guide for Care and Use of Laboratory Animals [30]. Following anesthesia and a surgical cut-down, a sheath was introduced into the carotid artery. Then a guiding catheter was advanced to the right coronary artery (RCA) for stent placement and intravascular imaging. Under guidance of angiography a small piece of pork lard was delivered into the coronary artery to mimic the plaque lesion as described by Lovrak et al [31]. The pork lard (lipid target) was fixed at its two ends with two small, modified, double-layered stents on the balloon catheter (Pantera Pro 4.0/15; Biotronik SE & Co. KG, Berlin, Germany). Figure 5.3(a) shows the photo of the lipid rich material with stents mounted on the balloon catheter. To prevent the two stents from being pushed apart while inflating the balloon, we connected them with the black surgical wires.

Then, the IVPA/US catheter was advanced into the RCA with a GuideLiner catheter (6F, Vascular Solutions, Minneapolis, MN, USA). The metal stents and the catheter were radio-opaque, thus, the pullback locations could be easily tracked by X-ray imaging [Fig. 5.3 (b)]. In this way, IVPA/US pullback recording was arranged to cover the lipid target region (the region in between the two stents) at a speed of 0.5mm/s. Each pullback recording contains at least 200 frames. The in vivo experiment was also performed at 1720 nm, but unlike the ex vivo experiment, it imaged through the PE sheath. During the experiment, we continuously flushed

the artery with heavy water-based saline. After the experiment, we sacrificed the pig, cut the artery open and confirmed the presence of the lipid target inside the RCA.

5.3 Results

5.3.1Ex vivo IVPA/US imaging of human coronary artery

We imaged a human atherosclerotic plaque specimen, obtained from autopsy. Figure 2 shows the combined IVUS/IVPA data. An atherosclerotic lesion with a variable amount of intraplaque lipid, photographed in its holder in Fig. 2(a), is visualized by IVPA/US. The lipid content increases in the pullback direction, from left to right in Fig. 2(b), appearing from 3 o'clock to 7 o'clock in the 3D reconstruction of the pullback data. Histology validations by Oil Red O lipid stain are shown at two pullback locations, indicated with yellow and blue contours in Fig. 2(b). In the combined IVPA/US images [Fig. 2(c) and 2(e)], the IVPA signal can be clearly appreciated at the corresponding thickened intima region within the artery wall (from 2 o'clock to 7 o'clock). This suggests the presence of a lipid-rich plaque, an observation that is confirmed by comparison with the histology. The proximal location [Figs. 2(c) and 2(d)] shows a bright IVPA signal corresponding to a dense lipid-laden intima. The more distal location [Figs. 2(e) and 2(f)] exhibits a markedly lower IVPA signal, and a less extensive lipid infiltration on histology.

IVPA achieved full visualization of the lipid-rich lesion throughout the depth of the plaque. The signal-to-noise ratio (SNR) of the PA signal in the plaque region in the image is approximately 20 dB without any averaging, validating the capability of plaque visualization with enough imaging depth by IVPA imaging at 1.7 μm in coronary artery.

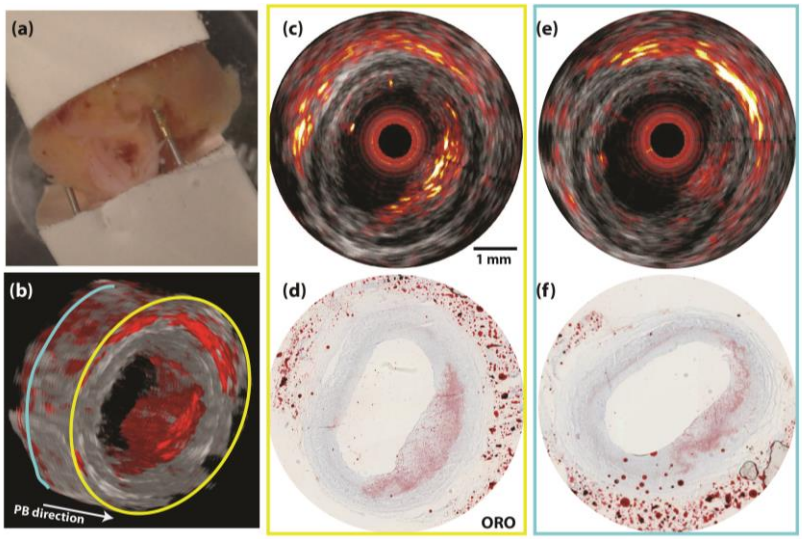

Figure 5.2. IVPA/US cross-sectional image of an atherosclerotic human coronary artery. (a) Photo of the human LAD sample fixed inside a holder. (b) 3D reconstruction of the pullback IVPA/US images. (c) Merged IVPA/US image of the plaque at locations with large plaque volume (the location with a yellow contour) and (e) with small plaque volume (the location with a blue contour). (d) and (f) The ORO histology staining at the imaging plane corresponding to images of (c) and (e). The dynamic range is 35 dB in IVUS image and 20 dB in IVPA image. No averaging was applied to IVUS or IVPA data.

5.3.2 In vivo IVPA/US imaging of swine coronary artery

In vivo IVPA/US imaging of a swine coronary artery with an artificial plaque is shown in Fig. 5.3. A lipid target was introduced into the coronary artery of a healthy animal by attaching a piece of pork fat to a pair of coronary stents and deploying them to attach it to the vessel wall [Fig. 3(a)]. Stents were introduced on a balloon under angiography guidance [Fig. 5.3(b)]. We acquired a pullback data set using the experimental IVPA/US catheter and system. A longitudinal section of the pullback IVPA/US data containing the lipid target is shown in Fig. 5.3(c), along with cross-sectional images at two selected pullback locations; one inside the lipid region (yellow line) and the other one outside (blue line). The lipid target can also be seen in the IVUS images as an intraluminal, echogenic object, and this was used to delineate the target by the dotted contour in Figs. 5.3(c) and 5.3(d). In the IVPA/US images of the lipid target [Figs. 5.3(d)-3(f)], a bright PA signal at 6 o'clock to 9 o'clock inside the lumen, generated from the lipid, is clearly observed with an SNR≈18 dB (marked with a yellow contour). As a reference, the characteristic PA signal disappears in absence of the lipid target; remaining signal is concentric with the catheter and is attributed to artifacts arising from signal generation in the catheter sheath. The entire IVPA/US pullback data display (300 frames data) video is shown in Visualization 2.

By IVUS, the lipid target appears larger than by IVPA: the IVPA does not detect the entire lipid inclusion. We attribute this to a combination of catheter limitations and image processing: During imaging, the target did not align perfectly with the artery wall, as expected, and as a result was very close to the catheter [Fig. 5.3(d)]. As described in our previous work [27], an IVPA catheter with a longitudinal beam offset has a low sensitivity to targets that are in close proximity to the transducer due to small optical/acoustic beam overlap. Secondly, imaging artifacts originating from light absorption in the catheter sheath overlapped with the lipid signal. Additional data processing to suppress the artifacts partially suppressed the lipid signal, while some residual artifacts remained, indicated with white arrows in Fig. 5.3(e).

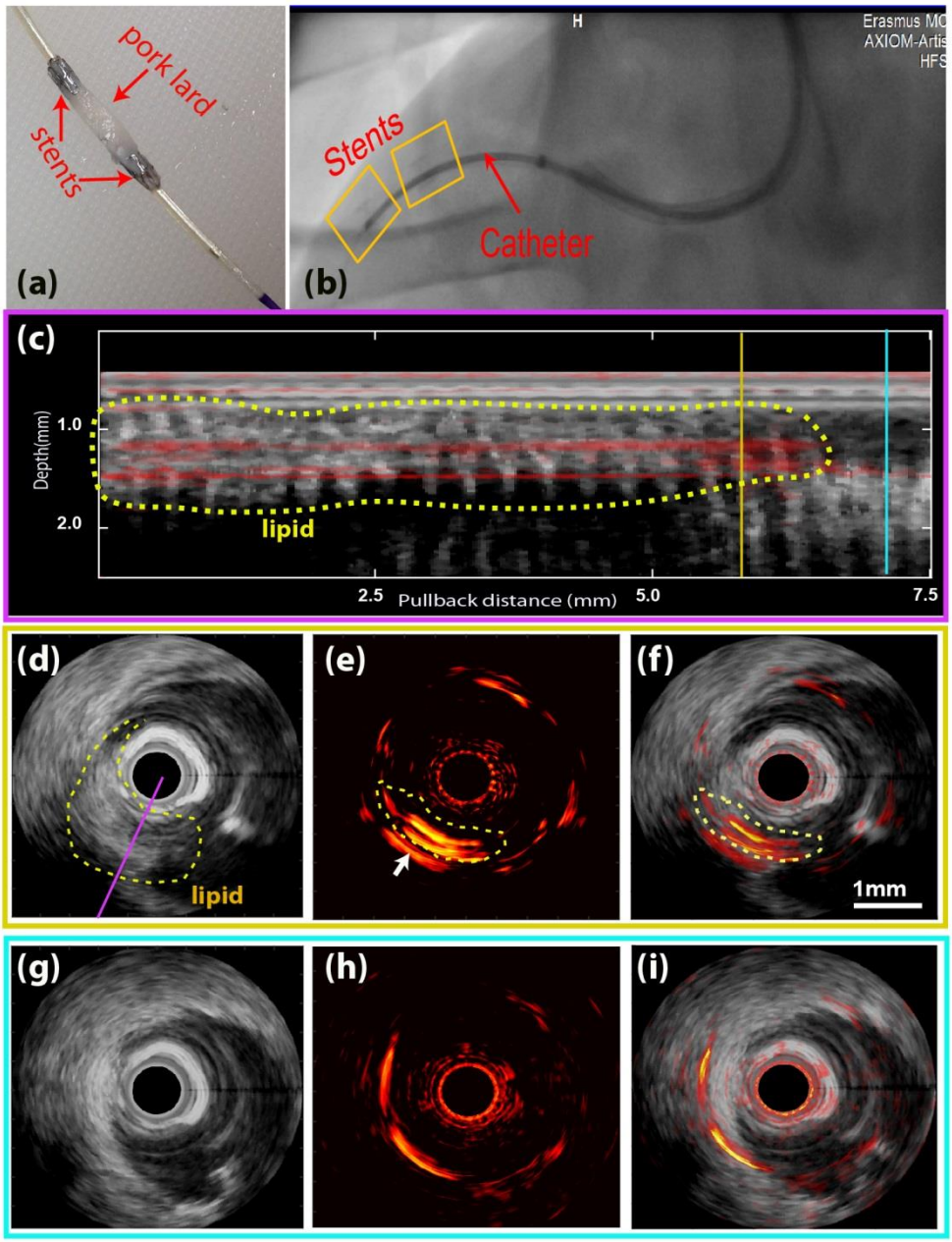

Figure 5.3. In vivo IVPA/US imaging result on a swine model. (a) Stents with lipid target mounted on a balloon catheter. (b) X-ray imaging of the pullback location. The stents were inside the yellow boxes and the lipid target located in between the two stents. (c) Longitudinal view of the pullback merged IVPA/US data at an angle intersecting with the lipid object (indicated with a purple line in (d)). (d,e,f) Cross-sectional IVUS, IVPA, and merged IVPA/US image at the pullback location indicated with a yellow line in (c). (g,h,i) Cross-sectional IVUS, IVPA and merged IVPA/US image at the pullback location indicated with a blue line in (c).The dynamic range is 32 dB for IVUS images and 18 dB for IVPA images; scale bar in (f) applies to all of (d)-(i).

5.4 Discussion

In this work, we demonstrated in vivo IVPA/US imaging based on a system using a 5 kHz laser with a flexible 1.3 mm catheter, capable of volumetric lipid detection in coronary arteries at 20 frames per second. We validated the imaging system performance on a human coronary artery ex vivo and on a swine coronary artery in vivo. It is the first in vivo IVPA/US imaging in a coronary artery reported to date, acquiring images of coronary lipid in this highly mobile,

challenging environment. Our IVPA/US imaging system significantly increased the imaging speed from 1 fps (the fastest imaging speed reported so far for a lipid-imaging IVPA system) to 20 fps [21-23, 32]. The operating parameters of our implementation of this technology match those desired of a clinical imaging system in terms of acquisition speed, operating wavelength, and scan method. The catheter proved to be sufficiently robust for in vivo imaging. Further miniaturization of the device is possible and has been demonstrated [32, 33]; the outer diameter could be reduced to < 1 mm with a smaller torque coil and outer sheath.

The IVPA/US system performs acquisition and real-time display of dual-modality data, meaning the data is visualized during imaging at the same rate that it is acquired. This is a key step for usability of IVPA in real-world settings. The image optimizations we performed off-line in the in vivo experiments do not require user intervention and could be incorporated straightforwardly in the real-time visualization (inducing a one-frame display delay).

The laser source in our system has a high repetition rate but moderate pulse energy. Partially due to ineffective coupling and scattering at the catheter tip, the optical exposure is less than 0.4 J/cm^2 at 1.7 μm, which is below the 1 J/cm^2 threshold specified by the ANSI laser safety standard [22]. Despite using a pulse energy which is one order of magnitude lower than that used previously in IVPA/US systems working at 1.7 μm, the PA SNR achieved in our imaging system was 20 dB, comparable to earlier reports [22, 23]. We used pork lard as a lipid target for in vivo imaging, which has a different lipid composition, and thus a slightly different absorption spectrum, compared to lipid-rich plaque [20]. However, at the selected wavelength (1720 nm), both pork lard and plaque generate strong PA signals. An alternative synthetic plaque is being developed, containing the same types of lipids as in plaques to better mimic the plaque lipid signature [31]. This material can be introduced in a similar manner as we did in the present study.

Some challenges clearly remain for the clinical translation of IVPA/US imaging, particularly in the catheter design. In a typical miniature non-collinear IVPA catheter, the offset between the acoustic and optical beams, longitudinally or laterally, leads to a low PA SNR when targets are close to the transducer [27]. Collinear catheter designs do not face this problem, but are more prone to image artefacts resulting from near-field optical absorption [34]. Another difficulty in catheter design is the sheath material, which needs to be transparent for both ultrasound and light (at 1.7 μm). The polyethylene (PE) material in our current catheter sheath is abundant in C-H bonds as lipids, which makes it a strong absorber at wavelengths providing lipid-specific contrast. A PE sheath absorbs almost half of the PA excitation energy, leading to a reduction in PA SNR and strong reflection artefacts due to echoes of the sheath-generated signal in IVPA image (fig. 5.5). Especially, during the in vivo swine experiment, the artifact from PE sheath appears close to the lipid target, making the PA signal from lipid target a mixture with sheath artifact, which is difficult to completely cancel without losing PA signal originating from tissue. A direct comparison between images with and without sheath shows a similar reduction in PA energy [24].

Attenuation and artifacts affect the quality of in vivo IVPA images compared to the ex vivo IVPA results, collected without sheath. Fluorinated polymers, such as PTFE are an interesting

alternative, but tend to have suboptimal mechanical and acoustic properties in their crystalline forms. Fabrication of amorphous fluorinated polymer, such as perfluoro-3-butenyl-vinyl ether (CytopTM), which is flexible and has a 95% transmittance of the light at 1.7 μm [35], in tube form would make these promising materials available for evaluation as catheter sheaths.

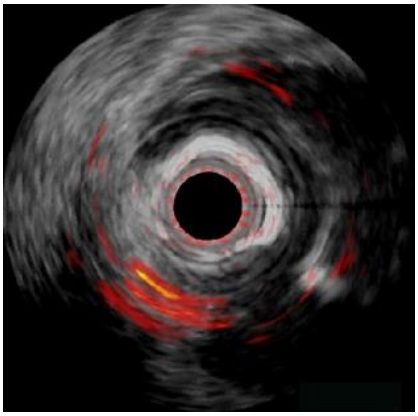

Figure 5.4. in vivo IVPA/US pullback recording (300 frames data) of a swine coronary artery with an artificial plaque lesion (Visualization 2).

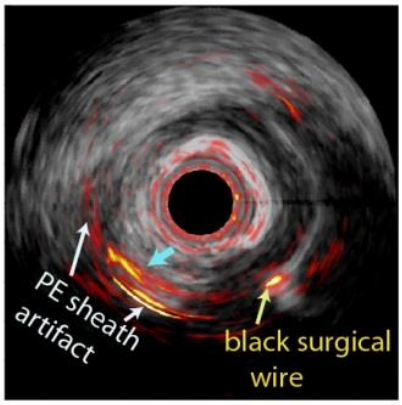

Figure 5.5. Merged cross-sectional IVPA/US image of the in vivo result on a swine coronary artery with artificial plaque lesion. White arrow indicates the PE sheath artifact, yellow arrow indicates the black surgical wire and blue arrow indicates the mixture of lipid signal and PE sheath artifact.

Fast and stable laser systems are also essential for translation of IVPA/US imaging to the clinical setting. We need to strike a balance between pulse rate (for speed), pulse energy (SNR), and overall power delivered to the vessel (safety). As 1.7 μm radiation is strongly absorbed by water, it is considered an eye-safe wavelength, which reduces concerns for user safety. We have not seen evidence of laser tissue damage in our human or swine samples, upon deposition of 150 mW of light in the artery. Nevertheless, optically and acoustically efficient designs allow for minimization of the applied laser power while preserving SNR. In recent work[36], we found that 80% of PA power from lipid-rich plaque is at frequencies below 8 MHz, and the PA SNR can be increased up to 20 dB by covering the frequency band below 8 MHz. We experienced >50% optical loss due to fiber coupling and scattering in the tip optics, which is clearly suboptimal. Improved catheter design and functionality may enable IVPA lipid imaging

with lower laser pulse energy and output power. Such moderate-output power lasers may prove to be more robust, user-friendly and affordable than the complex OPO system we currently use.

In the present series of experiments, we have chosen to clear blood from the artery for optimizing PA SNR. It is possible to image lipids through blood at 1.7 μm by IVPA imaging [16] due to the relatively small scattering coefficient at infrared wavelengths[37]. H2O absorption is significant, both in blood and in saline flush, which is why we use D2O-saline for flushing. Heavy water is non-toxic but expensive, which may present as a limitation going forward.

In summary, we demonstrated volumetric in vivo IVPA/US of lipid in the coronary circulation of a healthy swine. We built an imaging system with a miniature flexible catheter, allowing to image lipid-rich plaque lesions at 20 fps. The system produces good IVPA/US images of lipids with a PA SNR of about 20 dB at the an imaging frame rate that is compatible with comprehensive pullback imaging of coronary plaques.

Funding

Netherlands Organization for Scientific Research (NWO) ZonMW (104003006).

Acknowledgements

The authors gratefully acknowledge Mr. Keith Oakes from Elforlight Ltd. for the help with the configuration of the laser system. We acknowledge Robert Beurskens from Erasmus MC for the contribution to the development of the IVPA/US imaging system, Ms. Ilona Krabbendam-Peters and Dovile Gruzdyte from Erasmus MC for the help with the in vivo swine experiment and histology.

References

1. Yang, J.-M., et al., *Photoacoustic endoscopy.* Opt. Lett., 2009. **34**(10): p. 1591-1593.
2. Falk, E., P.K. Shah, and V. Fuster, *Coronary Plaque Disruption.* Circulation, 1995. **92**(3): p. 657-671.
3. Schaar, J.A., et al., *Terminology for high-risk and vulnerable coronary artery plaques.* European Heart Journal, 2004. **25**(12): p. 1077-1082.
4. Schaar, J.A., et al., *Intravascular palpography for vulnerable plaque assessment.* J Am Coll Cardiol, 2006. **47**(8 Suppl): p. C86-91.
5. van Soest, G., A.F. van der Steen, and E. Regar, *Autofluorescence: A New NIR on the Block⁎.* JACC: Cardiovascular Imaging, 2016.
6. Tearney, G.J., et al., *Consensus Standards for Acquisition, Measurement, and Reporting of Intravascular Optical Coherence Tomography Studies: A Report From the International Working Group for Intravascular Optical Coherence Tomography Standardization and Validation.* Journal of the American College of Cardiology, 2012. **59**(12): p. 1058-1072.
7. Manfrini, O., et al., *Sources of error and interpretation of plaque morphology by optical coherence tomography.* Am J Cardiol, 2006. **98**(2): p. 156-159.
8. Bourantas, C.V., et al., *Hybrid intravascular imaging: recent advances, technical considerations, and current applications in the study of plaque pathophysiology.* European Heart Journal, 2016: p. ehw097.

9. van Soest, G., E. Regar, and A.F. van der Steen, *Photonics in cardiovascular medicine.* Nature photonics, 2015. **9**(10): p. 626-629.
10. Choudhury, R.P., V. Fuster, and Z.A. Fayad, *Molecular, cellular and functional imaging of atherothrombosis.* Nature Reviews Drug Discovery, 2004. **3**(11): p. 913-925.
11. Garg, S., et al., *First use in patients of a combined near infra-red spectroscopy and intra-vascular ultrasound catheter to identify composition and structure of coronary plaque.* EuroIntervention, 2010. **5**(6): p. 755-756.
12. Jansen, K., et al., *Lipid detection in atherosclerotic human coronaries by spectroscopic intravascular photoacoustic imaging.* Optics Express, 2013. **21**(18): p. 21472-21484.
13. Wu, M., et al., *Intravascular Photoacoustic Imaging Of Vulnerable Atherosclerotic Plaque.* interventional Cardiology Review, 2016. **11**(2): p. 120-123.
14. Wang, B., et al., *In vivo Intravascular Ultrasound-guided Photoacoustic Imaging of Lipid in Plaques Using an Animal Model of Atherosclerosis.* Ultrasound in medicine & biology, 2012.
15. Wang, P., J.R. Rajian, and J.-X. Cheng, *Spectroscopic imaging of deep tissue through photoacoustic detection of molecular vibration.* The journal of physical chemistry letters, 2013. **4**(13): p. 2177-2185.
16. Wang, B., et al., *Intravascular photoacoustic imaging of lipid in atherosclerotic plaques in the presence of luminal blood.* Opt Lett, 2012. **37**(7): p. 1244-6.
17. Wang, B., et al., *Detection of lipid in atherosclerotic vessels using ultrasound-guided spectroscopic intravascular photoacoustic imaging.* Optics Express, 2010. **18**(5): p. 4889-4897.
18. Jansen, K., et al., *Photoacoustic imaging of human coronary atherosclerosis in two spectral bands.* Photoacoustics, 2014. **2**(1): p. 12-20.
19. Jansen, K., et al., *Spectroscopic intravascular photoacoustic imaging of lipids in atherosclerosis.* Journal of Biomedical Optics, 2014. **19**(2): p. 026006-026006.
20. Wu, M., et al., *Specific imaging of atherosclerotic plaque lipids with two-wavelength intravascular photoacoustics.* Biomedical Optics Express, 2015. **6**(9): p. 3276-3286.
21. Wang, P., et al., *High-speed Intravascular Photoacoustic Imaging of Lipid-laden Atherosclerotic Plaque Enabled by a 2-kHz Barium Nitrite Raman Laser.* Scientific reports, 2014. **4**.
22. Hui, J., et al., *High-speed intravascular photoacoustic imaging at 1.7 μm with a KTP-based OPO.* Biomedical Optics Express, 2015. **6**(11): p. 4557-4566.
23. Piao, Z., et al., *High speed intravascular photoacoustic imaging with fast optical parametric oscillator laser at 1.7 μm.* Applied physics letters, 2015. **107**(8): p. 083701.
24. VanderLaan, D., et al., *Real-Time Intravascular Ultrasound and Photoacoustic Imaging.* IEEE Transactions on Ultrasonics, Ferroelectrics, and Frequency Control, 2016. **PP**(99): p. 1-1.
25. Li, J., et al., *Ultrafast optical-ultrasonic system and miniaturized catheter for imaging and characterizing atherosclerotic plaques in vivo.* Scientific reports, 2015. **5**.
26. Rathod, K.S., et al., *Intravascular Ultrasound Versus Optical Coherence Tomography For Coronary Artery Imaging–Apples And Oranges.* Interventional Cardiology Review, 2015. **10**: p. 8-15.
27. Wu, M., et al., *Impact of device geometry on the imaging characteristics of an intravascular photoacoustic catheter.* Applied Optics, 2014. **53**(34): p. 8131-8139.
28. Leung, K.Y.E., et al., *Motion compensation for intravascular ultrasound palpography.* Ieee Transactions on Ultrasonics Ferroelectrics and Frequency Control, 2006. **53**(7): p. 1269-80.

29. van der Giessen, W.J., et al., *Lowering the dose of sirolimus, released from a nonpolymeric hydroxyapatite coated coronary stent, reduces signs of delayed healing.* JACC: Cardiovascular Interventions, 2009. **2**(4): p. 284-290.
30. Garber, J.C., et al., *Guide for the care and use of laboratory animals.* The National Academic Press, Washington DC, 2011. **8**: p. 220.
31. Matija Lovrak, et al., *Implantable artificial plaque as an alternative to atherosclerotic animal models to study stent based drug delivery and other transport phenomena in atherosclerotic plaque.* in preparation.
32. Li, Y., et al., *High-speed intravascular spectroscopic photoacoustic imaging at 1000 A-lines per second with a 0.9-mm diameter catheter.* Journal Of Biomedical Optics, 2015. **20**(6): p. 065006-065006.
33. Bai, X., et al., *Intravascular Optical-Resolution Photoacoustic Tomography with a 1.1 mm Diameter Catheter.* PLoS ONE, 2014. **9**(3): p. e92463.
34. Cao, Y., et al., *High-sensitivity intravascular photoacoustic imaging of lipid–laden plaque with a collinear catheter design.* Scientific reports, 2016. **6**: p. 25236.
35. Yabumoto, H., et al., *Perfluoropolymer waveguide with low loss in wide wavelength range.* Reports of the Research Laboratory, Asahi Glass, 2004. **54**: p. 49-52.
36. Daeichin, V., et al., *Frequency Analysis of the Photoacoustic Signal Generated by Coronary Atherosclerotic Plaque.* Ultrasound in medicine & biology, 2016.
37. Horton, N.G., et al., *In vivo three-photon microscopy of subcortical structures within an intact mouse brain.* Nat Photon, 2013. **7**(3): p. 205-209.

Chapter 6. General Conclusion

As coronary artery disease (CAD) is one of the leading causes of worldwide death, and brings substantial health care and economic burden to the society, intensive research effort has focused on it. The first clinical manifestation of CAD is commonly acute coronary syndrome (ACS) which is most often triggered by the rupture of the vulnerable atherosclerotic plaque and thrombosis [1-3]. A vulnerable plaque is generally represented as a lipid-rich necrotic core, covered by a thin fibrous cap with macrophage infiltration [4]. The knowledge of these features of the plaque is very important to characterize the vulnerability of the plaque, and thus is very helpful for guiding the diagnosis and treatment of CAD.

Intravascular photoacoustic (IVPA) imaging, generating an acoustic signal by specific optical absorption of the tissue, can image different tissue types with a good resolution (~50 μm) and reasonable imaging depth based on optical absorption contrast in coronary artery wall [5-7]. By working at different optical wavelengths for different absorption targets, IVPA imaging is capable of detection of many compositions present in a vulnerable plaque [8-10], with a primary focus on IVPA imaging of the lipid-rich core [11, 12]. A co-registered IVUS image offering full visualization of the artery wall structure is born with IVPA imaging by sharing the same ultrasound transducer. The combined IVPA/US imaging is able to image the atherosclerotic vulnerable plaque, morphologically and compositionally [13], making it a useful tool for assessment of the risk of the plaque lesion.

The complexity of the design and fabrication of the imaging catheter, and the slow imaging speed have impeded the translation of IVPA imaging to a clinical setting to date. In the recent years, research efforts have been directed towards the realization of a clinically feasible IVPA imaging system. We have achieved several essential steps on the way of translation of IVPA imaging to clinics: the miniature flexible catheter, high-efficiency specific imaging of vulnerable plaque composition, and a real-time IVPA imaging system (~ 20 frames per second). This chapter discusses an overview of our work and some remaining challenges on the development of IVPA imaging.

6.1 Achieved steps towards clinical IVPA/US imaging system

6.1.1 Steps towards a miniature IVPA catheter

A practical, functional IVPA/US catheter requires miniaturization to a size of less than 1 mm and high sensitivity for PA detection. Several layouts of the optical and acoustic channels of the catheter are possible, and have been characterized in literature by different research groups. A catheter design with a longitudinal offset between the optical and the ultrasound beams, which is used in the smallest IVPA catheter (diameter is 0.9 mm) reported so far [14], appears to be the best candidate for miniaturization. Based on this catheter design, we fabricated a flexible IVPA/US catheter with an outer diameter of about 1.3 mm, which is capable of lipid imaging in coronary arteries ex vivo and in vivo. A comprehensive characterization of the imaging property of the catheter is important for interpreting the received images. The spatial resolution of the catheter was quantified by a measurement on isolated targets. With our catheter, the PA and US axial resolutions are 52 and 43 μm, the lateral (azimuthal) resolutions are 215 and 205 μm, while the longitudinal (in the pullback direction) resolutions are 500 and 205 μm, respectively. The geometry configuration in our catheter presents a curved PA point

spread function in space, resulting in a mismatch between PA and US imaging plane. This mismatch is reduced in the presence of optical scattering, which is natural in tissue (Chapter 2).

6.1.2 Steps towards specific plaque lipids identification by IVPA imaging

To visualize the lipid deposits in atheromatous plaque, IVPA imaging generally works at the wavelength where lipids are the most highly absorbing tissue components. The optical absorption spectrum of lipids is shown in fig. 1(a). Generally, 1.2 or 1.7 μm are the best and most commonly used optical wavelengths for imaging lipids, although the possibility of IVPA imaging of lipids at 760 or 1064 nm has been explored [15, 16]. Compared to the other reported wavelengths for lipid imaging in coronary arteries, 1.7 μm has several advantages: it has a higher lipid-specific optical absorption and lower attenuation through biological tissue (fig. 6.1(b)) [17]; because of strong water absorption at this wavelength, it is considered eye-safe, which takes care of a major user safety concern. Fig. 6.1(c) shows the PA absorption spectra of lipid in water. Normalized the PA spectra amplitude of lipid to the one measured at the water interface (no water path), through about 3 mm water path, which is deep enough for imaging coronary arteries, the PA SNR of lipid at 1.7 μm is about 5 dB higher than imaging at 1.2 μm [18, 19].

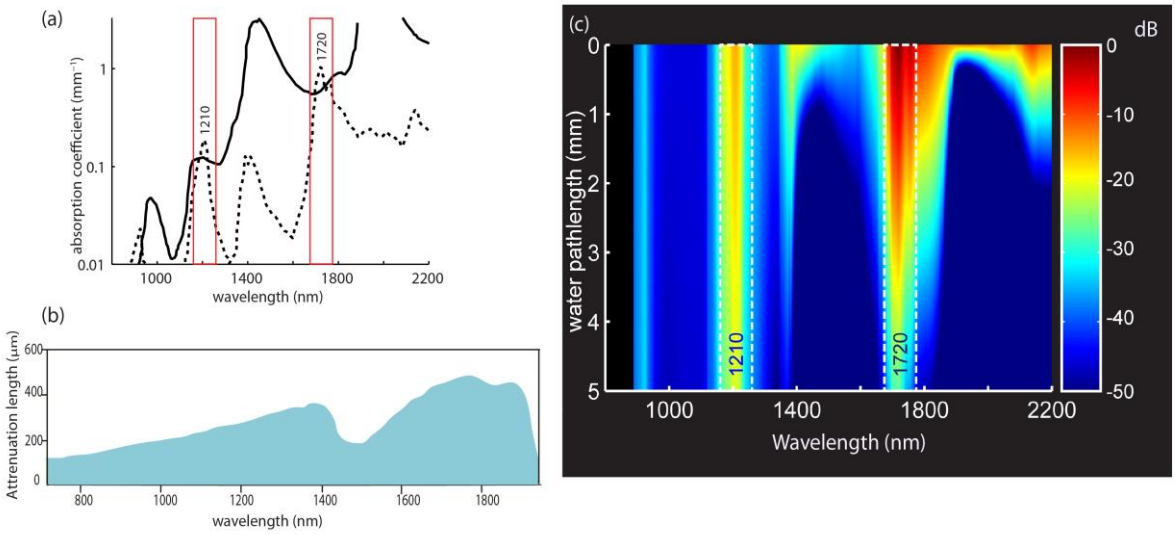

Figure 6.2. (a) Lipid absorption spectrum. The absorption spectra of water (solid line) and human fat (dotted line), with red dashed boxes indicating the two absorption peak for lipids. Adapted from [20]. (b) Attenuation length of brain tissue, showing the dominant contributions of tissue scattering in the visible/NIR region (up to approx. 1.3 μm), and of water absorption at longer wavelengths. Adapted from [17]. (c) The absorption spectra of lipid through different water path.

Typically, lipids are found in the plaque inside the artery wall (rich in cholesterol and cholesteryl esters [21, 22]), as well as in peri-adventitial fat tissue around the artery (a mixture of fatty acids [23]). These different lipids present different PA spectra, and can be differentiated by spectroscopic IVPA imaging (sIVPA)[24, 25]. However, sIVPA imaging requires many wavelengths and makes the imaging system complicated and costly. To solve this problem, we developed a new algorithm to detect and differentiate between plaque lipids and peri-adventitial fat with two wavelengths only, specifically 1718 and 1734 nm. Statistically, we

identify 70% of lipids in plaques, and 15% in the peri-adventitia tissue as cholesterol-like lipids. The latter number represents actual false positives. The former score is defined as a true positive detection and may be underestimated by the variability of plaque lipid composition: Plaques also contain fatty acid-like lipids (e.g. triglycerides and phosphatidylcholines). With this method, the presence and location of lipids within a plaque can be reliably and quickly displayed during a catheter pullback recording. Importantly, the specific information based on the spectral analysis is rapidly available without the need of tedious examination of the IVUS information. However, the recalibration of the threshold parameter is required when adapted the algorithm to different IVPA/US imaging systems (Chapter 3).

6.1.3 Steps towards a fast and safe IVPA/US imaging system

As a powerful tool to image lipid-rich vulnerable plaques, the further development of IVPA imaging severely suffers from its low imaging speed mainly due to the slow laser system. With the introduction of the fast lasers with 500 Hz to 2 kHz pulse-rate, many fast IVPA imaging system are on horizon [14, 26-28]. Although the imaging speed of IVPA imaging system for lipid imaging has been increased to 1 frame per second [27, 28], it is still too slow and restricts the application of IVPA/US imaging to the laboratory setting only. If taking clinically available IVUS system as a reference (IVUS system scans a vessel with a pullback speed of 0.5-1 mm/s at a frame rate of at least 20 fps [29]), an IVPA/US imaging system suitable for clinical applications requires a minimal frame rate of 20 fps. To reach 20 fps with a minimal 150 A-scan per cross-sectional acquisition (our catheter has an angular resolution about 5 degree, with a minimal 50% angular overlap between adjacent A scan, it requires more than $360/5*0.5=144$ A-scan per cross-sectional acquisition), a laser system with a pulse rate of at least 3000 (20*150) Hz is necessary.

We developed a real-time IVPA/US imaging system based on a 5 kHz OPO laser system (tuning range: 1700 to 1750 nm, pulse energy: maximal 80 µJ/pulse) and a flexible 1.3 mm imaging catheter. This IVPA/US imaging system is capable of imaging at 20 fps (250 A-scan per cross section), which is 20 times faster in terms of frame rate than any other imaging system, reaching the minimum acceptable imaging speed of commercially available IVUS systems, as routinely used in clinics for intracoronary imaging. The capability of the IVPA/US imaging system was first validated by the high accordance of the ex vivo result on an atherosclerotic human coronary artery to the gold standard histology staining. Encouraged by the success in the ex vivo experiment, we achieved the first in vivo IVPA/US imaging of coronary arteries on a healthy swine with an artificial plaque lesion.

In both the *ex vivo* and *in vivo* experiments, the real-time IVPA/US imaging system achieved a PA signal from the lipid deposition in coronary arteries with a SNR around 20dB based on the laser source with a high repetition rate but moderate pulse energy, which is about 10 times lower than the other imaging systems [27]. Due to ineffective coupling and scattering at the catheter tip, the optical exposure is less than 0.4 J/cm^2 at 1.7 µm, which is below the 1 J/cm^2 limit specified by the ANSI laser safety standard [28, 30]. In all the measurements, we have not seen any evidence of laser tissue damage in our human or swine samples, upon deposition

of 150 mW of light in the artery. These results demonstrate the capability of the IVPA/US imaging system for in vivo application (Chapter 5).

As argued above, faster imaging or more wavelengths can only be achieved by raising the laser system's pulse rate. The average power increases linearly with pulse frequency. With further increase of the laser repetition rate (> 10 kHz) while maintaining a reasonable pulse energy for high PA SNR (> tens μJ/pulse out of catheter), the average power delivered to the artery for IVPA imaging is quickly running into power management and safety concerns As one possible solution for that, it is important to match the transducer frequency bandwidth to the frequency response of PA signal generated from the plaque. Based on analysis of in vitro IVPA data from several atherosclerotic human coronary artery specimens, we found that that 80% of the PA power generated from plaque lipids lies in the frequency band below 8 MHz. The PA SNR can be increased by an order of magnitude by covering the low frequency range. The finding may enable the possibility of IVPA imaging based on fast laser sources with a moderate output power (Chapter 4).

6.2 Future works towards clinical IVPA/US imaging system

Although our current IVPA/US imaging system is capable of in vivo plaque lesion analysis, many challenges clearly remain for the further development of IVPA/US imaging. An ideal IVPA/US imaging system would consist of a highly sensitive imaging catheter with a maximum outer diameter of 1 mm, the robust, compact, fast laser system working at two different wavelengths for plaque lipid specific imaging, and a software interface capable of rapid visualization of the presence and location of lipid-rich plaque during the pullback data acquisition. The imaging system would allow for plaque imaging at a frame rate of at least 20 fps with a safe optical output power (below the threshold of $1 J/cm^2$ at 1.7 μm)

6.2.1 Catheter design

Based on the longitudinal dual beam offset design, the current prototype of flexible IVPA/US imaging catheter is 1.3 mm in outer diameter. The size of the catheter can be further reduced to around 1.0 mm by replacing with a smaller metal torque coil and outer sheath. However, this catheter design has a poor PA sensitivity with imaging targets close by the catheter. A collinear IVPA/US catheter design is proposed recently to overcome this limitation[31]. The design optimizes the imaging sensitivity and imaging depth with a highly overlapped dual beam path, but it is more prone to image the artifacts resulting from near-field optical absorption, such as the artifacts from the catheter sheath. Especially the catheter outer sheath is currently one of the biggest challenges for IVPA/US imaging. The sheath material needs to be transparent for both ultrasound and light (1.7 μm), as well as be strong enough to support the catheter inside the coronary arteries. In current prototype catheter, a PE sheath is used, which has adequate ultrasonic properties but attenuates the excitation light, leading to a reduction in PA SNR and strong reflection artifacts. Amorphous fluorinated polymers, such as perfluoro-3-butenyl-vinyl ether (CyTop^{TM}), which is flexible and has a 95 % transmittance of the light at 1.7 μm [32], may be a promising choice as the catheter sheath.

As mentioned before, to increase the sensitivity of IVPA imaging of plaque lipids, a transducer covering the low frequency bandwidth (below 8 MHz) should be applied. On the other hand,

for a high-resolution IVUS imaging of the artery structure, a high frequency (higher than 20 MHz) transducer is normally used in the IVPA/US system. To take both the advantages of high PA sensitivity for IVPA imaging of plaque and high resolution for IVUS imaging of artery wall, an IVPA/US catheter with a dual-element transducer would be an ideal design. Lately, a small broadband polyvinylidene difluoride (PVDF) transducer (frequency bandwidth of 2 to 15 MHz and size of 0.6 × 0.6 mm) with integrated electronics transducer for IVPA imaging was developed [33]. It can be potentially integrated into currently available IVPA/US catheter for IVPA imaging with more investigation.

Another possible improvement in our catheter design is to improve the efficiency of light delivery for IVPA imaging. In our current catheter, an angle polished fiber covered by a quartz cap (at an angle of 37 degree) was used for delivering light to the artery wall, and only about 40% of the light was delivered out of the fiber. Alternatively, according to our test in the lab, a combination of a common multimode fiber and a right angle prism (5 mm leg length) coated with the protective silver or gold layer achieved almost 90% of the light delivery. However, making the prism small enough to integrate into the miniature IVPA catheter is a challenge.

6.2.2 Imaging speed

As most of IVPA/US imaging systems, our current imaging system also requires saline flushing for plaque imaging in coronary arteries for a better PA SNR. Especially, when imaging at 1.7 μm, we used D_2O-saline for flushing due to the much lower attenuation of light through D_2O. Although D_2O is non-toxic, it is quite expensive, and can be a limitation for the application of IVPA imaging in the future. Moreover, to mitigate risks that may be introduced by the disruption to blood flow in the artery, the duration of flushing is limited to only a few seconds, leading to a limited volume of artery that can be safely imaged [34]. With a pullback speed of 0.5 mm/s and continuously saline flushing of maximal 10 s, a maximal 5 mm vessel can be safely scanned for one pullback, which is relatively short in practical application. To increase the pullback length, a higher pullback speed is recommended. A higher pullback speed generally brings in a larger error in longitudinal measurements due to a wider frame pitch (pullback speed/frame rate). In consequence, the frame rate should be increased as well. The ideal frame rate of IVPA imaging is limited to the highest frame rate of IVUS imaging (around 100 fps) and it is not possible to increase the frame rate of IVPA imaging freely. The increase of the frame rate requires a laser source with a higher pulse rate, which presents as the biggest limitation for IVPA imaging at this moment: there is a tradeoff between the high pulse rate for high imaging speed and the high pulse energy for high PA SNR, due to the limited optical power allowed for tissue imaging and the physical limitations of the laser system. In this case, IVPA/US imaging without flushing would be ideal. Principally, it is possible for IVPA imaging through the blood at 1.7 μm, which has been achieved in rabbit model *ex vivo* [35]. In the system, very high optical pulse energy is used (1.05 mJ/pulse from the catheter tip), which is not practical to use. In terms of IVPA/US imaging in the presence of blood with a reasonable laser pulse energy (tens of μJ/pulse), efforts must be taken to optimize the PA sensitivity, light delivery and data processing of the imaging system.

6.2.3 Other issues

Other challenges for adapting to the clinical setting, including the cost, robustness, compactness and high repetition rate (of the order of 10 kHz) of the laser sources are the topics of ongoing research. A new IVPA/US imaging system based on a continuous wave (CW) laser instead of a bulky, expensive pulsed laser proposed recently [36] provides another interesting alternative.

6.2.4 Combination with other imaging modalities

To capture more presentative features of a vulnerable plaque for a better assessment of the plaque lesion, combined imaging modality is a promising approach and may be a future trend for intravascular imaging. The combinations of IVUS and NIRS [37], IVUS and IVOCT [38], IVOCT and NIRF [39] has been proposed for a better characterization of the vulnerable plaque. Superior to NIRS/IVUS, which offers both full visualization of artery wall structure and the presence of lipid-rich plaque, IVPA/US imaging shows the lipid-rich plaque with detailed depth and volume information. It provides the location of the lipid core related to the lumen which is not available in NIRS imaging, and this location information can be critical for making the decision of the stenting region in percutaneous coronary intervention (PCI). As a plaque close to the lumen, even with a relatively small volume, we may still consider to include it into the stent coverage region for a better long-term outcome. Neither the combination of IVUS and IVOCT nor IVOCT and NIRF can offer the direct, validated visualization of coronary plaque lipid of IVPA imaging. To many clinicians, the ideal tool for guiding the atherosclerotic plaque diagnosis and interventions comprehends high resolution for thin cap thickness characterization, high sensitivity to detect lipids for plaque visualization in artery and reasonable penetration depth for plaque burden assessment. For that, the combination of IVOCT and IVPA would be a very promising choice at the cost of integrating an extra OCT laser system.

References

1. Falk, E., P.K. Shah, and V. Fuster, *Coronary Plaque Disruption.* Circulation, 1995. **92**(3): p. 657-671.
2. Bourantas, C.V., et al., *Hybrid intravascular imaging: current applications and prospective potential in the study of coronary atherosclerosis.* Journal of the American College Of Cardiology, 2013. **61**(13): p. 1369-1378.
3. Batty, J.A., et al., *Intracoronary Imaging in the Detection of Vulnerable Plaques.* Current cardiology reports, 2016. **18**(3): p. 1-12.
4. Schaar, J.A., et al., *Terminology for high-risk and vulnerable coronary artery plaques.* European Heart Journal, 2004. **25**(12): p. 1077-1082.
5. Jansen, K., G. van Soest, and A.F.W. van der Steen, *Intravascular Photoacoustic Imaging: A New Tool for Vulnerable Plaque Identification.* Ultrasound in medicine & biology, 2014. **40**(6): p. 1037-1048.
6. Schoenhagen, P. and D.G. Vince, *Intravascular Photoacoustic Tomography of Coronary AtherosclerosisRiding the Waves of Light and Sound⁎.* Journal of the American College of Cardiology, 2014. **64**(4): p. 391-393.
7. Jansen, K., et al., *Photoacoustic imaging of human coronary atherosclerosis in two spectral bands.* Photoacoustics, 2014. **2**(1): p. 12-20.

8. Wu, C., et al., *A novel photoacoustic nanoprobe of ICG@ PEG-Ag 2 S for atherosclerosis targeting and imaging in vivo.* Nanoscale, 2016.
9. Wang, B., et al., *Plasmonic Intravascular Photoacoustic Imaging for Detection of Macrophages in Atherosclerotic Plaques.* Nano Letters, 2008. **9**(6): p. 2212-2217.
10. Wu, M., et al., *Intravascular Photoacoustic Imaging Of Vulnerable Atherosclerotic Plaque.* interventional Cardiology Review, 2016. **11**(2): p. 120-123.
11. Allen, T.J., et al., *Spectroscopic photoacoustic imaging of lipid-rich plaques in the human aorta in the 740 to 1400 nm wavelength range.* Journal of Biomedical Optics, 2012. **17**(6): p. 061209-10.
12. Jansen, K., et al., *Intravascular photoacoustic imaging of human coronary atherosclerosis.* Opt Lett, 2011. **36**(5): p. 597-9.
13. Wang, B., et al., *Intravascular Photoacoustic Imaging.* Ieee Journal of Selected Topics in Quantum Electronics, 2010. **16**(3): p. 588-599.
14. Li, Y., et al., *High-speed intravascular spectroscopic photoacoustic imaging at 1000 A-lines per second with a 0.9-mm diameter catheter.* Journal of Biomedical Optics, 2015. **20**(6): p. 065006-065006.
15. Zhang, J., et al., *Characterization of lipid-rich aortic plaques by intravascular photoacoustic tomography: ex vivo and in vivo validation in a rabbit atherosclerosis model with histologic correlation.* Journal of the American College Of Cardiology, 2014. **64**(4): p. 385-390.
16. Choi, C., et al. *Fast integrated intravascular photoacoustic/ultrasound catheter*. in *SPIE BiOS*. 2016. International Society for Optics and Photonics.
17. Horton, N.G., et al., *In vivo three-photon microscopy of subcortical structures within an intact mouse brain.* Nature photonics, 2013. **7**(3): p. 205-209.
18. Wang, P., et al., *Bond-selective imaging of deep tissue through the optical window between 1600 and 1850 nm.* Journal of biophotonics, 2012. **5**(1): p. 25-32.
19. Wang, P., J.R. Rajian, and J.-X. Cheng, *Spectroscopic imaging of deep tissue through photoacoustic detection of molecular vibration.* The journal of physical chemistry letters, 2013. **4**(13): p. 2177-2185.
20. Anderson, R.R., et al., *Selective photothermolysis of lipid-rich tissues: A free electron laser study.* Lasers in Surgery and Medicine, 2006. **38**(10): p. 913-919.
21. Lundberg, B., *Chemical-Composition and Physical State of Lipid Deposits in Atherosclerosis.* Atherosclerosis, 1985. **56**(1): p. 93-110.
22. Stegemann, C., et al., *Comparative Lipidomics Profiling of Human Atherosclerotic Plaques / Clinical Perspective.* Circulation: Cardiovascular Genetics, 2011. **4**(3): p. 232-242.
23. Tsai, C.L., J.C. Chen, and W.J. Wang, *Near-infrared absorption property of biological soft tissue constituents.* J Med Biol Eng, 2001. **21**(1): p. 7-14.
24. Jansen, K., et al., *Spectroscopic intravascular photoacoustic imaging of lipids in atherosclerosis.* Journal of Biomedical Optics, 2014. **19**(2): p. 026006-026006.
25. Jansen, K., et al., *Lipid detection in atherosclerotic human coronaries by spectroscopic intravascular photoacoustic imaging.* Optics Express, 2013. **21**(18): p. 21472-21484.
26. Wang, P., et al., *High-speed Intravascular Photoacoustic Imaging of Lipid-laden Atherosclerotic Plaque Enabled by a 2-kHz Barium Nitrite Raman Laser.* Scientific reports, 2014. **4**.
27. Piao, Z., et al., *High speed intravascular photoacoustic imaging with fast optical parametric oscillator laser at 1.7 μm.* Applied physics letters, 2015. **107**(8): p. 083701.
28. Hui, J., et al., *High-speed intravascular photoacoustic imaging at 1.7 μm with a KTP-based OPO.* Biomedical Optics Express, 2015. **6**(11): p. 4557-4566.

29. Li, J. and Z. Chen, *Integrated intravascular ultrasound and optical coherence tomography technology: a promising tool to identify vulnerable plaques [INVITED PAPER]*. Journal of Biomedical Photonics & Engineering, 2016. **1**(4): p. 209-224.
30. *American National Standards for Safe Use of Lasers, ANSI Z136.1*. 2014.
31. Cao, Y., et al., *High-sensitivity intravascular photoacoustic imaging of lipid–laden plaque with a collinear catheter design.* Scientific reports, 2016. **6**: p. 25236.
32. Yabumoto, H., et al., *Perfluoropolymer waveguide with low loss in wide wavelength range.* Reports of the Research Laboratory, Asahi Glass, 2004. **54**: p. 49-52.
33. Daeichin, V., et al., *A Broadband Polyvinylidene Difluoride-Based Hydrophone with Integrated Readout Circuit for Intravascular Photoacoustic Imaging.* Ultrasound in medicine & biology, 2016. **42**(5): p. 1239-1243.
34. Suter, M.J., et al., *Optimizing flushing parameters in intracoronary optical coherence tomography: an in vivo swine study.* The International Journal of Cardiovascular Imaging, 2015. **31**(6): p. 1097-1106.
35. Wang, B., et al., *Intravascular photoacoustic imaging of lipid in atherosclerotic plaques in the presence of luminal blood.* Opt Lett, 2012. **37**(7): p. 1244-6.
36. Castelino, R.F., et al., *Combined frequency domain photoacoustic and ultrasound imaging for intravascular applications.* Biomedical Optics Express, 2016. **7**(11): p. 4441-4449.
37. Garg, S., et al., *First use in patients of a combined near infra-red spectroscopy and intra-vascular ultrasound catheter to identify composition and structure of coronary plaque.* EuroIntervention, 2010. **5**(6): p. 755-756.
38. Li, J., et al., *Ultrafast optical-ultrasonic system and miniaturized catheter for imaging and characterizing atherosclerotic plaques in vivo.* Scientific reports, 2015. **5**.
39. Yoo, H., et al., *Intra-arterial catheter for simultaneous microstructural and molecular imaging in vivo.* Nature medicine, 2011. **17**(12): p. 1680-1684.

Summary

The rupture of vulnerable atherosclerotic plaque is the most frequent cause of acute cardiovascular events and sudden cardiac deaths. The identification of the vulnerable plaque, which is believed to be related to the structure and composition of the plaque, can greatly benefit the management of the cardiovascular disease in clinics. A vulnerable plaque is usually described as a lipid-rich necrotic core, covered by a thin fibrous cap with macrophage infiltration. These common features of the vulnerable plaque can be useful markers for the detection of the vulnerable plaque by intravascular imaging techniques. Intravascular photoacoustic (IVPA) imaging can characterize the composition of the plaque based on the optical contrast between different tissue types, which can be easily applied by performing IVPA imaging at different wavelengths for different imaging targets. Combined IVPA/US imaging shows great potentials to image the vulnerable atherosclerotic plaque, morphologically (co-registered IVUS image) and compositionally (especially lipid-rich plaque), and is becoming a powerful tool to guide the assessment and treatment of the atherosclerotic plaque lesions.

The aim of this thesis is to develop a prototype of fast IVPA/US imaging system capable of performing in vivo experiments on swine model, accelerating the translation of IVPA/US imaging toward clinical application.

A sensitive, miniature and flexible IVPA/US imaging catheter is critical for the imaging system. **In chapter 2**, we fabricated an imaging catheter with a longitudinal dual beam offset. We characterized the imaging property of the catheter in terms of spatial shape of the PSF for IVPA imaging in clear and optically scattering media. We showed that the product of the two beam profiles can accurately model the measured peak response in clear and scattering media. We found that the dual beam offset leads to a curved PSF, making a mismatch between IVPA and IVUS imaging planes. Introduction of optical scattering can reduce this mismatch.

A suitable and effective application of wavelength for IVPA imaging of vulnerable plaque (lipid-rich plaque) plays an important role as well. Typically, lipids can be found in the plaque inside the artery wall (plaque lipids), as well as in peri-adventitial fat tissue around the artery (peri-adventitial lipids), that is present also in normal coronary arteries. **In chapter 3**, we developed an algorithm to detect and differentiate between these two kinds of lipids based on the relative difference of the PA signal at 2 wavelengths (1718 and 1734 nm). It achieved about 70% true positive and 15% false positive identification of plaque lipids in ex vivo human atherosclerotic coronary samples. It is possible to be adapted to a different imaging system platform by a recalibration of threshold parameter.

The optimization of PA sensitivity for IVPA imaging of lipid-rich plaque is another significant factor. **In chapter 4**, we investigated ex vivo PA data collected from 35 human atherosclerotic plaque lesions and found that majority (80%) of the PA signal power generated from the coronary plaque lesions lies in the frequency band below 8 MHz. A match of frequency response of the receiving transducer to the low frequency range, below 8 MHz can increase the

PA sensitivity of imaging plaque lipid by about 20dB. Our finding makes it possible for IVPA imaging of plaque lesions with low laser pulse energy.

Finally, **in chapter 5**, we achieved a fast IVPA/US imaging system with a 1.3 mm flexible catheter ready for the in vivo application. The imaging system is based on a 5 kHz pulse rate OPO laser and allows for IVPA/US imaging at 20 fps, which is 20 times faster than other reported systems so far. The capability of the imaging system is validated by a successful ex vivo experiment on a human atherosclerotic coronary artery. With this system, we achieved the first in vivo IVPA imaging of intracoronary lipid in a swine model with a PA SNR of about 20 dB. The system operated at 20 fps and 0.1~1 mm/s pullback speed, which is comparable to the commercial IVUS imaging system routinely used in clinical practice. It represents a big step towards a clinical IVPA/US imaging system, although a lot of future work remains, particularly in the optimization of the catheter.

Samenvatting

Het scheuren van kwetsbare atherosclerotische plaques is de meest voorkomende oorzaak van hartinfarcten. Het herkennen van kwetsbare plaques, kwestbaarheid is gerelateerd aan de structuur en de compositie van de plaques, is belangrijk voor de behandeling van hart- en vaatziekten. Een kwetsbare plaque wordt gekenmerkt door een necrotische kern met vetten, omhuld door een dunne fibreuze kap geïnfiltreerd door macrofagen. Deze vaak voorkomende kenmerken van kwetsbare plaques kunnen worden gebruikt voor de detectie hiervan met behulp van intravasculaire foto akoestische beeldvormingstechnieken (IPVA). Intravasculaire fotoakoestiek beeldvorming kan gebruikt worden om de samenstelling van de plaque vinden door middel van optisch contrast tussen verschillende weefsels. Dit kan gemakkelijk worden gedaan door IVPA uit te voeren bij verschillende golflengtes van licht voor verschillende weefsels. Gecombineerde IVPA en ultrageluid(US) beeldvorming is een veelbelovende techniek voor het in beeld brengen van kwetsbare plaques, wat betreft morfologie (co-geregistreerde IVUS beeld) en samenstelling (specifiek vet rijke plaques). Daarmee is deze techniek is een belangrijk middel voor het diagnosticeren en behandelen van atherosclerotische plaques.

Het doel van dit onderzoek is het ontwikkelen van een prototype voor een snel IVPA/US beeldvormingssyteem, wat in staat is in vivo experimenten uit te voeren op een varkensmodel, en daarmee een versnelling veroorzaken in het vertalen van deze techniek van een onderzoek setting naar een klinische toepassing.

Een gevoelige, kleine en flexibele IVPA/US katheter is essentieel voor het beeldvormingssyteem. **In hoofdstuk 2** hebben we een beeldvormingskatheter ontwikkeld waarbij de optische en akoestische bundels longitudinaal ten opzichte van elkaar geplaatst zijn.We hebben de beeldvormingseigenschappen van de katheter gekarakteriseerd wat betreft spatiele vorm van de PSF voor IVPA in een helder en optisch verstrooiend medium. We hebben aangetoond dat het product van de twee bundel profielen een nauwkeurig model is van de gemeten maximale respons in een helder en optisch verstrooiend medium. We hebben gevonden dat de duo bundel offset leidt tot een gebogen PSF, wat resulteert in een verkeerde overlap tussen de IVPA en IVUS beeldvlakken. Het toevoegen van optische verstrooiing kan deze foutieve overlap corrigeren.

Een geschikte en effectieve toepassing van golflengten voor IVPA beeldvorming van kwetsbare plaques (vet rijke plaques) is daarnaast ook een belangrijke factor. Vetten kunnen voornamelijk worden gevonden in de plaque, binnenin de vaatwand (plaque vetten), en daarnaast ook in peri-adventitieel vet weefsel rondom de slagader (peri-adventitiele vetten), dit laatste komt ook voor in normale kransslagaders. **In hoofdstuk 3**, hebben we een algoritme ontwikkeld voor de detectie en differentiatie tussen de twee verschillende soorten lipiden gebaseerd op het relatieve verschil tussen het foto akoestische signaal bij twee golflengtes (1718 en 1734 nm). Dit algoritme geeft 70% echt positief en 15% vals positieve identificatie

van plaque gerelateerde vetten in ex vivo humane atherosclerotische kransslagaders. Het is mogelijk om het algoritme aan te passen aan een ander beeldvormingssysteem platform door een kalibratie van de parameter drempelwaarde.

De optimalisatie van foto akoestische gevoeligheid voor IVPA beeldvorming van vet rijke plaques is een andere belangrijke factor. **In hoofdstuk 4**, hebben we gekeken naar ex vivo foto akoestische data verkregen van 35 humane atherosclerotische laesies en vonden dat het meeste (80%) foto akoestische signaal dat gegenereerd wordt in de coronaire plaque laesies een frequentie band heeft beneden 8MHz. De gevoeligheid voor het foto akoestische signaal van de plaque vetten kan worden vergroot met 20dB door de frequentierespons van de ultrageluid ontvanger te laten overlappen met de uitgezonden frequenties, lager dan 8MHz. Onze bevindingen maken het mogelijk om plaque laesies foto akoestische in beeld te brengen met lage laser puls energie.

Tot slot, **in hoofdstuk 5**, hebben we een snel IVPA/US beeldvormingssyteem ontwikkeld met een 1.3 mm flexibele katheter die in vivo gebruikt kan worden. Het systeem is gebaseerd op een 5 kHz puls snelheid OPO laser en dit zorgt voor IVPA/US beeldvorming met 20 fps, 20 keer sneller dan andere gerapporteerde systemen. The mogelijkheden van het systeem zijn gevalideerd door een succesvol ex vivo experiment op een humane atherosclerotische kransslagader. Met dit systeem hebben we ook de eerste in vivo IVPA beelden van intracoronaire vetten in een varkensmodel kunnen vastleggen, met een foto akoestische SNR van 20 dB. Het systeem functioneert bij 20 fps en 0.1~1 mm/s terugtrek snelheid, dit is vergelijkbaar met commerciële IVUS systemen die routinematig worden gebruikt in de kliniek. Dit is een grote stap richting een klinisch toepasbaar IVPA/US systeem, hoewel er nog veel werk te verzetten blijft, met name wat betreft het optimaliseren van de katheter.

Acknowledgement

There is an old Chinese saying: All good things must come to an end. After 5 years working in the BME group, it finally reaches the moment to farewell. Looking back, I have had a great time here: Very nice colleagues and friends, two lovely daughters and a PhD degree!

Ton, my promotor, thank you so much for giving me the opportunity to work in your great group and supporting me though my PhD. You are so kindhearted and thoughtful, making it a great pleasure working for you. Your wise mind and calm altitude towards solving problems give me a good lesson and would be beneficial for my lifetime. Gijs, my co-promotor, thank you so much for guiding me through in my work. Your extensive knowledge and professional skills of presentation and writing help me a lot. I am very lucky and happy to have you two as my promotors.

Krista, I am so grateful to have you as my ancestor, as well as my good friend. Thank you so much for your patient explanation for my questions even when you were busy. Thank you so much for showing me how to do the experiments hand by hand in my first year.

Geert, you are a magician in the lab. Your magical hands can make everything I asked. As I am such a person very good at killing things and thank you so much fixing them again and again for me.

Robert, thank you so much for always being there when I have problems. I will never forget your kind help when I was pregnant and sick at IUS conference in Dresden 5 years ago and your considerate company when I was frustrated by the failure of my experiments.

Fritz, thank you so much for your great help with the data acquisition software. I enjoyed very much all our discussion for the problems of the real-time IVPA imaging system. You always give me helpful ideas. So, I kept putting “hunting for Frits” in my daily schedule for quite a while. Many thanks for your time and patience.

Sophinese, Jovana and Mirjam, my dear girls in our biomedical optics office, thank you so much for your very nice company. I am the only child in my family, and the days with you girls making me feel I have three lovely sisters. Sophinese, you are so sweet and always willing to listen and help when I have problems, especially in my absence of maternity leave. I feel so lucky to have you around. Mirjam, thank you so much for your great help with my Dutch summary of my thesis. Jovana, it is very nice to have you siting behind me, your hard-working attitude set the right tone. Now, it comes the boy in the office. Tianshi, thanks for taking me out for Chinese meals when I was feeling down. Muthu, it was really fun travelling with you to the SPIE conference in USA and thank you so much for collecting human coronary artery specimens for me from the autopsy room, since I was so scared to be there. Andre and Ate, it was really a pleasure to work with you in the lab although you were only around for several months. Reza, Pieter, Martin and Leonardo, it is a great fun to have you in the office, I enjoyed a lot with you guys: full of sweets and snacks in the office and always support for each other☺.

Gracia, Rita, thank you so much for all your kind help with my purchase and reimbursement. Sharon, thank you so much for the help with the procedure of my PhD graduation. Heleen and Ilona, thank you so much for your great help with the pig experiments and histology work. Without your support, I will never have the in vivo data. Gerard and Hans, thank you for all the help for my work. Emile, thank you so much for your help with the US transducer for my project.

Rik, Klazina, Ali, Ines, Tom, Deep, Jason, Kirby, Sara, Ayla, Kim, Eline, Astrid, Ruoyu, Eric, Annette and Kristina, you are so nice to me and always help when I need. Thank you for making my PhD life in BME group colourful and joyful, although I seldom showed up in the drink and table game party thanks to my naughty daughter. I did feel the happy and relaxing atmosphere in the WhatsApp conversation.

At the end, I would like to thank my beloved family for their endless support and love. My dear papa and mama, thank you so much for always standing behind me for all my decisions. I deeply feel that the love from father stands as a huge mountain, while the love from my mother flows as a gentle stream. My parents and in laws, thank you so much for travelling aboard so often for taking care of my little girls, I know they are so naughty and give a lot of headache to you. My dear uncles and aunts, thank you so much for taking care of my parents when I was far away and keeping them from feeling lonely. My dear husband, Han and my lovely daughters, thanks so much for years of good company and support. No matter where we live, I feel home when you are there. I love all of you!

感谢我亲爱的家人, 是你们无尽的爱支持我走到今天。亲爱的爸爸，妈妈，感谢你们一直以来无条件的支持和付出。你们让我深深感受到：父爱如山，母爱似水。感谢我的父母和公婆，谢谢你们多年不辞辛劳长途奔波， 帮忙照看两个令人头疼的超级熊孩子。感谢我的姑姑，姑父，舅舅，舅妈，谢谢你们在我无法陪伴父母时候，照顾并陪伴他们，让他们免于孤单。我亲爱的夏寒以及可爱的孩子们，感谢你们的陪伴，尽管多年漂泊在外，但是有你们的地方就有家的感觉。我爱你们！

谨以此书献给所有我爱的人们！

About the author

Min Wu (吴敏) was born on January 12th, 1984 in Fujian, China. She obtained her Bachelor of Electronic Information Engineering (2006), and PhD degrees of Communication and Information System (2011) from Wuhan University, China. In 2012, she joined Thoraxcenter, Erasmus MC, University Medical Center Rotterdam to pursue her second PhD degree. Here she conducted the research described in this thesis.

Publications

1**. Min Wu,** Geert Springeling, Matija Lovrak, Fritz Mastik, Sophinese Iskander-rizk, Tianshi Wang, Heleen M. M. van Beusekom, A. F. W. van der steen, and Gijs van Soest, Real-time volumetric lipid imaging in vivo by intravascular photoacoustics at 20 frames per second. Biomedical optics express, 2017, 8(2), 943-953

2**. Min Wu,** Antonius F.W. van der Steen, Evelyn Regar, Gijs van Soest, Intravascular Photoacoustic Imaging of Vulnerable Atherosclerotic Plaque: An Emerging Technology Update, Interventional cardiology review journal, 2016;11(2):120–3

3. Daeichin V, **Wu M**, de Jong N, et al. Frequency analysis of the photoacoustic signal generated by coronary atherosclerotic plaque. *Ultrasound Med Bio* 2016;42:2017–25.

4. **Wu M**, Jansen K, van der Steen A F W, et al. Specific imaging of atherosclerotic plaque lipids with two-wavelength intravascular photoacoustics. Biomedical optics express, 2015, 6(9): 3276-3286

5. **Wu M**, Jansen K, Springeling G, et al. Impact of device geometry on the imaging characteristics of an intravascular photoacoustic catheter. Applied optics, 2014, 53(34): 8131-8139.

6. Krista Jansen; **Min Wu**; Antonius F. W. van der Steen; Gijs van Soest. Lipid detection in atherosclerotic human coronaries by spectroscopic intravascular photoacoustic imaging. Optics Express, Vol. 21, Issue 18, pp. 21472-21484 ,2013

7. Jansen, Krista and **Wu, Min** and van der Steen, Antonius FW and van Soest, Gijs; Photoacoustic imaging of human coronary atherosclerosis in two spectral bands, Photoacoustics, volume 2, no. 1, page 12-20, 2014

8.Jansen K, van der Steen A F W, **Wu M**, et al. Spectroscopic intravascular photoacoustic imaging of lipids in atherosclerosis. Journal of biomedical optics, 2014, 19(2): 026006-026006.

PhD portfolio

Courses	Year	ECTS
vascular clinical epidemiology	2012	1.5
English biomedical writing and communication	2014	4
Pathophysiology of ischemic heart disease	2014	1.5

Workshops and seminars	Year	ECTS
Seminar: Biomarkers in Cardiovascular Disease	2012	0.4
Seminar: Coronary and Cranial Thrombosis	2013	0.4
Seminar: New imaging strategies for the detection of atherosclerosis.	2014	0.2
NUMVSeminar (spring)	2014	0.15
NUMVSeminar (autumn)	2014	0.15
NUMVSeminar (spring)	2015	0.15
NUMVSeminar (autumn)	2015	0.15
Workshop: Photoshop and illustrator CS5	2013	0.3
Workshop: Photo-acoustic Imaging and Sensing	2012	0.15
Workshop: medical ultrasound transducer	2012	0.15
Workshop: Tissue Optics	2014	0.15
Workshop: Optical Design for Biomedical Imaging	2014	0.15
Workshop: Photoacoustic	2015	0.15
Workshop: Introduction to Optical Alignment Techniques	2015	0.3

Presentations	Year	ECTS
Oral presentation - 2014 BIOS, SPIE Photonics West conference	2014	1.6
Oral presentation - 9th Ultrasonic Biomedical Microscanning conference(UBM 2014)	2014	1.2
Poster presentation - Design of Medical Devices Europe 2014	2014	1.0
Oral presentation - COEUR Research Seminar:New imaging strategies for the detection of atherosclerosis.	2014	1.3
Oral presentation - 2015 BIOS, SPIE Photonics West conference	2015	1.6
Poster presentation - The optics in cardiology Symposium	2015	1.0
Oral presentation – NUMV Seminar	2015	1.0
Oral presentation - 2015 IEEE International Ultrasonics Symposium,	2015	1.6
Oral presentation - 2016 BIOS, SPIE Photonics West conference	2016	1.6
Oral presentation - UBM 2016	2016	1.3

International conferences	Year	ECTS
2012 IEEE International Ultrasonics Symposium, Dresden, Germany	2012	1.2
The optics in cardiology Symposium, Rotterdam	2013	0.6
the 8th international symposium on Biomechanics in Vascular Biology and Cardiovascular Disease	2013	0.6
2014 BiOS, SPIE Photonics West, San Francisco, USA	2014	1.8

COEUR Symposium:Current Cardiac and Vascular Aging Research at EMC, (Rotterdam, the Netherlands)	2014	0.4
9th Ultrasonic Biomedical Microscanning conference(UBM 2014), Scotland	2014	1.2
Design of Medical Devices Europe 2014 (Delft, the Netherlands)	2014	0.9
2015 BIOS, SPIE Photonics West, (San Francisco, USA)	2015	1.8
21th ultrasound contrast Imaging symposium,rotterdam	2015	0.6
optics in cardiology, rotterdam	2015	0.9
2015 IEEE International Ultrasonics Symposium, Taipei, Taiwan	2015	1.2
2016 BiOS, SPIE Photonics West, San Francisco, USA	2016	1.8
UBM 2016, Bonaire	2016	0.9

Total: 37.05